National Library
of Canada

Canadian Theses Service

Ottawa, Canada
K1A 0N4

Bibliothèque nationale
du Canada

Services des thèses canadiennes

CANADIAN THESES

THÈSES CANADIENNES

NOTICE

The quality of this microfiche is heavily dependent upon the quality of the original thesis submitted for microfilming. Every effort has been made to ensure the highest quality of reproduction possible.

If pages are missing, contact the university which granted the degree.

Some pages may have indistinct print especially if the original pages were typed with a poor typewriter ribbon or if the university sent us an inferior photocopy.

Previously copyrighted materials (journal articles, published tests, etc.) are not filmed.

Reproduction in full or in part of this film is governed by the Canadian Copyright Act, R.S.C. 1970, c. C-30.

AVIS

La qualité de cette microfiche dépend grandement de la qualité de la thèse soumise au microfilmage. Nous avons tout fait pour assurer une qualité supérieure de reproduction.

S'il manque des pages, veuillez communiquer avec l'université qui a conféré le grade.

La qualité d'impression de certaines pages peut laisser à désirer, surtout si les pages originales ont été dactylographiées à l'aide d'un ruban usé ou si l'université nous a fait parvenir une photocopie de qualité inférieure.

Les documents qui font déjà l'objet d'un droit d'auteur (articles de revue, examens publiés, etc.) ne sont pas microfilmés.

La reproduction, même partielle, de ce microfilm est soumise à la Loi canadienne sur le droit d'auteur, SRC 1970, c. C-30.

THIS DISSERTATION
HAS BEEN MICROFILMED
EXACTLY AS RECEIVED

LA THÈSE A ÉTÉ
MICROFILMÉE TELLE QUE
NOUS L'AVONS REÇUE

NL-339 (r. 86/06)

Canada

THE UNIVERSITY OF ALBERTA

SPIN-LATTICE RELAXATION OF ^{23}Na IN $NaNO_2$

BY

SRIPEN TOWTA

©

A THESIS
SUBMITTED TO THE FACULTY OF GRADUATE STUDIES AND RESEARCH
IN PARTIAL FULFILMENT OF THE REQUIREMENTS FOR THE DEGREE
OF DOCTOR OF PHILOSOPHY
IN
SOLID STATE PHYSICS

DEPARTMENT OF PHYSICS

EDMONTON, ALBERTA
FALL 1986

Permission has been granted to the National Library of Canada to microfilm this thesis and to lend or sell copies of the film.

The author (copyright owner) has reserved other publication rights, and neither the thesis nor extensive extracts from it may be printed or otherwise reproduced without his/her written permission.

L'autorisation a été accordée à la Bibliothèque nationale du Canada de microfilmer cette thèse et de prêter ou de vendre des exemplaires du film.

L'auteur (titulaire du droit d'auteur) se réserve les autres droits de publication; ni la thèse ni de longs extraits de celle-ci ne doivent être imprimés ou autrement reproduits sans son autorisation écrite.

ISBN 0-315-32525-9

THE UNIVERSITY OF ALBERTA

RELEASE FORM

NAME OF AUTHOR: Sripen Towta

TITLE OF THESIS: Spin-Lattice Relaxation of ^{23}Na in $NaNO_2$.

DEGREE: Ph.D.

YEAR THIS DEGREE GRANTED: 1986

Permission is hereby granted to THE UNIVERSITY OF ALBERTA LIBRARY to reproduce single copies of this thesis and to lend or sell such copies for private, scholarly or scientific research purposes only.

The author reserves other publication rights, and neither the thesis nor extensive extracts from it may be printed or otherwise reproduced without the author's written permission.

Signature: S. Towta

Permanent Address:

Department of Physics
Chiang Mai University
Chiang Mai, Thailand.

Date: 12 August 1986

THE UNIVERSITY OF ALBERTA

FACULTY OF GRADUATE STUDIES AND RESEARCH

The undersigned certify that they have read, and recommend to the Faculty of Graduate Studies and Research for acceptance, a thesis entitled "Spin-Lattice of ^{23}Na in $NaNO_2$" submitted by Sripen Towta in partial fulfilment of the requirements for the degree of Doctor of Philosophy.

D.G. Hughes

Supervisor

Stanley Segel

J.S. Martin

R.F. Egerton

John Stephenson

DATE: 8 August 1986

TO MY MOTHER

ABSTRACT

This thesis describes an experimental pulsed double nuclear magnetic resonance study of the orientation and temperature dependence of the spin-lattice relaxation of ^{23}Na nuclei in a single crystal of the ferroelectric material $NaNO_2$. A preliminary study showed that the quadrupole transition probability W_1 could best be measured by exciting the centre line of the three-line spectrum and measuring the rate $2W_1$ of the subsequent exponential approach of the satellite resonances to equilibrium. The orientation dependence of W_1, measured at room temperature, was in very good agreement with theory, and the six independent M-tensor components were obtained from the data. Similar measurements were made at 235 K, 170 K and 145 K. By studying the recovery of the centre line in addition to the satellites, it was found that the relaxation was entirely magnetic at 145 K and largely so at 170 K. However, it was still possible to extract approximate values of W_1 at 170 K, from the recovery of the satellites. The orientation dependence was rather different from that at room temperature but was in good agreement with the theoretical form. At 235 K, the magnetic contribution to the spin-lattice relaxation was small, and the orientation dependence of W_1 was similar to that observed at room temperature. A second single crystal of $NaNO_2$, obtained from a different source,

showed identical magnetic relaxation, indicating that the magnetic relaxation may not be due to paramagnetic impurities but may be intrinsic and related to the unexplained T_1 minima of ^{14}N observed by Abe et al. in an NQR study. An ESR study failed to reveal a large enough concentration of paramagnetic centres to account for our data. Rapid diffusion of NO_2 ion or the frequent passage of domain walls could account for our data, but are unlikely to occur sufficiently rapidly at such low temperatures.

Measurements of the temperature dependence of W_1 showed that the quadrupole relaxation is not caused by phonons. Comparison of the ratios of M-tensor components with the results of point-charge calculations indicate that the quadrupole relaxation could be caused by an angular oscillation of the NO_2 groups about the $\underset{\sim}{c}$ axis of the crystal. However, an alternative possibility is that it is caused by the diffusion of a small concentration of lattice defects such as NO_2 vacancies.

The orientation dependence of W_1 was also measured at 432 K, near the critical temperature, 438 K, at which $NaNO_2$ undergoes a transition to a paraelectric phase. The noncritical or "background" contribution to the relaxation was removed by extrapolating data taken at lower temperatures.

The M-tensor component M_{1111}, associated with the critical contribution to the relaxation, was found to be negligible, in agreement with the results of a point-charge calculation, in which it is assumed that the relaxation is caused by reversal of the NO_2 groups. However, M_{1212} associated with the critical component was found to be much larger than theoretically predicted, indicating that perhaps the NO_2 groups are not all in the $\underset{\sim\sim}{bc}$ plane when they reverse their orientation.

ACKNOWLEDGEMENTS

I wish to express my sincere gratitude to Professor D.G. Hughes, my research supervisor, for his continual help, interest and encouragement throughout the work.

I am grateful to Mr. Willy Siewert, Mr. Dave Cramer and Mr. Len Wampler for the design, construction and repair of the electronic equipment, and to Mr. Ray Pegington, Mr. Gilbert Lachat and Mr. Alan Slater for the construction of NMR probes and sample holders. I also wish to thank Mr. Ken Marsh for technical assistance in the laboratory, and Mr. Bigam for running the ESR spectra.

It is a pleasure to acknowledge the University of Alberta for financial support in the form of Graduate Assistantships.

TABLE OF CONTENTS

Chapter Page

1 INTRODUCTION 1

2 THEORY 7

2.1 Elementary description of pulsed NMR 7

2.2 Nuclear electric quadrupole interaction 15

2.2.1 Nuclear electric quadrupole Hamiltonian 15

2.2.2 Quadrupole-split NMR spectrum of nuclei in single crystals 18

2.2.3 Orientation dependence of the nuclear quadrupole spin lattice relaxation in single crystals 20

2.2.4 Calculation of the ratios of the M-tensor component using a point-charge model 29

2.3 Time dependent behaviour of a system of $I=3/2$ nuclei experiencing first-order quadrupole splitting 30

2.3.1 Quadrupole relaxation 30

2.3.2 Magnetic relaxation 36

2.3.3 Quadrupole and magnetic relaxation 40

3 CRYSTAL STRUCTURE OF $NaNO_2$; QUADRUPOLE SPLITTING AND QUADRUPOLE RELAXATION OF ^{23}Na IN A $NaNO_2$ SINGLE CRYSTAL 43

3.1 Crystal structure of $NaNO_2$ 43

3.2 Orientation dependence of the ^{23}Na quadrupole splitting in $NaNO_2$ 46

3.3 Orientation dependence of the ^{23}Na quadrupole relaxation in $NaNO_2$ 47

Chapter Page

4 EXPERIMENTAL DETAILS 49

4.1 Equipment 49

4.1.1 Pulsed DNMR spectrometer 49

4.1.2 NMR probe 53

4.1.3 Faraday shield 58

4.1.4 Sample holders and variable temperature systems 64

4.1.5 Pulse generator 70

4.1.6 Magnet 71

4.2 Sodium nitrite 71

4.3 Installation of the $NaNO_2$ crystals in the sample holder 72

4.4 Experimental procedure 76

4.4.1 Measurement OF FID amplitudes 76

4.4.2 Choice of experimental method to study the orientation dependence of the quadrupole relaxation 80

4.4.3 Choice of experimental parameters to study the orientation dependence of the quadrupole relaxation 89

4.4.4 Setting-up procedure 91

5 RESULTS AND ANALYSIS 94

5.1 Temperature dependence of the spin-lattice relaxation of ^{23}Na in $NaNO_2$ 94

5.2 Orientation of dependence of the spin-lattice relaxation of ^{23}Na in $NaNO_2$ 103

5.2.1 Orientation dependence at room temperature 103

Chapter Page

5.2.2 Orientatin dependence at low temperatures (135 K, 145 K and 170 K) 111

5.2.3 Orientation dependence at 235 K 128

5.2.4 Orientation dependence at 432 K 132

5.3 Temperature dependence of the quadrupole coupling constant and asymmetry parameter of ^{23}Na in $NaNO_2$ 132

5.4 Electron spin resonance spectrum of a single crystal of $NaNO_2$ 143

6 DISCUSSION 150

6.1 Temperature dependence of the spin-lattice relaxation 150

6.2 Cause of the observed magnetic relaxation 153

6.3 Orientation dependence of the quadrupole relaxation at and below room temprature 162

6.4 Orientation dependence of the quadrupole relaxation at 432 K 170

6.5 Temperature dependence of the M-tensor components 176

BIBLIOGRAPHY 179

LIST OF TABLES

Table		Page
1	W_1 of ^{23}Na in $NaNO_2$ at various crystal orientations, obtained from experiments (ii) and (iii)	85
2	W_{hfs} measured at different temperatures at $\theta=4°$, $\phi=0°$.	95
3	W_{hfs} measured at different temperatures at $\theta=0°$.	98
4	Orientation dependence of W_1 at 298 K.	106
5	M-tensor components multiplied by $e^2Q^2/96$ at various temperatures.	109
6	W_1 and W_2 at various temperatures and orientations.	110
7	Orientation dependence of W_{hfs} at 170 K.	112
8	Orientation dependence of W_{hfs} at 145 K.	116
9	W_{cl} and W_{hfs} at different orientations and temperatures.	121
10	Orientation dependence of $4W_3$ and W_1 at 170 K.	127
11	Orientation dependence of W_{hfs} and W_1 at 235 K.	131
12	Orientation dependence of W_1 at 432 K.	135
13	Quadrupole coupling constant e^2qQ/h at various temperatures.	139
14	Asymmetry parameter η at various temperatures.	140
15	Values of the activation energy derived from the asymptotic values of the slope of the graph of T_1 versus T by Abe et al. (1972).	163
16	Experimental values of the ratios of the M-tensor components.	165
17	Theoretical values of the ratios of the M-tensor components.	167

Table Page

18 M-tensor components associated with the critical contribution to the relaxation at 432 K. 174

19 The ratios of the M-tensor components associated with the critical contribution to the relaxation at 432 K. 175

LIST OF FIGURES

Figure — Page

2.1 Precession of the nuclear magnetization in the rotating coordinate system. 11

2.2 Schematic representation of (a) the FID following a 90° pulse, (b) the FID following a 180°-τ-90° pulse sequence. 14

2.3 Orientation of the external magnetic field relative to the principal axes of the crystal. 22

2.4 Energy level diagrams for a system of nuclei with $I=3/2$ showing (a) quadrupole transitions (b) magnetic transitions. 33

3.1 Unit cell of sodium nitrite and the crystal coordinate system used to denote the orientation of the magnetic field $\vec{H}_o$. 45

4.1 Block diagram of the pulsed DNMR spectrometer. 51

4.2 Circuit diagram of the NMR probe. 55

4.3 Profile of(a) an earlier version (b) a later version, of the Faraday shield. 62

4.4 Low temperature sample holder and variable temperature system. 66

4.5 Schematic diagrams of sample holder showing (a) a horizontal section through Axis 2 (b) a front view of Angular Scale 2. 74

4.6 Schematic diagram of an FID. 79

5.1 Half the relaxation rate of the high frequency satellite, W_{hfs}, of ^{23}Na in a single crystal of $NaNO_2$ at $\theta=4°$, $\phi=0°$ plotted as a function of temperature. 97

5.2 Half the relaxation rate of the high frequency satellite, $W_{hfs}(\approx W_1)$, of ^{23}Na in a single crystal of $NaNO_2$ at $\theta=0°$ plotted as a function of temperature. 100

5.3 Variation of W_1 with θ at $\phi=0°$, 45° and 90° for ^{23}Na in $NaNO_2$ at 298 K. 108

Figure		Page
5.4	Variation of W_{hfs} with θ at $\phi=0°$, 45° and 90° for ^{23}Na in $NaNO_2$ at 170 K.	114
5.5	Variation of W_{hfs} with θ at $\phi=0°$. 45° and 90° for ^{23}Na in $NaNO_2$ at 145 K.	118
5.6	Logarithm of W_{hfs} plotted versus 1/T at low temperatures.	124
5.7	Variation of W_1 with θ at $\phi=0°$, 45° and 90° for ^{23}Na in $NaNO_2$ at 170 K.	130
5.8	Variation of W_1 with θ at $\phi=0°$. 45° and 90° for ^{23}Na in $NaNO_2$ at 235 K.	134
5.9	Variation of W_1 with θ at $\phi=0°$, 45° and 90° for ^{23}Na in $NaNO_2$ at 432 K.	137
5.10	The quadrupole coupling constant e^2qQ/h plotted as a function of temperature.	142
5.11	ESR spectrum of Crystal B with the magnetic field perpendicular to the **b** axis and making an angle of about 25° with the **c** axis.	145
5.12	ESR spectrum of Crystal B with the magnetic field parallel to the **a** axis.	147
6.1	The spin-lattice relaxation rate $T_1^{-1}= (2/5)(W_1+4W_2)$ of ^{23}Na in a single crystal of $NaNO_2$ measured as a function of temperature by Bonera et al. (1970).	152
6.2	The spin-lattice relaxation time T_1 of ^{14}N in $NaNO_2$ powder measured as a function of temperature in a NQR study by Abe et al. (1972).	158
6.3	Logarithm of f_{min} plotted against the reciprocal of the temperature at which the relaxation time is a minimum.	161
6.4	Values of $W_{hfs}(=W_1)$ plotted against temperature between 200 K and 410 K.	172
6.5	Values of the M-tensor components plotted as a function of temperature.	178

CHAPTER 1

INTRODUCTION

A nucleus possessing a magnetic moment $\vec{\mu}$ and a collinear angular momentum $\vec{J}$, situated in a magnetic field $\vec{H}_o$, has 2I+1 energy levels given by $-\gamma\hbar H_o m$ where $\gamma=\vec{\mu}/\vec{J}$ is the gyromagnetic ratio. Also, m is the magnetic quantum number which can take one of (2I+1) values I, I-1,...,-I and I is the nuclear spin quantum number which is either an integer or a half integer depending on the nucleus involved. A radiofrequency (rf) magnetic field polarized at right angles to $\vec{H}_o$ will induce transitions corresponding to $\Delta m = \pm 1$ between adjacent energy levels, provided its angular frequency ω is such that $\hbar\omega = \hbar\gamma H_o$ or $\omega = \gamma H_o$. This is the well known NMR phenomenon.

In practice, nuclei experience time-dependent magnetic fields produced by their surroundings. These cause $\Delta m = \pm 1$ transitions between adjacent energy levels, and they enable the spin system to come into thermal equilibrium with the surroundings. This phenomenon is called spin-lattice relaxation, the mechanism is called magnetic relaxation, and the approach to equilibrium is often exponential, the characteristic time being called the spin-lattice relaxation time T_1.

In solids, the magnetic relaxation caused by lattice vibrations is usually very weak, because their characteristic frequencies are much higher than typical NMR frequencies. In such cases, the dominant magnetic relaxation is often caused by the fluctuating magnetic fields associated with paramagnetic impurities.

Nuclei with I > 1 possess an electric quadrupole moment in addition to a magnetic dipole moment. This nuclear electric quadrupole moment will interact with the electric field gradient at the nuclear site. In particular, the interaction with the time-averaged electric field gradient modifies the Zeeman energy levels. For ^{23}Na nuclei (I = 3/2) situated at identical sites in a single crystal, the case with which we shall be mainly concerned, the quadrupole interaction is much smaller than the Zeeman interaction in a magnetic field ~1 T, and the effect is to split the NMR line into three components, the so-called centre line associated with the transition $m = \frac{1}{2} \leftrightarrow -\frac{1}{2}$, flanked on either side by a pair of so-called satellites associated with the transitions $m = \pm\frac{3}{2} \leftrightarrow \pm\frac{1}{2}$.

The interaction of the nuclear electric quadrupole moment with the time-dependent part of the electric field gradient gives rise to transitions between the nuclear magnetic energy levels, a phenomenon called quadrupole relaxation. The magnitudes of quadrupole moments are such that, in most cases, the quadrupole relaxation caused by a particular lattice motion is much more effective than the magnetic relaxation. In contrast to the magnetic case, the transition $m = +1/2 \leftrightarrow -1/2$ is not allowed but transitions corresponding to $\Delta m = \pm 2$ are allowed. For I=3/2, the probabilities of the allowed $\Delta m = \pm 1$ and ± 2 transitions are denoted by W_1 and W_2 respectively.

For a system of nuclei situated at identical sites in a single crystal, the dependence of W_1 and W_2 on the orientation of the crystal relative to the external magnetic field $\vec{H}_0$ has been calculated by Pietilä (1968), Snyder and Hughes (1971) and Hughes (1973). In general, the form of the orientation dependence varies with the point group symmetry of the nuclear sites, and W_1 and W_2 can each be expressed as a linear combination of the components of a real fourth-rank tensor. The components of this so-called M-tensor contain information about the dynamical environment of the spin system.

The orientation dependence of W_1 and W_2 has been measured for the ^{23}Na spin system in a single crystal of $NaNO_3$ ($\bar{3}$ symmetry) where the quadrupole relaxation is primarily caused by phonons. The observed orientation dependence was found to be good agreement with theory at 77 K (Niemelä, 1967; Hughes, Reed and Snyder, 1970), and at room temperature (Spencer and Hughes, 1978). Moreover, the ratios of the M-tensor components were in surprisingly good agreement with the results of a point charge calculation which assumes isotropic motion of the sodium ion.

Sodium nitrite is a crystal which is ferroelectric at room temperature (Sawada et al, 1958) but undergoes an order-disorder transition to an antiferroelectric phase at 437 K and to a paraelectric phase at 438 K. Since Sawada's discovery, a large number of ^{23}Na NMR and ^{14}N NQR investigations have been performed on this material. The first detailed study of the temperature dependence of the spin-lattice relaxation of ^{23}Na in $NaNO_2$ was carried out by Bonera, Borsa and Rigamonti (1970), henceforth referred to as BBR. They oriented a single crystal relative to the external magnetic field so that the centre line and satellites approximately overlapped. In that case, the approach of the spin system to equilibrium is exponential and the spin-lattice relaxation time is given by $T_1^{-1} = (2/5)(W_1 + 4W_2)$ where W_1 and W_2 refer, of course, to the particular crystal orientation used. They observed an unexpected rapid increase of T_1^{-1} between 170 K and 220 K and this is still not properly understood. They also observed a critical point anomaly near the transition to the paraelectric phase. In BBR's work and in subsequent investigations of the critical point anomaly by Avogadro et al (1971, 1975), the orientation dependence of W_1 and W_2 was largely ignored. To extract maximum information from measured quadrupole relaxation rates requires the determination of all the independent components of the M-tensor. There is no a priori reason why they should scale identically with temperature. Indeed, Hughes and Spencer (1982) have shown that BBR's data imply that the ratios of the M-tensor components of ^{23}Na in $NaNO_2$ change significantly near the ferroelectric transitions, though it was not possible to detetmine these values. It is therefore not known which

M-tensor component or components do display a critical point anomaly at the transition. The only systematic study of the orientation dependence of the quadrupole relaxation of ^{23}Na in $NaNO_2$ has been carried out by Hughes and Spencer (1982). By measuring the orientation dependence of W_1/W_2, they were able to determine the ratios of the M-tensor components. However, their study was only carried out at room temperature.

The initial purpose of the work described in this thesis was to measure the orientation dependence of the quadrupole relaxation of ^{23}Na in $NaNO_2$ at various temperatures in order to determine the temperature dependence of each of the M-tensor components. It was hoped thereby to obtain an improved understanding of the factors determining the magnitude of the M-tensor components and to obtain useful information about the lattice dynamical details of the crystal. However, during the work, it became apparent that the spin-lattice relaxation at low temperature was magnetic rather than quadrupolar. Some time was therefore spent trying to understand the ^{23}Na spin-lattice relaxation observed at low temperature and trying to interpret published ^{14}N relaxation data in $NaNO_2$ obtained at low temperature by NQR.

In our work the relaxation behaviour of ^{23}Na in $NaNO_2$ was mainly studied by a pulsed double NMR (DNMR) method. In this technique a selective 90° or 180° pulse is applied to the centre line of the quadrupole-split spectrum, and the recovery of one of the satellites towards equilibrium is observed by applying a selective 90° pulse at the frequency of the satellite. For quadrupole relaxation, the recovery of the satellite should be exponential with a rate of $2W_1$. Measurements were made as a function of crystal orientation at various temperatures ranging from 130 K to 462 K. The only inaccessible orientations were those where the satellites and centre line were too closely spaced for them to be individually or selectively excited by rf pulses. However, measurements could be made at enough crystal orientations so that the various M-tensor components could be determined.

In order to obtain meaningful values of the M-tensor components, it was necessary to make precise measurements of relaxation rates. We aimed for, and achieved, a precision of about 1% in our work. This required good instrumentation and lengthy measurement times to perform the required signal averaging. Also necessary was a stable and uniform sample temperature and a method for accurately setting the crystal orientation.

The general theory is developed in section 2, and applied specifically to ^{23}Na and $NaNO_2$ in section 3. Experimental details are described in section 4. The results are given and analyzed in section 5 and discussed in section 6.

CHAPTER 2

THEORY

2.1 Elementary description of pulsed NMR

The classical equation of motion for a spin of magnetic moment $\vec{\mu}$ and collinear angular momentum $\vec{J}$, situated in a steady magnetic field $\vec{H}_o$, is

$$d\vec{J}/dt = \vec{\mu} \times \vec{H}_o \ . \tag{2.1}$$

It follows that

$$d\vec{\mu}/dt = \gamma\vec{\mu} \times \vec{H}_o \tag{2.2}$$

where $\gamma = \vec{\mu}/\vec{J}$, the gyromagnetic ratio of the spin. It can be shown quantum mechanically (Slichter, 1980) that the expectation value of the magnetic moment $\langle\vec{\mu}\rangle$ of a nuclear spin situated in a steady magnetic field $\vec{H}_o$ is given by a similar equation, namely

$$d\langle\vec{\mu}\rangle/dt = \gamma\langle\vec{\mu}\rangle \times \vec{H}_o \quad . \tag{2.3}$$

For a group of nuclei, the total magnetic moment or macroscopic magnetization is given by

$$\vec{M} = \sum\vec{\mu}_k \tag{2.4}$$

where $\vec{\mu}_k$ is the magnetic moment of the kth nucleus. If the nuclei are identical, the equation of motion for the macroscopic magnetization $\vec{\mu}$ is therefore

$$d\vec{M}/dt = \gamma\vec{M} \times \vec{H}_o \quad . \tag{2.5}$$

If the motion of the magnetization is viewed from a frame of reference rotating about $\vec{H}_o$ with an angular velocity Ω, the equation of motion is (Slichter, 1980)

$$d\vec{M}_{rot}/dt = \vec{M}_{rot} \times (\gamma\vec{H}_o + \vec{\Omega}) \ . \tag{2.6}$$

If $\vec{\Omega} = -\gamma\vec{H}$, then $d\vec{M}_{rot}/dt$ is obviously zero and $\vec{M}_{rot}$ is time independent. This shows that the nuclear magnetization, when viewed from the laboratory frame, precesses indefinitely around $\vec{H}_o$ at a frequency Ω which is numerically equal to γH_o. The precession frequency $\Omega = \gamma H_o$ is called the Larmor frequency, and is equal in magnitude to the angular frequency needed to produce magnetic resonance absorption. The sense of the precession is governed by the sign of γ.

Suppose that, in addition to a steady magnetic field $\vec{H}_o$ applied along the z axis say, we apply to the spin system a rotating magnetic field

$$\vec{H}_1 = H_1(\hat{i}\cos\omega t + \hat{j}\sin\omega t) \tag{2.7}$$

directed at right angles to $\vec{H}_o$. Viewed from a coordinate system that rotates about the z axis at the same frequency ω and in the same sense as $\vec{H}_1$, and with $\vec{H}_1$ directed along the x axis, the equation of motion of the magnetization becomes

$$\frac{d\vec{M}_{rot}}{dt} = \vec{M}_{rot} \times [\hat{i}\gamma H_1 + \hat{k}(\omega + \gamma H_o)] \ . \tag{2.8}$$

In this rotating frame, the magnetization precesses about a static effective magnetic field

$$\vec{H}_{eff} = \hat{i}H_1 + \hat{k}(H_o + \frac{\omega}{\gamma}) \ . \tag{2.9}$$

At resonance, when $\omega = -\gamma H_o$, i.e. when ω is numerically equal to the Larmor frequency,

$$\vec{H}_{eff} = \hat{i}H_1 \tag{2.10}$$

and the effective field is directed along the x axis of the rotating coordinate system. If the nuclear magnetization is initially parallel to $\vec{H}_o$, as it would be in thermal equilibrium for example, then the magnetization will precess in the yz plane about the x axis of the rotating frame with a frequency γH_1. If the rotating magnetic field $\vec{H}_1$ is applied for a short time τ_p say, the angle through which $\vec{M}$ precesses in the rotating frame is given in radians by

$$\theta = \gamma H_1 \tau_p \quad . \tag{2.11}$$

The situation is shown in Fig. 2.1(a). Of particular importance are so-called 90° and 180° pulses whose lengths (or amplitudes) are chosen so as to turn the nuclear magnetization through 90° and 180° respectively in the rotating coordinate system. This is shown in Fig. 2.1(b) and (c).

When viewed from the laboratory reference frame, the transverse component of the magnetization caused by the rf pulse rotates at the Larmor frequency around $\vec{H}_o$. The motion of this rotating component can be followed by monitoring the EMF induced in a coil wound around the sample with its axis orthogonal to $\vec{H}_o$. In practice, interactions among the nuclear spins, in particular magnetic dipole interactions, cause a dephasing of the precession of the individual spins and so the transverse magnetization decays away to zero. The rf signal across the coil similarly decays to zero, and the envelope of the decaying rf signal is called the free induction decay or FID. The situation

Figure 2.1

Precession of the nuclear magnetization (for $\gamma>0$) about the axis of the rotating coordinate system when a rf magnetic field $\vec{H}_1$ is applied along the x axis for a time τ_p. In case (a), $\gamma H_1 \tau_p$ is equal to θ. Cases (b) and (c) show 90° and 180° pulses where $\gamma H_1 \tau_p = \pi/2$ and π respectively.

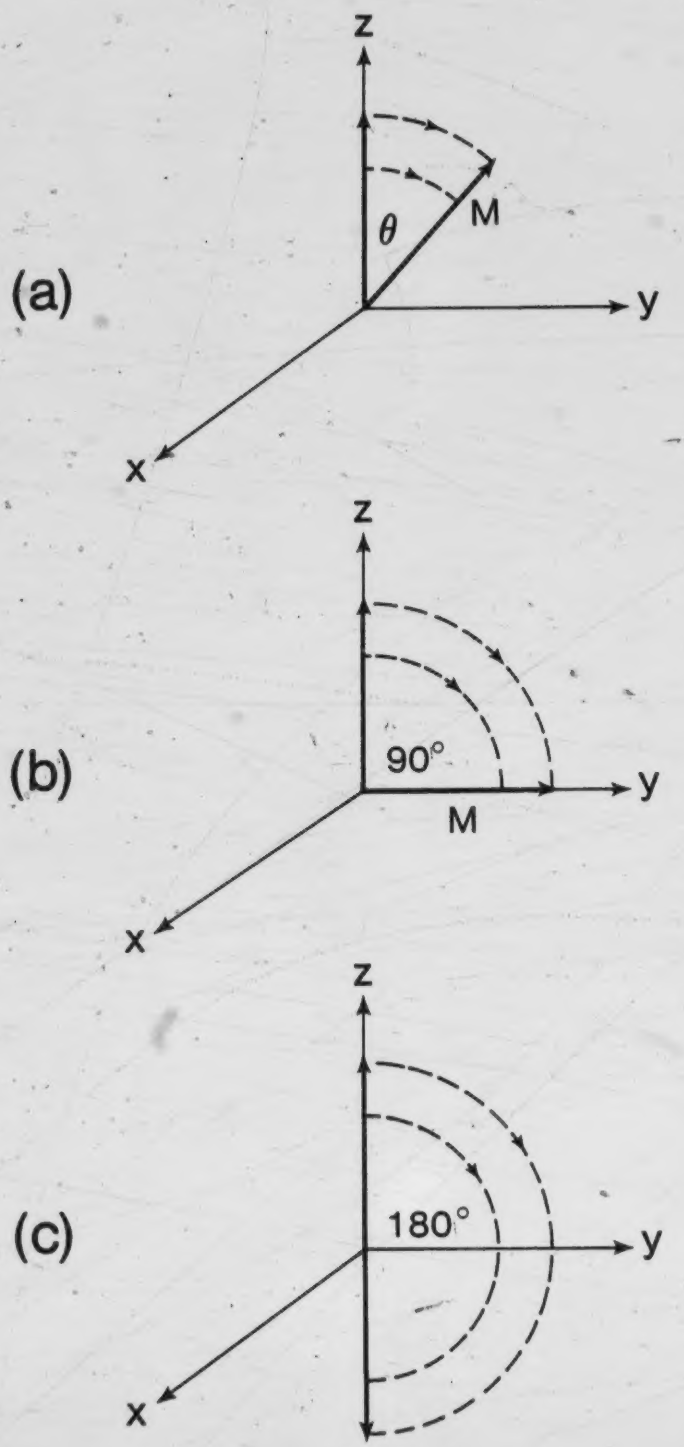
z
M
θ
(a)
y
x
z
90°
(b)
y
M
x
z
180°
(c)
y
x

is shown schematically for a 90° pulse in Fig. 2.2(a). It can be shown (cf. Slichter, 1980) that the FID, following a rf pulse whose duration is much shorter than the decay time, is the Fourier transform of the NMR absorption lineshape in the frequency domain. In solids, the nuclear magnetic dipole interactions cause the signal to decay rapidly in a time of order 10^{-4} s. The shape of the FID varies from one spin system to another but is, in many cases, roughly Gaussian in shape. In liquids, the magnetic dipole interactions are largely averaged out, and the decay time is much longer, often of the order of seconds. In such cases, the decay is exponential and the characteristic decay time is called the transverse or spin-spin relaxation time T_2.

Following a 180° pulse, there is no transverse magnetization and hence no FID. However, the magnetization has been completely reversed by the pulse. Because of interactions between the spin system and its surroundings, the magnetization gradually returns to its thermal equilibrium value. During that process, the magnetization remains parallel to the magnetic field and the process is called longitudinal or spin-lattice relaxation. The approach of the longitudinal magnetization toward equilibrium is exponential for spin systems with $I = 1/2$ and is often exponential for those with $I > 1/2$. In such cases, the characteristic recovery time is called the longitudinal

Figure 2.2

Schematic representation of (a) the FID following a 90° pulse, (b) the FID following a 180°-τ-90° pulse sequence.

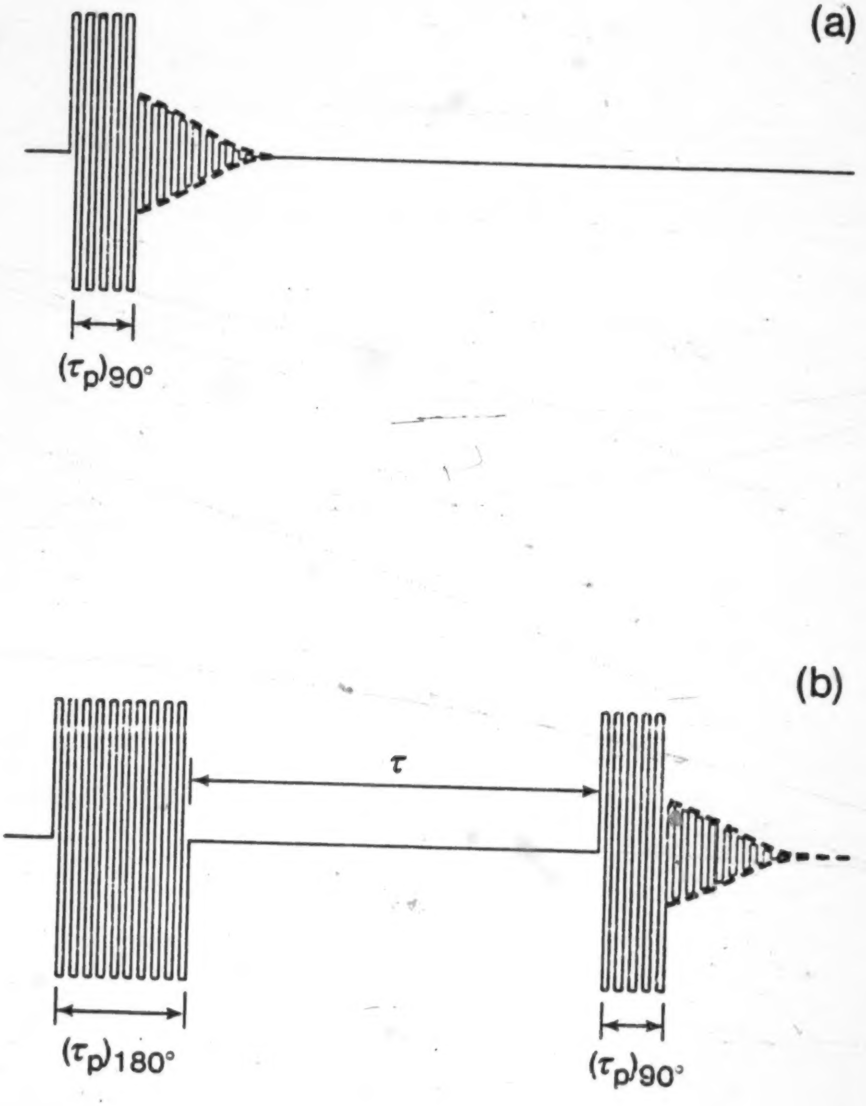
(a)
$(\tau_p)_{90°}$
(b)
τ
$(\tau_p)_{180°}$
$(\tau_p)_{90°}$

or spin-lattice relaxation time T_1 and the recovery of the longitudinal magnetization following a 180° pulse is given by

$$M_z(t) = M_o[1 - 2\exp(-t/T_1)] \ . \tag{2.12}$$

In non-metallic solids, T_1 is typically in the range 10^{-2} to 10^4 s.

2.2 Nuclear electric quadrupole interactions

2.2.1 Nuclear electric quadrupole Hamiltonian

For a nucleus which has a spin number $I > 1$, it is necessary to take into account the electrostatic interaction of the nucleus with its surroundings. The electrostatic Hamiltonian is

$$\mathcal{H} = \int\rho(\vec{r})V(\vec{r})dV \tag{2.13}$$

where $\rho(\vec{r})$ is the nuclear charge density, $V(\vec{r})$ is the electrostatic potential caused by the charges external to the nucleus and the integral is over the nuclear volume. By expressing the potential $V(\vec{r})$ as a Taylor expansion in a Cartesian coordinate system of arbitrary orientation but whose origin is at the nuclear center of mass, the Hamiltonian becomes

$$\begin{aligned}\mathcal{H} &= \int\rho(\vec{r})\left[V_o + \sum_j \left(\frac{\partial V}{\partial x_j}\right)_o x_j + \frac{1}{2}\sum_{jk}\left(\frac{\partial^2 V}{\partial x_j \partial x_k}\right)_o x_j x_k + \ldots\right]dV \\ &= ZeV_o + \sum_j P_j\left(\frac{\partial V}{\partial x_j}\right)_o + \frac{1}{2}\sum_{jk} Q'_{jk}\left(\frac{\partial^2 V}{\partial x_j \partial x_k}\right)_o + \ldots \end{aligned} \tag{2.14}$$

where $\int\rho(\vec{r})dV$ is Ze, the nuclear charge,

$\int\rho(\vec{r})x_j dV$ is P_j, the jth component of the nuclear electric dipole moment,

$\int\rho(\vec{r})x_j x_k dV$ is Q'_{jk}, the jkth component of the nuclear electric quadrupole moment tensor.

Since the first term in the Hamiltonian is orientation independent, it is of no interest here. Furthermore, because of parity considerations, the electric dipole moment (and the electric octupole moment etc.) measured relative to the nuclear center of mass vanishes. Thus, the expression for the Hamiltonian can be written as

$$\mathcal{H} = \frac{1}{2}\sum_{jk} Q'_{jk}V_{jk} + \text{hexadecapole term} + \ldots \qquad (2.15)$$

where $V_{jk} = \partial^2 V/\partial x_j \partial x_k$ is the jk component of the electric field gradient tensor. The hexadecapole interaction is negligible in all practical cases in NMR (Abragam, 1961). Therefore we need only consider the quadrupole Hamiltonian

$$Q = \frac{1}{2}\sum_{jk} Q'_{jk}V_{jk} . \qquad (2.16)$$

The quadrupole moment tensor Q'_{jk} is obviously symmetric and thus has at most six independent components. It is convenient to define a tensor Q_{jk} which is both symmetric and traceless. This is done by writing

$$Q_{jk} = 3Q'_{jk} - \delta_{jk}\sum_{\ell} Q'_{\ell\ell} \qquad (2.17)$$

where δ_{jk} is the Kronecker delta function. By substituting Q'_{jk} from Eq. (2.17) in Eq. (2.16) and ignoring the term involving traces since it is independent of the nuclear orientation, it is found that

$$\mathcal{H}_Q = \frac{1}{6} \sum_{jk} Q_{jk} V_{jk} \, . \tag{2.18}$$

By using the theorem that the corresponding matrix elements of all traceless second-rank symmetric tensors are proportional (Ramsey, 1953), it can be shown (Cohen and Reif, 1957) that the matrix elements of the quadrupole Hamiltonian are given by

$$\langle m' | \mathcal{H} | m \rangle = [eQ/6I(2I-1)] \sum_{jk} \langle m' | \tfrac{3}{2}(I_j I_k + I_k I_j) - \delta_{jk} I^2 | m \rangle V_{jk} , \tag{2.19}$$

where Q is a scalar quantity called the nuclear quadrupole moment and is defined by

$$eQ = \int \rho(\vec{r})(3z^2 - r^2) dV$$

where $\rho(\vec{r})$ is the nuclear charge density, the z axis is parallel to the external magnetic field, and the nucleus is in a state where the z component of the angular momentum is a maximum. By introducing the raising and lowering spin operators,

$$I_{\pm} = I_x \pm iI_y \quad , \tag{2.20}$$

the Hamiltonian becomes

$$\langle m' | \mathcal{H} | m \rangle = [eQ|eI(2I-1)] \langle m' | (3I_z^2 - I^2)V_o + (I_+ I_z + I_z I_+)V_{-1} + (I_- I_z + I_z I_-)V_{+1} + I_+^2 V_{-2} + I_-^2 V_{+2} | m \rangle \, , \tag{2.21}$$

where

$$\begin{aligned} V_o &= V_{zz} \\ V_{\pm 1} &= V_{xz} \pm iV_{yz} \\ V_{\pm 2} &= \tfrac{1}{2}(V_{xx} - V_{yy}) \pm iV_{xy} \, . \end{aligned} \tag{2.22}$$

In a representation that diagonalizes the Zeeman energy, the matrix elements of $\mathcal{H}_Q$ are

$$\langle m|\mathcal{H}_Q|m\rangle = A[3m^2 - I(I+1)]V_o \qquad (2.23)$$

$$\langle m\pm 1|\mathcal{H}_Q|m\rangle = A(2m\pm 1)[(I\mp m)(I\pm m+1)]^{1/2}V_{\mp 1} \qquad (2.24)$$

$$\langle m\pm 2|\mathcal{H}_Q|m\rangle = A[I\mp m)(I\mp m-1)(I\pm m+1)(I\pm M+2)]^{1/2}V_{\mp 2} \qquad (2.25)$$

$$\langle m'|\mathcal{H}_Q|m\rangle = 0 \quad \text{for} \quad |m'-m| > 2 \qquad (2.26)$$

where $A = eQ/4I(2I-1)$.

2.2.2 Quadrupole-split NMR spectrum of nuclei in single crystals

Consider a system of quadrupolar nuclei situated at identical sites in a single crystal. In the so-called high field case, the quadrupole interaction is much smaller than the Zeeman interaction and is therefore treated as a perturbation. The Hamiltonian of the spin system is then given by

$$\mathcal{H} = -\gamma\hbar m H_o + \mathcal{H}_Q \qquad (2.27)$$

where the matrix elements of $\mathcal{H}_Q$ are given in Eqs. (2.23), (2.24), (2.25), (2.26) and the z axis of the coordinate system coincides with the magnetic field direction. To second order in the quadrupole interaction, the energy levels are given by (Bersohn, 1952)

$$E_m = -\gamma\hbar m H_o + A[3m^2 - I(I+1)]V_o + 2A^2\,\frac{({}^{V}{+1})({}^{V}{-1})}{\gamma\hbar H_o}\,m \times$$

$$[4I(I+1)-1-8m^2] - 2A^2\,\frac{({}^{V}{+2})({}^{V}{-2})}{\gamma\hbar H_o}\,m\,[2I(I+1)-1-2m^2]. \qquad (2.28)$$

The NMR frequencies are governed by the time-averaged values of E_m and these values are in turn governed by the time-averaged values of the components of the electric field gradient tensor.

To take advantage of crystal symmetry, we choose a different coordinate system from that used previously. Let xyz be a principal coordinate system fixed with respect to the crystal so that $\bar{V}_{xy} = \bar{V}_{yz} = \bar{V}_{xz} = 0$. The x,y and z axes are traditionally chosen so that

$$|\bar{V}_{zz}| > |\bar{V}_{yy}| > |\bar{V}_{xx}| \quad . \tag{2.29}$$

It is also convenient to define two parameters q and η by

$$eq = \bar{V}_{zz} \tag{2.30}$$

and

$$\eta = (\bar{V}_{xx} - \bar{V}_{yy})/\bar{V}_{zz} \quad . \tag{2.31}$$

η is a measure of the departure from axial symmetry and is called the asymmetry parameter of the electric field gradient. Since the electric field gradient tensor components obey Laplace's equation, $\nabla^2 V = 0$, then η satisfies the condition

$$0 < \eta < 1 \quad . \tag{2.32}$$

If the nuclei are situated on 3-fold, 4-fold or 6-fold axes of symmetry, $\bar{V}_{xx}$ and $\bar{V}_{yy}$ are equal and η is zero.

We denote the polar and azimuthal angles of the external magnetic field $\vec{H}_0$ with respect to the crystal coordinate system (xyz) by θ and ϕ respectively, as shown in Fig. 2.3. By transforming Eq. (2.28) from the laboratory coordinate system to the crystal coordinate system, it can be shown that

$$\begin{aligned} E_m = & -\gamma\hbar m H_o + \frac{3Aeq}{2}(3\cos^2\theta-1+\eta\sin^2\theta\cos2\phi)\{m^2-\frac{1}{3}I(I+1)\} \\ & + \frac{A^2e^2q^2}{4h\nu_o}[2m\{4I(I+1)-1-8m^2\}\{\frac{9}{4}\sin^2 2\theta-\frac{3}{2}\eta\sin^2 2\theta\cos2\phi \\ & + \eta^2(\sin^2\theta-\sin^4\theta\cos2\phi)\} - \frac{m}{2}\{2I(I+1)-1-2m^2\}\{9\sin^4\theta \\ & + 6\eta\sin^2\theta\cos2\phi(2-\sin^2\theta)+\eta^2(\cos^2 2\phi\sin^4\theta+4(1-\sin^2\theta))\}] \end{aligned} \tag{2.33}$$

The frequencies of the quadrupole-split NMR lines, $|E_{m-1}-E_m|/h$, are therefore given, in second order by

$$\begin{aligned} \nu_{m\to m-1} = & \nu_o + \frac{3Aeq}{2h}(1-2m)(3\cos^2\theta-1+\eta\sin^2\theta\cos2\phi) \\ & + \frac{A^2e^2q^2}{4h^2\nu_o}[(-8I(I+1)+18+48m(m-1)\{\frac{9}{4}\sin 2\theta-\frac{3}{2}\eta\sin^2 2\theta\cos2\phi \\ & + \eta^2(\sin^2\theta-\sin^4\theta\cos2\phi)\} + (I(I+1)-\frac{3}{2}-2m(m-1))\{9\sin^4\theta \\ & + 6\eta\sin^2\theta\cos2\phi(2-\sin^2\theta)+\eta^2(\cos^2 2\phi\sin^4\theta+4(1-\sin^2\theta))\}] \end{aligned} \tag{2.34}$$

where ν_o is the unperturbed resonance frequency.

2.2.3 Orientation dependence of the nuclear quadrupole spin lattice relaxation in single crystals

Consider again a system of quadrupolar nuclei situated at identical sites in a single crystal. Thermal fluctuations in the electric field gradient induce transitions between energy levels of the nuclear spin system via the coupling between the nuclear electric quadrupole moment and

Figure 2.3

Orientation of the external magnetic field relative to the principal axes of the crystal

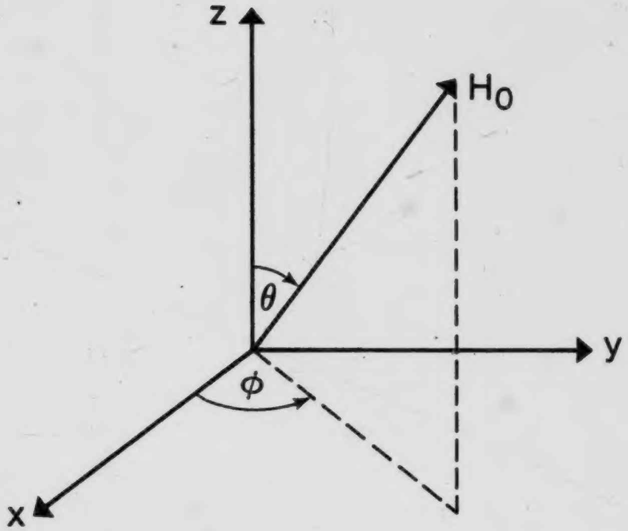
z
H_0
θ
y
ϕ
x

the time dependent electric field gradient at the nuclear sites. The transition probability per unit time for this case is given by

$$W_{mn\to m'n'} = 2\pi\hbar^{-1}\left|\langle m'n'|\mathcal{H}_Q|mn\rangle\right|^2\delta(E_{m'}+E_{n'}-E_m-E_n) \qquad (2.35)$$

where m and m' are the initial and final spin states, n and n' are the initial and final lattice states. If the lattice is in equilibrium at a temperature T, the average transition probability per unit time of the spin transition m→m' is

$$W_{m\to m'} = \frac{\sum_{nn'} e^{-\beta E_n} W_{mn\to m'n'}}{\sum_n e^{-\beta E_n}} \qquad (2.36)$$

where $\beta = 1/kT$. For transitions where m changes by ±1 and ±2, the transition probabilities per unit time can be written as

$$W_{m\to m+1} = \frac{2\pi\lambda_1^2}{\hbar}\,\frac{\sum_{nn'}\exp(-\beta E_n)\left|\langle n'|V_{x'z'}-iV_{y'z'}|n\rangle\right|^2\delta(E_{n'}-E_n+E_{m+1}-E_m)}{\sum_n \exp(-\beta E_n)} \qquad (2.37)$$

and

$$W_{m\to m+2} = \frac{2\pi\lambda_2^2}{\hbar}\times \frac{\sum_{nn'}\exp(-\beta E_n)\left|\langle n'|\tfrac{1}{2}(V_{x'x'}-V_{y'y'})-iV_{x'y'}|n\rangle\right|^2\delta(E_{n'}-E_n+E_{m+2}-E_m)}{\sum_n \exp(-\beta E_n)}. \qquad (2.38)$$

Here, x'y'z' form a coordinate system whose z' axis coincides with the direction of the external magnetic field, and

$$\lambda_1 = A(2m+1)[(I-m)(I+m+1)]^{1/2}$$
$$\lambda_2 = A[(I-m)(I-m-1)(I+m+1)(I+m+2)]^{1/2}.$$

It is convenient to define (cf. Yosida and Moriya, 1956) two quantities W_1 and W_2, which characterize the nuclear quadrupole spin-lattice relaxation. They are defined by the expressions

$$W_{m\to m+1} = \frac{W_1(2m+1)^2(I+m+1)(I-m)}{2I(2I-1)^2} \tag{2.39}$$

and

$$W_{m\to m+2} = \frac{W_2(I-m)(I-m-1)(I+m+1)(I+m+2)}{2I(2I-1)^2} \tag{2.40}$$

It follows from Eqs. (2.37), (2.38), (2.39) and (2.40) that, for I = 3/2, W_1 and W_2 are

$$W_1 = \frac{\pi e^2 Q^2}{4I\hbar} \frac{\sum_{nn'} \exp(-\beta E_n)\langle n'|V_{x'z'}-iV_{y'z'}|n\rangle|^2 \delta(E_{n'}-E_n+E_{m+1}-E_m)}{\sum_n \exp(-\beta E_n)} \tag{2.41}$$

and

$$W_2 = \frac{\pi e^2 Q^2}{4I\hbar} \times$$
$$\frac{\sum_{nn'} \exp(-\beta E_n)|\langle n'|\frac{1}{2}(V_{x'x'}-V_{y'y'})-iV_{x'y'}|n\rangle|^2 \delta(E_{n'}-E_n+E_{m+2}-E_m)}{\sum_n \exp(-\beta E_n)} \tag{2.42}$$

By expressing the electric field gradient component $V_{x'x'}$, $V_{y'y'}$, etc. in terms of the components of the electric field gradient tensor measured relative to a crystal coordinate system xyz (Nye, 1957), it is found that, in general, W_1 and W_2 can be written as linear combinations of the components of symmetric fourth-rank tensors (Snyder and Hughes, 1971; Hughes, 1973)

$$M_{\alpha\beta\alpha'\beta'}(\mu,m) = \frac{2\pi}{\hbar} \times \frac{\sum_{nn'} \exp(-\beta E_n) \langle n'|V_{\alpha\beta}|n\rangle^{*} \langle n'|V_{\alpha'\beta'}|n\rangle \delta(E_n - E_{n'} + E_{m+\mu} - E_m)}{\sum_n \exp(-\beta E_n)} \tag{2.43}$$

where $\alpha, \beta, \alpha', \beta' = x, y, z$ and $\mu=1$ refers to W_1 and $\mu=2$ refers to W_2. In what follows, we replace $M_{\alpha\beta\alpha'\beta'}(\mu,m)$ by $M_{\alpha\beta\alpha'\beta'}$, it being understood that the M components in general depend on μ and m.

It can be shown (Hughes, 1973) that, for magnetic fields realizable in the laboratory, the M-tensor components in nonmagnetic crystals are real because of time reversal invariance. It then follows from Eq. (2.43) that

$$M_{\alpha\beta\alpha'\beta'} = M_{\beta\alpha\alpha'\beta'} = M_{\alpha\beta\beta'\alpha'} = M_{\alpha'\beta'\alpha\beta} \; . \tag{2.44}$$

Moreover, we find from Laplace's equation that

$$\sum_{\alpha} M_{\alpha\alpha\alpha'\beta'} = \sum_{\alpha'} M_{\alpha\beta\alpha'\alpha'} = 0 \; . \tag{2.45}$$

Eqs. (2.44) and (2.45) imply that the number of independent tensor components is reduced from eighty-one to fifteen.

The presence of crystal symmetry reduces still further the number of independent components, and Snyder and Hughes (1971) have given the orientation dependence of W_1 and W_2 for the various point group symmetries.

If the quadrupole relaxation is caused by the diffusion of charged defects (Cohen and Reif, 1957) or the torsional motion of molecular or ionic groups (Bayer, 1951; Das and Hahn, 1958), it is convenient to treat the field gradient components as stationary random functions of time (Slichter, 1980). It can be shown that the orientation dependence of W_1 and W_2 is of the same general form as given by Snyder and Hughes (1971) and the M-tensor components are defined as

$$M_{\alpha\beta\alpha'\beta'}(\mu,m) = \frac{1}{\hbar^2} \int_{-\infty}^{\alpha} \overline{V_{\alpha\beta}(t+\tau)V_{\alpha'\beta'}(t)} \exp\{-i(E_{m+\mu}-E_m)\tau/\hbar\} d\tau \tag{2.46}$$

where the bar signifies an ensemble average. From time reversal symmetry, the correlation function $\overline{V_{\alpha\beta}(t+\tau)V_{\alpha'\beta'}(t)}$ is an even function of τ, and the M-tensor components are again real and Eqs. (2.44) and (2.45) remain valid.

We note from Eqs. (2.43) and (2.46) that each M-tensor component has, in general, a different value for W_1 and for W_2 on account of μ which appear in the delta function. It is therefore convenient to distinguish between two types of relaxation processes: Type A where the M components are independent of μ and m; and Type B where the M components depend on μ and m.

In crystals where the spin-lattice relaxation is caused by lattice vibrations, the interaction is believed to occur via a Raman type interaction with phonons. Originally, it was believed (Van Kranendonk, 1954) that the interaction was a first order harmonic Raman process involving fluctuations in the electric field gradient tensor components which are quadratic in the atomic displacements. It was later proposed (Van Kranendonk and Walker, 1967; Van Kranendonk and Walker, 1968) that the dominant interaction is a first-order anharmonic Raman process involving fluctuations in the electric field tensor components which are linear in the atomic displacements. Except at the lowest temperatures, most of the phonons involved in the relaxation process have high energies and frequencies. In that case, the nuclear magnetic energy difference $|E_{m+\mu} - E_m|$ is negligible in comparison with typical phonon energies. The μ-dependence in Eq. (2.43) therefore disappears and so Raman type relaxation processes can be expected to be of Type A. The relaxation caused by the diffusion of charged defects and the torsional motion of molecular and ionic groups also corresponds to Type A provided the correlation time is sufficiently short. This can be seen by assuming (Landau and Lifshitz, 1958) that the correlation function $\overline{V_{\alpha\beta}(t+\tau)V_{\alpha'\beta'}(t)}$ varies exponentially with τ so that

$$\overline{V_{\alpha\beta}(t+\tau)V_{\alpha'\beta'}(t)} = \overline{V_{\alpha\beta}(t)V_{\alpha'\beta'}(t)}\ \exp(-|\tau|/\tau_c). \qquad (2.47)$$

Using Eqs. (2.46) and (2.47), it can be shown that

$$M_{\alpha\beta\alpha'\beta} = \overline{V_{\alpha\beta}(t)V_{\alpha'\beta'}(t)}2\tau_c[1 + (E_{m+\mu}-E_m)^2\tau_c^2/\hbar^2] \quad . \qquad (2.48)$$

This expression is independent of μ in the short correlation time limit

$$\tau_c << \hbar/|E_{m+\mu} - E_m| \quad . \qquad (2.49)$$

In the so-called direct process, a single low energy phonon is either emitted or absorbed. Such a process would only be expected to be significant at very low (liquid helium) temperatures and to our knowledge has not been observed because of competing relaxation mechanisms. However, if it did occur, the direct process would be of Type B since the density of phonon states contributing to W_1 processes would be significantly larger than the density of phonon states contributing to W_2 processes, because of the different phonon energies involved. The diffusion and torsional motion relaxation processes also belong to Type B if the correlation time is sufficiently long as can be seen from Eq. (2.48). Though the M components in Type B processes necessarily depend on μ, they will be essentially independent of m in cases where the static quadrupole interaction is much smaller than the Zeeman interaction.

2.2.4 Calculation of the ratios of the M-tensor component using a point-charge model

The only calculations of the ratios of the M-tensor seem to be those of Hughes and Reed (1971) and Hughes and Spencer (1982). In the work of Hughes and Spencer, the relaxing nucleus is assumed to be surrounded by an array point charges $q_1, \ldots, q_n$, and the quadrupole relaxation is assumed to depend on fluctuations in the electric field gradient which are linear in the relative displacements of the nucleus and the surrounding point charges. Such a linear dependence is expected if the relaxation is caused by the anharmonic Raman process (Van Kranendonk and Walker, 1967; Van Kranendonk and Walker, 1968) for example. A linear dependence should also be expected in the classical limit, provided the displacement of neighbouring ions relative to the nucleus involved is much smaller than the distance from the ions to the nucleus.

The increase in the electric field gradient component $V_{\alpha\beta} = \partial^2 V/\partial x_\alpha \partial x_\beta$ at the nuclear site, which is linear in the displacements, is given by

$$\delta V_{\alpha\beta} = \sum_{j=1}^{3} \Big(\sum_{i=1}^{n} \frac{3q_i}{r_i^7} \big[(\delta_{\alpha j} x_{\beta i} + \delta_{\beta j} x_{\alpha i} + \delta_{\alpha\beta} x_{ji}) r_i^2 - 5 x_{ji} x_{\alpha i} x_{\beta i}\big](dx_{ji} - dx_{jo}) \Big) . \qquad (2.50)$$

Here, r_i is the distance of the ith charge from the nucleus, x_{ji} is the x_j coordinate of the ith charge measured from the nucleus, dx_{ji} is the displacement of the ith charge in the x_j direction and dx_{jo} is the displacement of the nucleus in the x_j direction. We assume that $M_{\alpha\beta\alpha'\beta'}$ is proportional to $\overline{\delta V_{\alpha\beta}\delta V_{\alpha'\beta'}}$ where the bar signifies the time average. (This assumes that the various electric field gradient components $V_{\alpha\beta}$ experience essentially the same statistical time dependence.) If the displacements of the nucleus and the surrounding n charges are all uncorrelated, it follows that

$$\begin{aligned}
M_{\alpha\beta\alpha'\beta'} \sim \sum_{j=1}^{3} \Big(& \sum_{i=1}^{n} \frac{9q_i^2}{r_i^{14}} [(\delta_{\alpha j}x_{\beta i}+\delta_{\beta j}x_{\alpha i}+\delta_{\alpha\beta}x_{ji})r_i^2-5x_{ji}x_{\alpha i}x_{\beta i}] \\
& \times [(\delta_{i'j}x_{\beta' i}+\delta_{\beta' j}x_{\alpha' i}+\delta_{\alpha'\beta'}x_{ji})r_i^2-5x_{ji}x_{\alpha' i}x_{\beta' i}]\overline{(dx_{ji})^2} \\
& + \Big(\sum_{i=1}^{n} \frac{3q_i}{r_i^7} [(\delta_{\alpha j}x_{\beta i}+\delta_{\beta j}x_{\alpha i}+ \delta_{\alpha\beta}x_{ji})r_i^2-5x_{ji}x_{\alpha i}x_{\beta i}]\Big) \\
& \times \Big(\sum_{i=1}^{n} \frac{3q_i}{r_i^7} [(\delta_{\alpha' j}x_{\beta' i}+\delta_{\beta' j}x_{\alpha' i}+\delta_{\alpha'\beta'}x_{ji})r_i^2-5x_{ji}x_{\alpha' i}x_{\beta' i}]\Big) \\
& \times \overline{(dx_{jo})^2} \; . \qquad (2.51)
\end{aligned}$$

2.3 Time dependent behaviour of a system of I=3/2 nuclei experiencing first-order quadrupole splitting

2.3.1 Quadrupole relaxation

The allowed quadrupole relaxation transitions for a system of identical I = 3/2 nuclei experiencing first-order quadrupole splitting are shown in Fig. 2.4(a). The downward transition probabilities are related to the corresponding upward transition probabilities by the Boltzmann factor which can be written, in the high-temperature approximation, as $1+\Delta E/kT$ where ΔE is the difference between the energies of the two levels involved. The frequencies of the centre line and the $m = 3/2 \leftrightarrow 1/2$ and $m = -1/2 \leftrightarrow -3/2$ satellites respectively are given, in first order (see second term on RHS of Eq. (2.34)), by ν_o, $\nu_o(1+\delta)$ and $\nu_o(1-\delta)$ where $\delta = -(e^2qQ)/4h\nu_o)\ (3\cos^2\theta-1+\eta\sin^2\theta\cos 2\phi)$. It follows that if the upward transition probabilities are written as W_1 and W_2, then the downward transition probabilities are $W_1(1+\Delta_+)$, $W_1(1+\Delta_-)$, $W_2(1+\Delta+\Delta_+)$ and $W_2(1+\Delta+\Delta_-)$, as shown in Fig. 2.4(a)), where $\Delta = h\nu_o/kT$, $\Delta_+ = \Delta(1+\delta)$ and $\Delta_- = \Delta(1-\delta)$. We now derive the time-dependent behaviour of the nuclear spin system. Our treatment differs from that found in the literature (Andrew and Tunstall, 1961) by taking into account the unequal energy level spacings i.e. the quadrupole splitting.

In the absence of externally applied rf fields, the rate equations are:-

$$\frac{dN_{3/2}}{dt} = -N_{3/2}(W_1+W_2)+N_{1/2}W_1(1+\Delta_+)+N_{-1/2}W_2(1+\Delta+\Delta_+) \qquad (2.52)$$

$$\frac{dN_{1/2}}{dt} = N_{3/2}W_1-N_{1/2}\{W_2+W_1(1+\Delta_+)\}+N_{-3/2}W_2(1+\Delta+\Delta_-) \qquad (2.53)$$

Figure 2.4

Energy level diagram for a system of nuclei with I = 3/2 showing (a) quadrupole transitions (b) magnetic transitions.

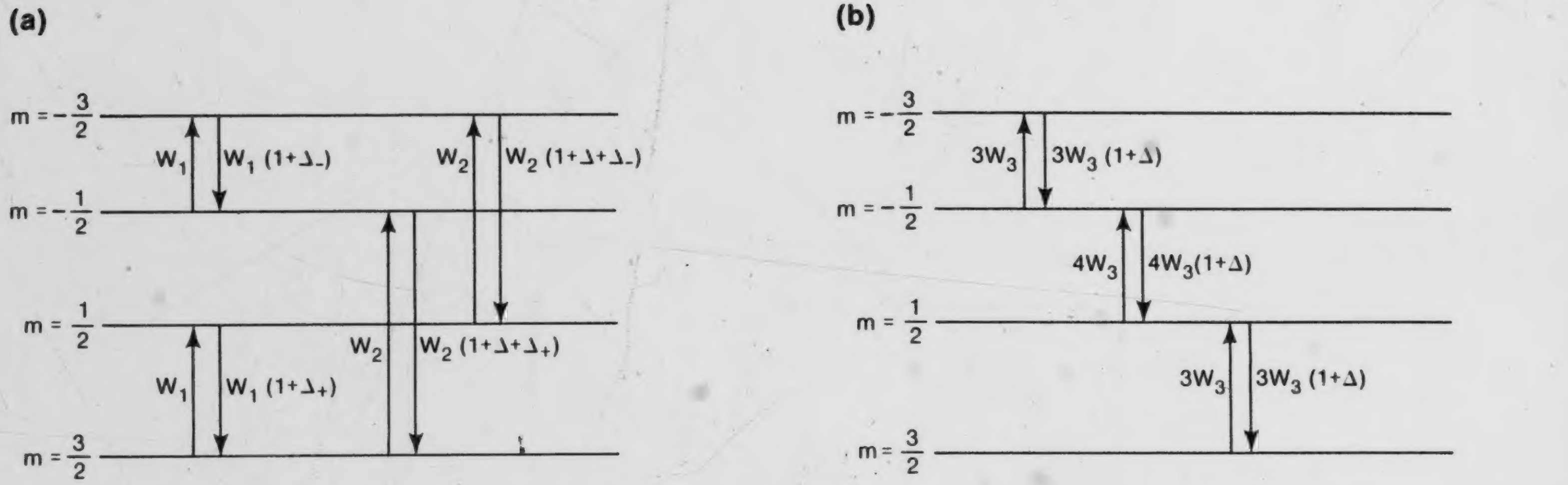
(a)
$m = -\frac{3}{2}$
$m = -\frac{1}{2}$
$m = \frac{1}{2}$
$m = \frac{3}{2}$
W_1
$W_1\ (1+\Delta_-)$
W_1
$W_1\ (1+\Delta_+)$
W_2
$W_2\ (1+\Delta+\Delta_-)$
W_2
$W_2\ (1+\Delta+\Delta_+)$
(b)
$m = -\frac{3}{2}$
$m = -\frac{1}{2}$
$m = \frac{1}{2}$
$m = \frac{3}{2}$
$3W_3$
$3W_3\ (1+\Delta)$
$4W_3$
$4W_3(1+\Delta)$
$3W_3$
$3W_3\ (1+\Delta)$

$$\frac{dN_{-1/2}}{dt} = N_{3/2}W_2 - N_{-1/2}\{W_1 + W_2(1+\Delta+\Delta_+)\} + N_{-3/2}W_1(1+\Delta_-) \quad (2.54)$$

$$\frac{dN_{-3/2}}{dt} = N_{1/2}W_2 + N_{-1/2}W_1 - N_{-3/2}\{W_1(1+\Delta_-) + W_2(1+\Delta+\Delta_-)\} \quad (2.55)$$

where $N_{3/2}$, $N_{1/2}$, $N_{-1/2}$ and $N_{-3/2}$ are the populations of the states m = 3/2, 1/2, -1/2 and -3/2 respectively. If we denote the population differences $N_{3/2}-N_{1/2}$, $N_{1/2}-N_{-1/2}$ and $N_{-1/2}-N_{-3/2}$ by N_{+1}, N_o and N_{-1} respectively, we can write

$$\frac{dN_{+1}}{dt} = -(2W_1+W_2)\{N_{+1}-n_o(1+\delta)\} + W_2\{N_{-1}-n_o(1-\delta)\} \quad (2.56)$$

$$\frac{dN_o}{dt} = (W_1-W_2)\{N_{+1}-n_o(1+\delta)\} - 2W_2(N_o-n_o) + (W_1-W_2) \times \{N_{-1}-n_o(1-\delta)\} \quad (2.57)$$

$$\frac{dN_{-1}}{dt} = W_2\{N_{+1}-n_o(1+\delta)\} - (2W_1+W_2)\{N_1 - n_o(1-\delta)\} , \quad (2.58)$$

where n_o, $n_o(1+\delta)$ and $n_o(1-\delta)$ are the population differences of N_o, N_{+1} and N_{-1} respectively at thermal equilibrium. Now if we let $N'_{+1} = N_{+1}-n_o(1+\delta)$, $N'_o = N_o-n_o$ and $N'_{-1} = N_{-1}-n_o(1-\delta)$, so that the primed quantities represent deviations from the thermal equilibrium values, we can rewrite Eqs. (2.56), (2.57) and (2.58) in the form

$$\frac{dN_{+1}}{dt} = -(2W_1+W_2)N'_{+1} + W_2N'_{-1} \quad (2.59)$$

$$\frac{dN'_o}{dt} = (W_1-W_2)N'_{+1} - 2W_2N'_o + (W_1-W_2)N'_{-1} \quad (2.60)$$

$$\frac{dN'_{-1}}{dt} = W_2N'_{+1} - (2W_1+W_2)N'_{-1} \quad . \quad (2.61)$$

The general solution of these homogeneous first-order differential equations is

$$N'_o = Ae^{-2W_1t} + Be^{-2W_2t} \tag{2.62}$$

$$N'_{+1} = -Ae^{-2W_1t} - Ce^{-2(W_1+W_2)t} \tag{2.63}$$

$$N'_{-1} = -Ae^{-2W_1t} + Ce^{-2(W_1+W_2)t} \tag{2.64}$$

where the coefficients A, B and C depend on the initial conditions.

Suppose that the spin system is in thermal equilibrium and the centre line is suddenly irradiated by a selective pulse (i.e. one that does not perturb the satellites). It can be shown that the recovery of the population differences is then given by

$$N'_o = -D(e^{-2W_1t} + e^{-2W_2t}) \tag{2.65}$$

$$N'_{\pm1} = De^{-2W_1t} \tag{2.66}$$

where D is a constant which depends on the excitation. For example, if the centre line is completely saturated or is subjected to an ideal 90° pulse so that N_o becomes 0, D is equal to $n_o/2$. If it is subjected to an ideal 180° pulse, so that N_o becomes $-n_o$, then D is equal to n_o.

Suppose instead that the $m = 3/2 \leftrightarrow 1/2$ satellite is suddenly irradiated by a selective pulse when the spin system is in thermal equilibrium. The recovery of the population differences is then of the form

$$N'_o = Ee^{-2W_1t} \tag{2.67}$$

$$N'_{+1} = -E(e^{-2W_1t} + e^{-2(W_1+W_2)t}) \tag{2.68}$$

$$N'_{-1} = -E(e^{-2W_1t} - e^{-2(W_1+W_2)t}) \tag{2.69}$$

where E is a constant which depends on the excitation. For example, if the satellite is subjected to an ideal 90° pulse, then E is $n_o(1-\delta)/2$. If it is subjected to an ideal 180° pulse then E is $n_o(1-\delta)$.

It can be seen from Eqs. (2.62) to (2.69) that the unequal energy level spacings have no effect on the time-dependent behaviour of the spin system. This is in contrast to the situation in the enhancement method of measuring W_2/W_1 (Hughes and Reed, 1971; Spencer and Hughes, 1978). In that case, where resonance amplitudes are measured, it is necessary to take quadrupole splittings into account.

2.3.2 Magnetic relaxation

In this section we consider the magnetic spin-lattice relaxation of I = 3/2 nuclei experiencing first-order quadrupole splitting. Our treatment is a generalization of that previously given by Andrew and Tunstall (1961). As was done by these authors we assume that the relaxation is homogeneous, i.e. is the same at all nuclei. The upward magnetic relaxation probability may be written as

$$W_{m\to m-1} = W_3(I+m)(I-m+1) \qquad (2.70)$$

where W_3 is independent of m for the nuclei involved. The corresponding downward transition probability is given in the high temperature approximation by Eq. (2.70) multiplied by the Boltzmann factor $(1+\Delta)$, where $\Delta = h\nu_o/kT$ and ν_o is the unperturbed resonance frequency. (As was seen in section 2.3.1, it is not necessary to take into account the unequal energy level spacings.) The transitions which occur in the case $I = 3/2$ are shown in Fig. 2.4(b).

In the absence of externally applied rf fields, the rate equations can be written as

$$\frac{dN_{-3/2}}{dt} = 3W_3N_{-1/2} - 3W_3(1+\Delta)N_{-3/2} \tag{2.71}$$

$$\frac{dN_{-1/2}}{dt} = -(3W_3+4W_3(1+\Delta))N_{-1/2}+3W_3(1+\Delta)N_{-3/2}+4W_3N_{1/2} \tag{2.72}$$

$$\frac{dN_{1/2}}{dt} = -(4W_3+3W_3(1+\Delta))N_{1/2}+4W_3(1+\Delta)N_{-1/2}+3W_3N_{3/2} \tag{2.73}$$

$$\frac{dN_{3/2}}{dt} = -3W_3N_{3/2} + 3W_3(1+\Delta)N_{1/2} \; . \tag{2.74}$$

Using a procedure similar to that used in section 2.3.1 it is found that

$$\frac{dN'_{-1}}{dt} = 4W_3N'_o - 6W_3N'_{-1} \tag{2.75}$$

$$\frac{dN'_o}{dt} = 3W_3N'_{+1} + 3W_3N'_{-1} - 8W_3N'_o \tag{2.76}$$

$$\frac{dN'_{+1}}{dt} = 4W_3N'_o - 6W_3N'_{+1} \; , \tag{2.77}$$

for which the general solution is

$$N'_{-1} = Ae^{-6W_3t} + Be^{-2W_3t} + Ce^{-12W_3t} \tag{2.78}$$

$$N'_o = \frac{3}{2}(A+D)e^{-6W_3t} + Be^{-2W_3t} - \frac{3}{2}Ce^{-12W_3t} \tag{2.79}$$

$$N'_{+1} = De^{-6W_3t} + Be^{-2W_3t} + Ce^{-12W_3t} \; . \tag{2.80}$$

Here, A,B,C and D are constants depending on the initial conditions. If the spin system is initially in thermal equilibrium and the centre line is suddenly excited by a selective pulse, the recovery of the population differences can be shown to be given by

$$N'_o = E(e^{-2W_3t} + 9e^{-12W_3t}) \qquad (2.81)$$

$$N'_{\pm 1} = E(e^{-2W_3t} - 6e^{-12W_3t}) \qquad (2.82)$$

where E is a constant which depends on the excitation. For example, if the centre line is subjected to an ideal 180° pulse, E is $-n_o/5$. We see that the recovery of the centre line and satellites is nonexponential.

A case which we consider later in this thesis is where nuclei relax via a magnetic interaction with a relatively small number of electronic paramagnetic spins. In this case, the direct spin-lattice relaxation will be inhomogeneous i.e. will be different for different spins. However, because of spin diffusion (Bloembergen, 1949; Abragam, 1961) arising from the coupling together of nuclear spins via the interaction of their magnetic dipoles, the inhomogeneity in the relaxation may be small enough to ignore. The theory just presented should therefore cover that case. However, if the crystal contains enough defects or strains so that the first-order quadrupole splitting varies significantly from one nucleus to its neighbours,then spin diffusion occurring via the satellites will be inhibited i.e. so-called flip-flop transitions in which one nucleus undergoes a transition from the state m = +3/2 to m = +1/2 say and a neighbour goes from m = +1/2 to +3/2 will be inhibited. In that case, it can be assumed that no transitions occur between levels m = ±3/2 and ±1/2 by interaction with the paramagnetic spins, so that the only magnetic transitions that occur are between the states m = +1/2 and -1/2 with a probability $4W_3$. We now consider that case since, to our knowledge, it has not been treated in the literature.

We again assume that the magnetic relaxation is homogeneous. In the absence of externally applied rf fields, the rate equations can be written as

$$\frac{dN_{3/2}}{dt} = 0 \tag{2.83}$$

$$\frac{dN_{-3/2}}{dt} = 0 \tag{2.84}$$

$$\frac{dN_{1/2}}{dt} = 4W_3(1+\Delta)N_{-1/2} - 4W_3N_{1/2} \tag{2.85}$$

$$\frac{dN_{-1/2}}{dt} = 4W_3N_{1/2} - 4W_3(1+\Delta)N_{-1/2} \; . \tag{2.86}$$

Using a procedure similar to that used in section 2.3.1, it is found that

$$\frac{dN'_{+1}}{dt} = 4W_3N'_o \tag{2.87}$$

$$\frac{dN'_o}{dt} = -8W_3N'_o \tag{2.88}$$

$$\frac{dN'_{-1}}{dt} = 4W_3N'_o \; . \tag{2.89}$$

If the spin system is initially in thermal equilibrium and the centre line is suddenly excited by a selective 180° pulse, the recovery of the population differences can be shown to be

$$N'_{\pm 1} = n_o e^{-8W_3t} \tag{2.90}$$

$$N'_o = -2n_o e^{-8W_3t} \; . \tag{2.91}$$

2.3.3 Quadrupole and magnetic relaxation

The time dependent behaviour of a $I = 3/2$ spin system in the presence of quadrupole splitting, and magnetic and quadrupole relaxation has been treated by Niemelä (1967). However, he included all the magnetic transitions shown in Fig. 2.4(b). We encounter later a situation where the magnetic transitions between the levels $m = \pm 3/2$ and $m = \pm 1/2$ seem to be inhibited. We therefore consider the case of a system of $I = 3/2$ nuclei experiencing both quadrupole and magnetic relaxation, but with the magnetic transitions being only between the levels $m = +1/2$ and $m = -1/2$.

In the absence of externally applied rf fields, it can be shown that the rate equations are

$$\frac{dN'_{+1}}{dt} = W_2N'_{-1} + 4W_3N'_o - (2W_1+W_2)N'_{+1} \qquad (2.92)$$

$$\frac{dN'_o}{dt} = (W_1-W_2)N'_{-1} - (2W_2+8W_3)N'_o + (W_1-W_2)N'_{+1} \qquad (2.93)$$

$$\frac{dN'_{-1}}{dt} = W_2W_{+1} + 4W_3N'_o - (2W_1+W_2)N'_{-1} \qquad (2.94)$$

We are interested only in the case where both satellites are perturbed equally by the initial excitation. In that case, N'_1 must equal N'_{-1} initially, and they will remain equal afterwards because of the symmetry of Eqs. (2.92) and (2.94). The general solution of Eqs. (2.92) to (2.94) is in that case

$$N'_o = Ae^{\lambda_1 t} + Be^{\lambda_2 t} \qquad (2.95)$$

$$N'_{\pm 1} = Ce^{\lambda_1 t} + De^{\lambda_2 t} \qquad (2.96)$$

where

$$\lambda_1 = -(W_1 + W_2 + 4W_3) + P \qquad (2.97)$$

$$\lambda_2 = -(W_1 + W_2 + 4W_3) - P \qquad (2.98)$$

$$C = A[(W_2 - W_1 + 4W_3 + P)/2(W_1 - W_2)] \qquad (2.99)$$

$$D = B[(W_2 - W_1 + 4W_3 - P)/2(W_1 - W_2)] \qquad (2.100)$$

$$P = [(W_1 - W_2)^2 + 16W_3^2]^{1/2} \qquad (2.101)$$

Here, A and B are arbitrary constants depending on the initial conditions. If the centre line alone is excited initially, then $N_o' = -2N_{\pm 1}$ at $t = 0$ and the recovery of the spin system is given by

$$N_o' = E[(4W_3 - P)/P]e^{\lambda_1 t} - E[(4W_3 + P/P]e^{\lambda_2 t} \qquad (2.102)$$

$$\begin{aligned} N_{\pm 1} &= E[(W_2 - W_1 + 4W_3 + P)(4W_3 - P)/2(W_1 - W_2)P]e^{\lambda_1 t} \\ &\quad - E(W_2 - W_1 + 4W_3 - P)(4W_3 + P)/2(W_1 - W_2)P]e^{\lambda_2 t} \end{aligned} \qquad (2.103)$$

where E is a constant. The recovery of the spin system is clearly nonexponential in this case. However, it is useful to apply Eqs. (2.102) and (2.103) to two extreme cases.

Consider first the case $(W_1 - W_2) << 16W_3^2$ where the magnetic relaxation is dominant. The recovery of the centre line and satellites is then exponential of the form

$$N_1' = Fe^{-(W_1 + W_2 + 8W_3)t} \qquad (2.104)$$

$$N_o' = -2Fe^{-(W_1 + W_2 + 8W_3)t} \qquad (2.105)$$

If we further assume that W_1 and W_2 are not very different from one another, then

$$N_1' \approx Ee^{-2(W_1 + 4W_2)t} \qquad (2.106)$$

$$N_o' \simeq -2Ee^{-2(W_1+4W_2)t} \qquad (2.107)$$

in which case the relaxation rate of the satellites is simply the sum of the quadrupolar rate $2W_1$ and the magnetic rate $8W_3$.

Consider now the other extreme case $(W_1-W_2)^2 \gg 16W_3^2$ where the quadrupole relaxation is dominant. The time dependent behaviour is now given by

$$N_1' \simeq Ge^{-2(W_1+2W_3)t} \qquad (2.108)$$

$$N_o' \simeq -G(e^{-2(W_1+2W_3)t} + e^{-2(W_2+2W_3)t}) \qquad (2.109)$$

Here, the relaxation of the satellites is exponential, the rate being the sum of the quadrupolar rate $2W_1$ and half the magnetic rate $4W_3$.

CHAPTER 3

CRYSTAL STRUCTURE OF $NaNO_2$; QUADRUPOLE SPLITTING AND QUADRUPOLE RELAXATION OF ^{23}Na IN A $NaNO_2$ SINGLE CRYSTAL

3.1 Crystal structure of $NaNO_2$

$NaNO_2$ belongs to the body-centered orthorhombic system, space group Imm2-C_{2v}^{20} at room temperature (Ziegler, 1931). The unit cell is shown in Fig. 3.1. There are two molecules per unit cell and two mirror planes perpendicular to the $\underset{\sim}{a}$ and $\underset{\sim}{c}$ axes respectively. The unit cell dimensions at room temperature are $\underset{\sim}{a}$ = 3.560±0.010 Å, $\underset{\sim}{b}$ = 5.563±0.005 Å, $\underset{\sim}{c}$ = 5.384±0.005 Å (Kay and Frazer, 1961). The ferroelectricity of $NaNO_2$ comes from the ordered arrangement of NO_2 groups and the spontaneous polarization is parallel to the $\underset{\sim}{b}$ axis (Sawada et al., 1958).

$NaNO_2$ undergoes a first-order transition at T≈437 K from the ferroelectric phase to an antiferroelectric phase which exists only over a very small temperature range (~1°C). In this phase, the average electric dipole moment along the $\underset{\sim}{b}$ axis displays a sinusoidal modulation along the $\underset{\sim}{a}$ axis with a period of about $8\underset{\sim}{a}$ (Yamada et al, 1963; Yamada and Yamada, 1966). At a temperature T≈438 K, a further transition occurs from the antiferroelectric phase to a paraelectric phase characterized by a space group Immm-D_{2h}^{25}. In the latter phase, the NO_2 groups are

Figure 3.1

Unit cell of sodium nitrite and the crystal coordinate system used to denote the orientation of magnetic field $\vec{H}_o$

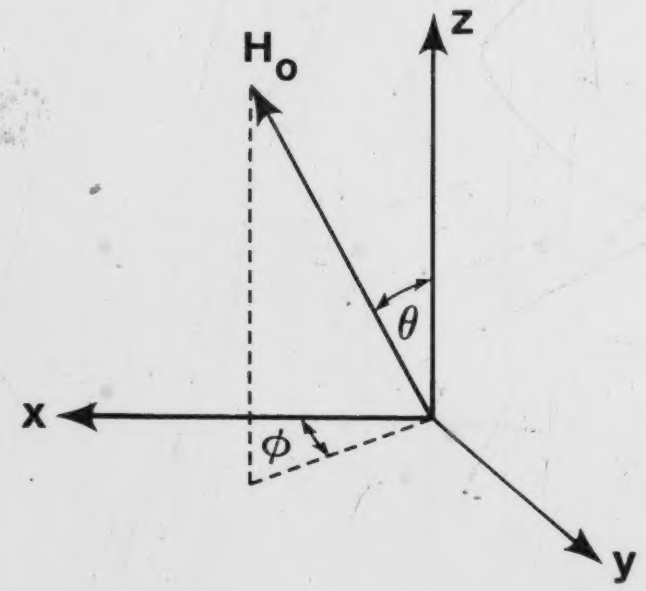
H$_o$
z
θ
x
ϕ
y

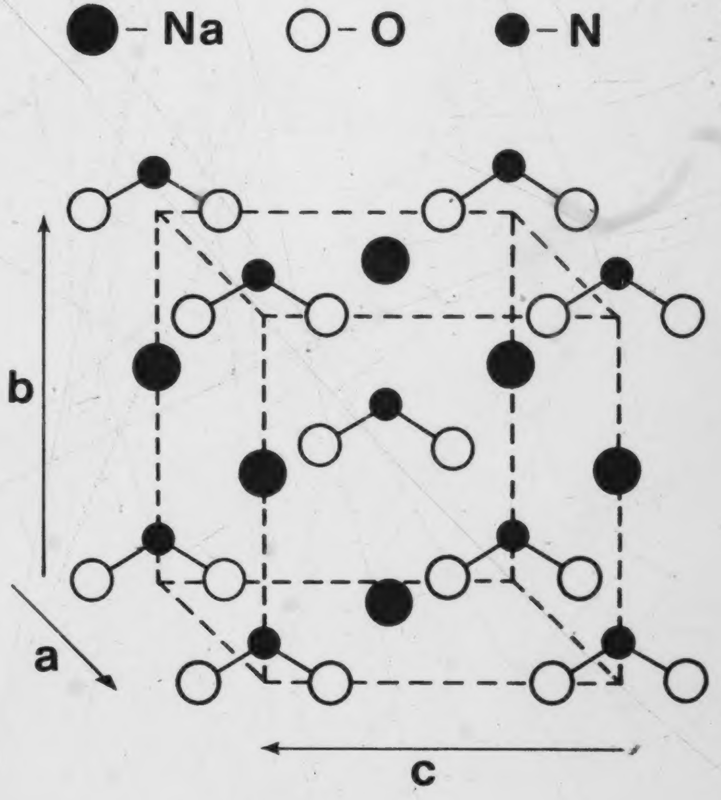
● – Na
○ – O
• – N
b
a
c

completely disordered and have an equal probability of pointing along the +$\underset{\sim}{b}$ and -$\underset{\sim}{b}$ axes.

3.2 Orientation dependence of the ^{23}Na quadrupole splitting in NaNO$_2$

The sodium sites in NaNO$_2$ are all identical. Since ^{23}Na has a spin of 3/2, there are therefore three ^{23}Na resonances observed in a single crystal of this material. As can be seen from Eq. (2.34), in first order the centre line corresponding to the transition $m = +1/2 \leftrightarrow -1/2$ is unaffected by the quadrupole interaction, and the frequencies of the satellites corresponding to the $m = \pm 3/2 \leftrightarrow \pm 1/2$ transitions are given by

$$\nu_{\pm} = \nu_o \mp \frac{e^2qQ}{4h} (3\cos^2\theta - 1 + \eta\sin^2\theta\cos 2\phi) \ . \qquad (3.1)$$

The crystal coordinate system is such that the x,y and z axes are parallel to the $\underset{\sim}{c}$, $\underset{\sim}{a}$ and $\underset{\sim}{b}$ crystalline axes respectively (Weiss, 1960) as shown in Fig. 3.1. The nuclear quadrupole coupling constant e^2qQ/h varies from 1100 kHz at 18°C to 749 kHz at 215°C (Weiss and Biedenkapp, 1962). The asymmetry parameter η varies from 0.11 at 18°C to zero at the transition temperature. Above the transition temperature, the asymmetry is in the opposite sense so that the smallest quadrupole splitting now occurs when the magnetic field is parallel to the $\underset{\sim}{a}$ axis instead of the $\underset{\sim}{c}$ axis.

At the magnetic field strengths used in our work, second order quadrupole effects are significant. It can be shown using Eq. (2.34) that the frequencies of the centre line and satellites of ^{23}Na in $NaNO_2$ are given, in second order, by

$$\nu_c = \nu_o - \frac{e^4q^2Q^2}{192h^2\nu_o}\left[9\sin^2\theta(9\cos^2\theta-1)-6\eta\sin^2\theta\cos2\phi(10-9\sin^2\theta)\right.$$

$$\left.-4\eta^2(1-3\sin^2\theta+\frac{9}{4}\sin^4\theta\cos2\phi)\right] \qquad (3.2)$$

$$\nu_\pm = \nu_o \mp \frac{e^2qQ}{4h}(3\cos^2\theta-1+\eta\sin^2\theta\cos2\phi) + \frac{e^4q^2Q^2}{24h^2\nu_o}\left\{\frac{9}{4}\sin^22\theta\right.$$

$$\left.-\frac{3}{2}\eta(\sin^22\theta\cos2\phi)+\eta^2\sin^2\theta(1-\sin^2\theta\cos^22\phi)\right\} . \qquad (3.3)$$

3.3 Orientation dependence of the ^{23}Na quadrupole relaxation in $NaNO_2$

The orientation dependence of the quadrupole transition probabilities W_1 and W_2 of nuclei at sites possessing mm2 or mmm point group symmetry is given by (Snyder and Hughes, 1971)

$$W_1 = (e^2Q^2/96)\left[4M_{1111}+4M_{1133}+M_{3333}+4M_{2323}+4M_{3131}+4M_{1212}\right.$$

$$+6(3M_{3333}-2M_{2323}-2M_{3131})\cos^2\theta$$

$$-(4M_{1111}+4M_{1133}+19M_{3333}-16M_{2323}-16M_{3131}+4M_{1212})$$

$$\times\cos^4\theta-12(2M_{1133}+M_{3333})\cos2\phi\sin^2\theta\cos^2\theta$$

$$-4(M_{2323}-M_{3131})\cos2\phi\sin^2\theta(1-4\cos^2\theta)$$

$$\left.-(4M_{1111}+4M_{1133}+M_{3333}-4M_{1212})\cos4\phi\sin^4\theta\right] \qquad (3.4)$$

$$\begin{aligned}
W_2 = (e^2Q^2/96)[&4M_{1111}+4M_{1133}+\frac{19}{4}M_{3333}+4M_{2323}+4M_{3131}+4M_{1212} \\
&+ 6(M_{3333}+M_{2323}-\frac{5}{4}M_{3333}M_{1212})\cos^2\theta \\
&+ (M_{1111}+M_{1133}+\frac{19}{4}M_{3333}-4M_{2323}-4M_{3131}+M_{1212})\cos^4\theta \\
&+ 3(2M_{1133}+M_{3333})\cos 2\phi\sin^2\theta(1+\cos^2\theta) \\
&+ 4(M_{2323}-M_{3131})\cos 2\phi\sin^4\theta \\
&+ (M_{1111}+M_{1133}+\frac{1}{4}M_{3333}-M_{1212})\cos 4\phi\sin^4\theta] \qquad (3.5)
\end{aligned}$$

provided the relaxation is homogeneous i.e. is the same at each sodium site. The form of the orientation dependence of W_1 and W_2 should therefore be the same in the paraelectric phase as in the ferroelectric phase. In Eqs. (3.4) and (3.5), the z axis is the 2-fold axis and the x and y axes lie in the mirror planes (Snyder and Hughes, 1971). For convenience, we choose the x and y axes to lie along the $\underset{\sim}{c}$ and $\underset{\sim}{a}$ axes respectively, so that our coordinate system coincides with that used to describe the quadrupole splitting below the transition temperature (Weiss, 1960; Weiss and Biedenkapp, 1962).

CHAPTER 4

EXPERIMENTAL DETAILS

4.1 Equipment

4.1.1 Pulsed DNMR spectrometer

In this section we briefly describe the various parts of the equipment and their functional relationships. Important parts of the apparatus are described in more detail in sections 4.1.2 to 4.1.6.

In our experimental technique, an rf pulse is applied to one of the three quadrupole-split resonances, and a second rf pulse is subsequently applied to one of the other resonances (or, in one version of the experiment, the same resonance) in order to monitor the recovery of the spin system. The block diagram is shown in Fig. 4.1. RF Generator 1, which is a Wavetek 178 Programmable Waveform Synthesizer, provides the excitation signal for the first pulse. Its frequency is set to match the frequency of the resonance to be excited. RF Generator 2, which is a Fluke 6039A Frequency Synthesizer, provides the rf signal for the 90° pulses which are used to monitor the approach to equilibrium of the second resonance. The external magnetic field $\vec{H}_o$ is always set so that the frequency of the second resonance is close to 14.5 MHz. Rectangular gating signals are provided by a digital pulse generator clocked by a 14.5

Figure 4.1

Block diagram of the pulsed DNMR spectrometer

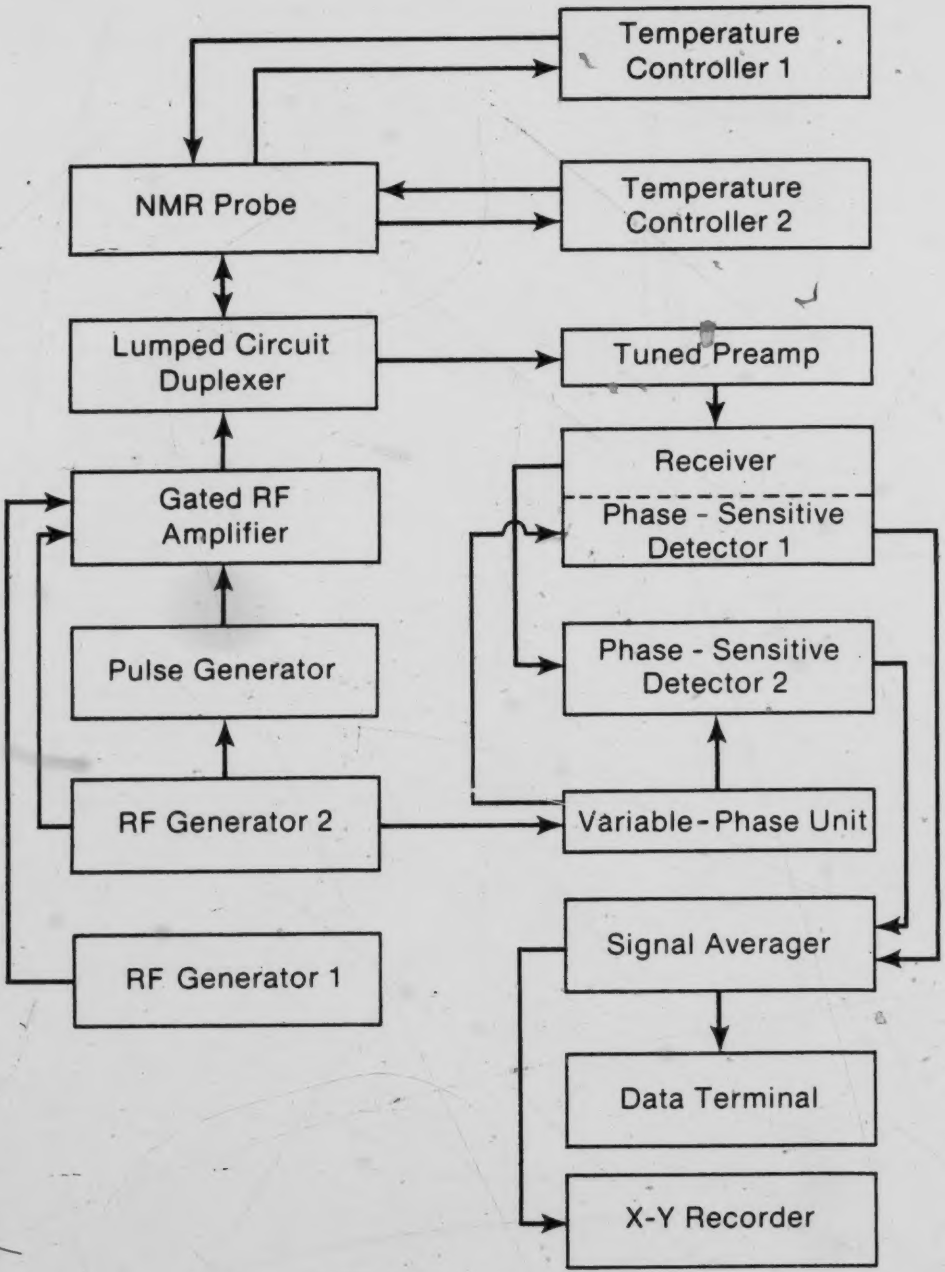
Temperature Controller 1
Temperature Controller 2
NMR Probe
Lumped Circuit Duplexer
Tuned Preamp
Receiver
Phase - Sensitive Detector 1
Gated RF Amplifier
Pulse Generator
Phase - Sensitive Detector 2
RF Generator 2
Variable-Phase Unit
Signal Averager
RF Generator 1
Data Terminal
X-Y Recorder

MHz signal from the Fluke Frequency Synthesizer. The gating signals are fed to the gated rf amplifier, a Matec 515 1 kW amplifier plugged into a Matec 5100 mainframe unit. The high power rf pulses are fed from the amplifier to the probe via a lumped circuit duplexer of the type described by McLachlan (1980). When fed with a large signal, this unit connects the output of the gated rf amplifier directly to the probe, and isolates the input of the detection circuitry. In the absence of large signals, the duplexer connects the probe to the Matec 251 tuned preamplifier, and isolates the output of the gated rf amplifier. The receiver, a Matec 625 Wide-band Receiver, incorporates a phase-sensitive detector, the reference signal being obtained from RF Generator 2 via a variable phase-shift unit. In order to simultaneously record the in-phase and out-of-phase components of the NMR signal, a second phase-sensitive detector, constructed by the departmental Electronics Shop, is used. It incorporates a fine phase-shift control which enables the orthogonality condition to be accurately maintained. The phase-detected NMR signals are fed to a two-channel Nicolet 1170 Signal Averager. The averaged NMR signals can be digitally read out via a Texas Instruments Type 733 ASR electronic data terminal or plotted on a Hewlett-Packard 7004B X-Y recorder.

Two Lakeshore Cryotronics DRC 82C temperature controllers are used to maintain a constant temperature at platinum resistance sensors located above and below the sample.

4.1.2 NMR probe

A single coil arrangement was used in our work. In order to match the probe to the 50 Ω output impedance of the gated rf amplifier and the 50 Ω input impedance of the preamplifier, the circuit shown in Fig. 4.2 was used. A probe impedance of 50 Ω is required for maximum power transfer from the gated rf amplifier and to obtain the best signal-to-noise ratio. Also, reflection problems are avoided by using RG-58 coaxial cable, which has a characteristic impedance of 50 Ω, to connect the various rf units.

The operation of the circuit, which is similar to the one mentioned by Hoult (1978), can be qualitatively understood as follows: Suppose C_2 and R are omitted. The capacitor C_1 can then be adjusted to obtain series resonance with the coil L. The impedance would then be r, the resistance of the coil, and this is usually much smaller than 50 Ω. However, suppose now that C_1 is increased until the real part of the admittance is 1/50 Ω. The imaginary part of the admittance can now be cancelled by suitably adjusting C_2. The total impedance of the circuit is then 50 Ω resistive, as required.

A typical NMR coil has a Q-factor in the range 100 to 200. The decay time of the FID of our ^{23}Na resonances

Figure 4.2

Circuit diagram of the NMR probe

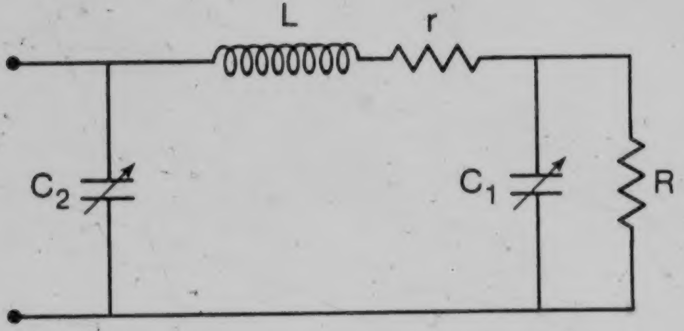
L
r
C2
C1
R

is roughly 100 μs. Thus, in order to record most of the FID following a 90° pulse, it is necessary for the receiver and probe to recover in a time much less than 100 μs. The recovery time of our receiver and preamplifier depends on the operating frequency and is about 6 μs at 14.5 MHz. The "ring down" time of the probe, i.e. the time taken for the rf pulse to decay away to the noise level, depends on the Q of the coil. We found that a Q of roughly 50 gave a satisfactory overall recovery time of about 25 μs. The resistance R across C_1 in Fig. 4.2 was therefore chosen to load the circuit so that a recovery time of roughly 25 μs was obtained.

The voltage across capacitor C_2 is limited to about 300 V, the output of the gated rf amplifier. An ordinary variable air capacitor with a range 13.5 to 320 pF was used for C_2 as there was no danger of dielectric breakdown. A total capacitance of around 500 pF was usually required to "tune" the probe to 50 Ω, and so a fixed capacitor was connected in parallel with the variable air capacitor. The voltage across C_1 during the rf pulse is much larger than the output of the gated rf amplifier because L and C_1 are not far from being in series resonance. In order to avoid the possibility of dielectric breakdown, a 3-30 pF vacuum-variable capacitor, manufactured by ITT Jennings Ltd. and capable of withstanding 9 kV, was used for C_1.

Three different NMR probes were used for the work described in this thesis. The room temperature coil was 0.58 inches long and 0.94 inches in diameter and consisted of 21 turns of 0.006 inch diameter silver wire which gave an inductance of approximately 8 μH. The low temperature coil was 0.53 inches long and 0.94 inches in diameter and consisted of 19 turns of 0.009 inch diameter silver wire which gave an inductance of approximately 7 μH. Silver was used instead of copper because the ^{63}Cu NMR frequency is quite close to that of ^{23}Na. The coil formers were approximately 0.04 inches thick, and had Faraday shields, described in section 4.1.3, glued on the inside. To minimize the danger of dielectric breakdown from the high voltage end of the coil to the grounded Faraday shield, the formers were made of teflon, this material being chosen because of superior dielectric strength in small thicknesses (International Telephone and Telegraph Corporation, 1977).

Teflon does not withstand temperatures much in excess of 200°C and so a separate coil former and sample holder were made of Macor Machinable Glass-Ceramic for high temperature work. The Macor Machinable Glass-Ceramic has negligible sodium content. However, the material is very fragile and not easy to machine in small thicknesses. The diameter of the high temperature crystal holder was therefore larger than that of the low temperature crystal holder and the coil diameter had to be increased to 1.06 inches.

This meant that the number of turns had to be reduced from nineteen to sixteen to keep the inductance at about 7 μH. The length of the coil was 0.50 inches. The coil was again wound with silver wire, but the diameter was increased to 0.014 inches to obtain a higher Q-factor and to reduce the stray inductance of the leads.

The body of the probe was solidly constructed using 3/16-inch material to reduce microphonic effects. Brass was used, in preference to aluminum for example, to reduce spurious ringing signals observed by other workers (Buess and Peterson, 1978) and by us with a preliminary aluminum probe.

4.1.3 Faraday shield

A major problem in performing pulsed NMR on piezoelectric materials is the spurious signals associated with the "ringing" of the sample caused by the rf pulse. For a single crystal of $NaNO_2$ the so-called "piezoelectric ringing signals" are, at some crystal orientations, two orders of magnitude larger than the ^{23}Na FID following a typical 90° pulse (Hughes and Pandey, 1984). Three methods to reduce the problem have been described in the literature: firstly, grinding the crystal into a fine powder, secondly, immersing the crystal in a viscous liquid to damp the vibrations, and thirdly, using a shield to reduce the rf fields which excite the piezoelectric vibrations. The first method is obviously inappropriate in our case. The second method provides inadequate suppression in the case of $NaNO_2$, and so we used a shield to suppress the spurious signals.

Hughes and Pandey (1984) in our laboratory showed that the piezoelectric ringing signals are caused by a purely electric interaction between the crystal and the coil. They designed an electrostatic or Faraday shield (Pandey and Hughes, 1984) that reduced the piezoelectric ringing signals by about four orders of magnitude. The term Faraday shield means different things to different people. We mean a device that largely eliminates the electrostatic or conservative (curl $\vec{E} = 0$) part of the time-varying electric field caused by charges on the coil, without altering the induced or non-conservative (curl $\vec{E}=-\partial\vec{B}/\partial t$) component caused by the time-varying magnetic field (Townsend and Donaldson, 1928; Allen and Segre, 1961; Contaxes and Hatch, 1969; Magid, 1972). The $\vec{B}$ field is, of course, essential to perform the NMR experiment. The reason that Pandey and Hughes were able to achieve such a large suppression is because the piezoelectric ringing signals involve the square of the strength of the electric interaction between the coil and the crystal. For example, if the shield reduces the electric field at the crystal caused by rf pulse to 1% of its unshielded value, the amplitude of the piezoelectric vibration would be reduced to 1% of its previous value. However, the shield also reduces the reverse electrical coupling between the coil and the charges on the crystal to 1% of its previous value, so that the amplitude of the piezoelectric ringing signals is 0.01% of the value without the shield.

For the room temperature probe, we used the Faraday shield designed by Pandey and Hughes (1984). A disadvantage was that it was made of copper, and a small ^{63}Cu FID could be seen superposed on the ^{23}Na FID. However, because the spin-lattice relaxation time of ^{23}Cu in copper is about 3.5 ms (Redfield, 1956), much shorter than that of ^{23}Na in $NaNO_2$, it had negligible effect on our results.

For the low temperature probe, a silver shield of improved design was made using a silk-screening process by the Graphics Division in the Technical Services Department of the University of alberta. The design is shown in Fig. 4.3(a). The substrate is kapton 0.002 inches thick. The gaps and the silver strips are 0.5 mm wide. Together, they prevent large scale induced currents from flowing in the shield, currents which would otherwise reduce the rf magnetic field. The shield was glued to the inside of the coil former and the long pig-tail enabled the shield to be grounded to the body of the probe. Early versions of the shield were found to significantly reduce the Q of the coil in which they were placed. This was found to be due to the fact that the electrical resistance of the silver strips

Figure 4.3

Profile of (a) an earlier version

(b) a later version of the Faraday shield

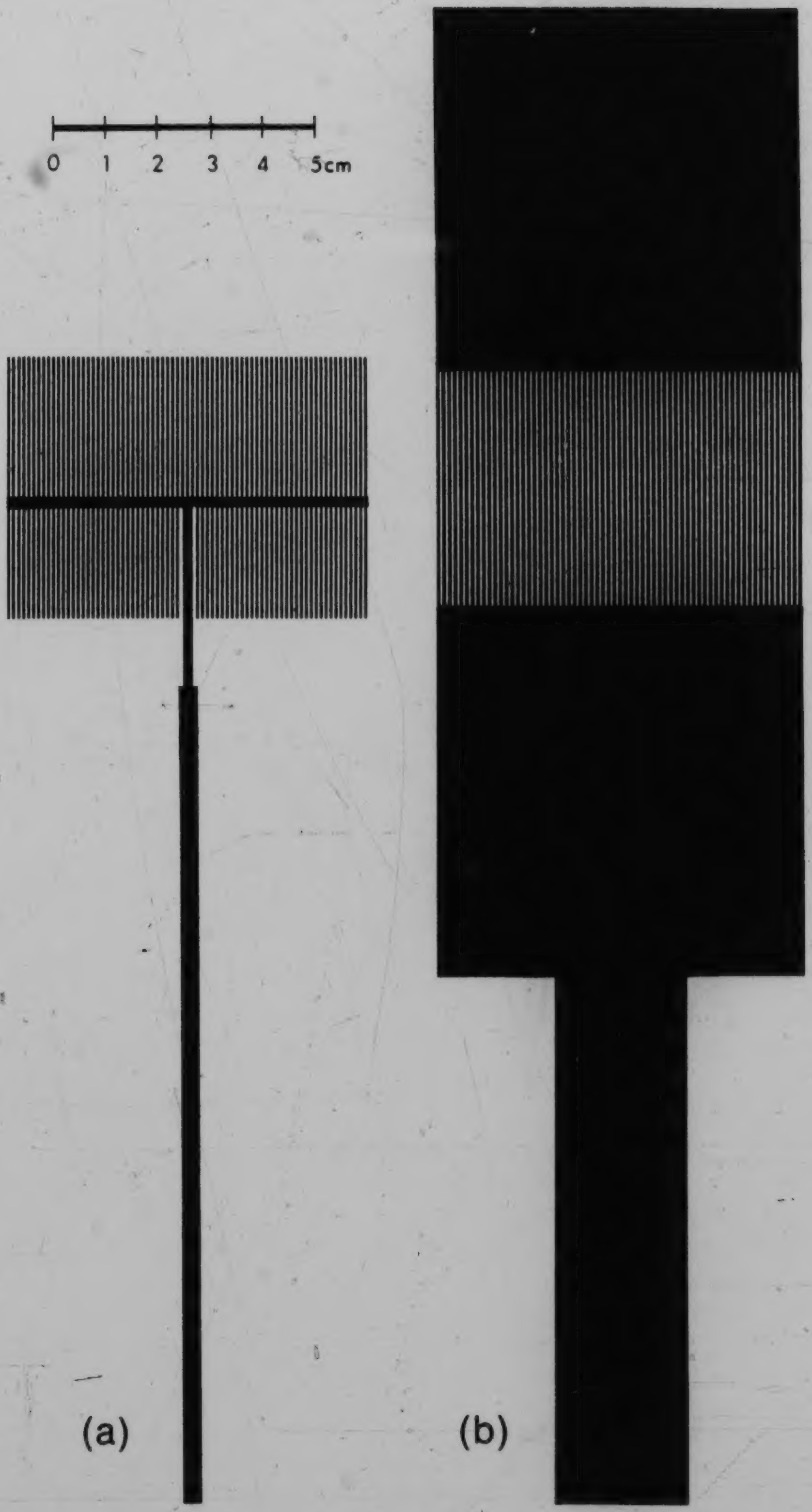
5cm
(a)
(b)

and pig-tail was too high. A thicker layer of silver ink was therefore laid down by repeated applications of ink during the silk-screening process. Also, following the advice of Advanced Coating and Chemical Co., California, the manufacturer of the silver ink (Silver Conductance Coating, Type 720 C), the shield was heat-treated for four hours in an oven at 100°C to reduce the electrical resistance of the ink. A shield with a resistance of about 10 Ω from one end of the shield to the end of the pig-tail was found to reduce the Q of the coil by only about 10% and it totally eliminated the spurious piezoelectric signals.

When making measurements at low temperatures, it was found that an important function of the shield was to reduce rf interference from the temperature controllers fed along to the temperature sensors located near the rf coil. Indeed, we found that the suppression of the rf interference was a more severe test of the efficiency of the shield than the suppression of the piezoelectric ringing signals. This is because the magnitude of the observed interference signals is directly proportional to the electrical coupling between the rf coil and the temperature sensors, whereas the amplitude of the piezoelectric ringing signals is proportional to the square of the electrical coupling between the rf coil and the piezoelectric sample. Because of the rf interference, some of the later low temperature measurements were made using a shield of the design shown in Fig.

4.3(b). The continuous parts of the shield above and below the strips were added to minimize the electrical coupling between the rf coil and the temperature sensors and heaters.

The high temperature probe used a stainless steel (non-magnetic type 304) shield of the type shown in Fig. 4.3(b). The shield was 0.009 inches thick and was strong enough to be slid as a cylinder inside the machinable glass-ceramic coil former. A disadvantage of this shield is that it reduced the Q of the rf coil to between 35 and 40. This is less than the optimum value for our experiments and we recommend that, in future, a thinner stainless steel shield be tried even though it might be more difficult to manufacture and install.

4.1.4 Sample holders and variable temperature systems

Three sample holders were constructed to fit inside the room temperature probe, the low temperature probe and the high temperature probe respectively. The design of the low temperature probe is shown in Fig. 4.4. The high temperature probe is of similar design but of slightly larger diameter as mentioned in section 4.1.3.

Each sample holder can be rotated about Axis 1, the long axis of the probe, which is arranged to be vertical. Its orientation about that axis can be read with an accuracy of about 0.1 degree on a three-inch diameter circular

Figure 4.4

Low temperature sample holder and variable temperature system

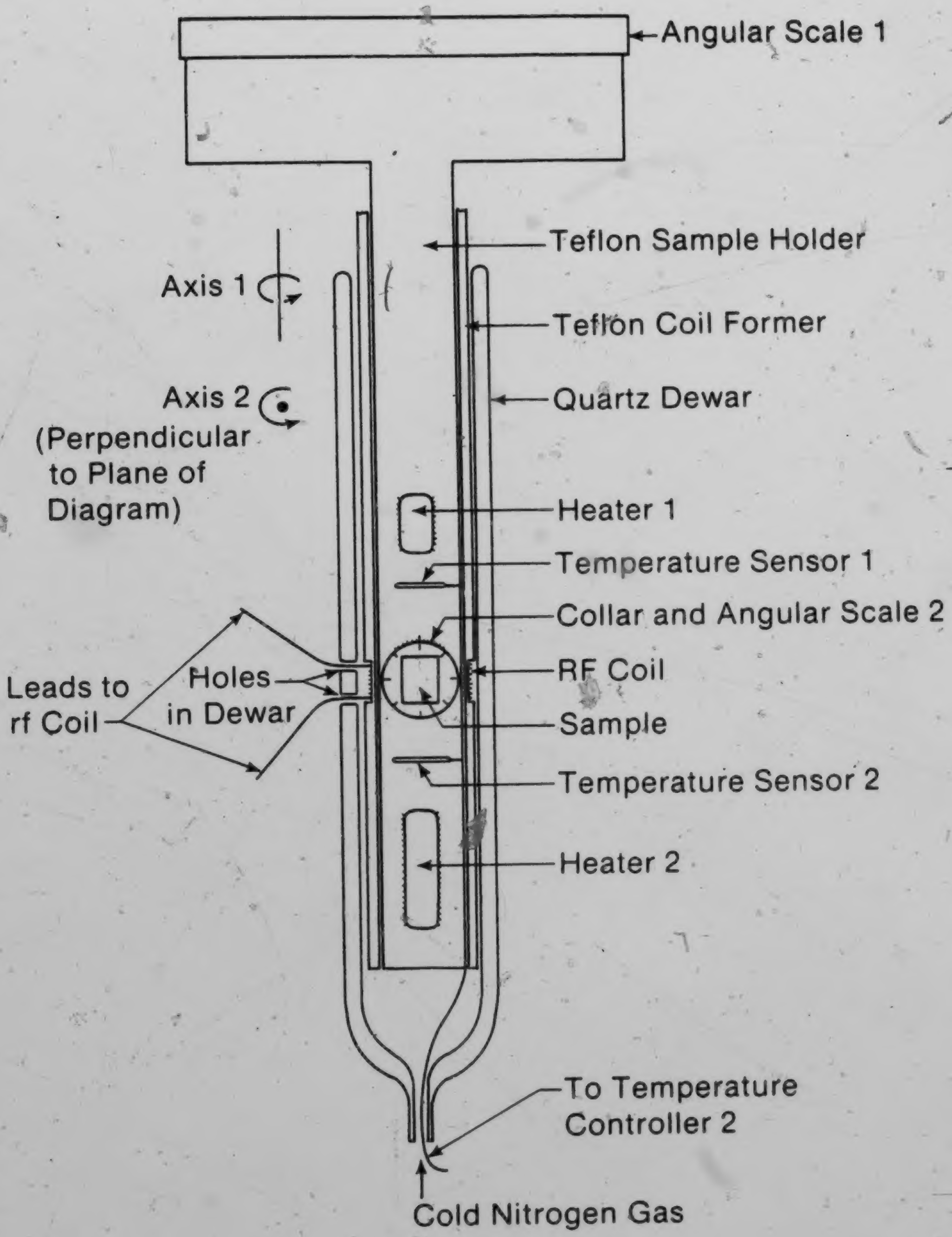
Angular Scale 1
Teflon Sample Holder
Axis 1
Teflon Coil Former
Axis 2
(Perpendicular to Plane of Diagram)
Quartz Dewar
Heater 1
Temperature Sensor 1
Collar and Angular Scale 2
Leads to rf Coil
Holes in Dewar
RF Coil
Sample
Temperature Sensor 2
Heater 2
To Temperature Controller 2
Cold Nitrogen Gas

vernier scale which we call Scale 1. As shown in Fig. 4.4, the crystal itself is held in a small collar that can be rotated about Axis 2, an axis perpendicular to the long axis of the probe. The orientation of the crystal about that axis can be read with an accuracy of about one degree from a vernier scale on the collar which we call Scale 2. The two rotations allow the crystal to be set at any desired orientation relative to the external magnetic field $\vec{H}_o$ which is perpendicular to Axis 1.

In order to minimize the temperature gradient across the sample, two heaters symmetrically situated above and below the sample were used. In the low temperature arrangement, the upper heater had a resistance of 24 Ω and the lower heater had a resistance of 32 Ω. Both heaters were made of 34-gauge manganin wire, non-inductively wound on a former made of a ceramic foam manufactured by the Cotronics Corp. in Brooklyn, N.Y. Two type PT-103 platinum resistance thermometers manufactured by Lakeshore Cryotronics were mounted above and below the sample as shown in Fig. 4.4 to measure and control the temperatures at those locations. The heaters in the high temperature system were similarly constructed but their resistances were 50 Ω in order to obtain more power from the constant current generators in the controllers. The heaters were wound non-inductively on the machinable glass ceramic part of the sample holder.

The low temperature coil former and the high temperature coil former fitted inside a quartz Dewar vessel made by the Technical Services Glass-blowing Shop. The Dewar was basically cylindrical with an inside diameter of 3.6 cm and an outside diameter of 4.5 cm, these being the largest diameters that could be accommodated in the space between the magnet pole caps. Because of the proximity of the rf coil to the Dewar vessel, it was necessary to leave a 7.5 cm gap in the silvering near the location of the rf coil. Otherwise, the Q of the coil would be greatly reduced because of rf currents flowing in the silvering. We noticed only a slight reduction ~5% in the Q of our coil caused by the Dewar. The lack of silvering allows much more radiant energy to flow through the Dewar near the rf coil. In order to reduce this heat transfer, the outside of the Dewar was enclosed in a thin layer of styrofoam.

What we think is a unique feature is the provision of two small holes about 2 mm in diameter in the side of the Dewar near the location of the rf coil as shown in Fig. 4.4. These allow the leads connecting the rf coil to the input connector and the vacuum-variable capacitor to be as short as possible. This ensures that the stray inductance of the leads is small so that the inductance of the coil itself is a maximum, as required for a good NMR signal-to-noise ratio. The holes in the side of the Dewar were sealed with a small quantity of polystyrene Q-dope.

As shown in Fig. 4.4, the Dewar narrows at the bottom to provide an access hole 6 mm in diameter. To obtain sample temperatures below room temperature, cold nitrogen gas is fed through the access hole so that it flows past the outside of the sample holder or coil former. The 6 mm diameter access hole also allows leads from the lower sensor and heater to be led from the sample holder without passing through the rf coil.

Cold nitrogen gas was obtained by boiling liquid nitrogen in a large 200 litre storage Dewar. The AC power fed from a Variac to a 50 ohm power resistor suspended in the liquid was adjusted to give a rate of flow of gas which would give a temperature about five degrees lower than the required temperature. The temperature controllers and heaters were then used to raise the temperatures at both sensors to the desired value. To obtain temperatures stable to within ±0.1°C we found it necessary to feed the Variac from a line voltage regulator. Otherwise, variations in the rate of flow of gas, caused by sudden changes in line voltage, caused temperature fluctuations that the controllers and heaters could not compensate. The sample temperature was taken to be the mean of the temperatures indicated by the two sensors.

For measurements above room temperature, no gas flow was used. Instead, the temperature controllers were used to supply power to the two heaters in such a way as to maintain both sensors at the same temperature. In the high temperature system, there were substantial temperature inhomogeneities and a copper constantan thermocouple was therefore used to measure the temperature near the sample. To minimize heat flow along the wires to the hot junction, 30 gauge constantan and 42 gauge copper were used to form the thermocouple. The hot junction was installed in a small hole drilled in the machinable glass ceramic about 15 mm from the centre of the sample. The cold junction was kept at 0°C in an iced-water bath and values of the temperature were obtained from a Type T thermocouple reference table (Powell et al., 1974).

4.1.5 Pulse generator

The pulse generator used in our system was designed and constructed by the electronic shop in the Department of Physics. It provides two rectangular pulses of variable width, the resolution being 69 ns, the period of the 14.5 MHz clock signal. The pulse separation can be set anywhere in the range 10^2 to 10^{10} clock period ($6.9\ \mu s$ to $6.9\times10^2 s$) with a resolution of 10^2 periods, and the pulse sequence interval, i.e. the time between consecutive pairs of pulses, can be set anywhere in the range 10^5 to 10^{11} clock period (6.9 ms to $6.9\times10^3 s$). The pulse durations and the intervals between pulses are selected by a set of decade thumbwheel switches.

4.1.6 Magnet

The magnetic field was produced by a Varian V-3601 12-inch electromagnet, mounted horizontally and equipped with tapered pole-caps giving a magnet gap of 2.3 inches and a maximum magnetic field strength of 1.35 T. A field stability of better than 5 parts in 10^6 is achieved by means of a Varian Fieldial Regulator Mark II V-FR 2500.

4.2 Sodium nitrite

Two single crystals of $NaNO_2$, referred to as A and B, were used in this work. Crystal A, provided by Dr. Y. Takagi from Nagoya University, Japan, was prepared using reagent-grade material with the following listed impurities: Cl < 0.005%; SO_4 < 0.005%; Heavy metals (as Pb) < 0.001%; Iron (Fe) < 0.001%; Ca < 0.01%; K < 0.01%. This crystal is approximately cylindrical in form, 15 mm in diameter and 11 mm in length. The ferroelectric axis ($\underset{\sim}{b}$ axis) is at right angles to the cylinder axis. Crystal B, provided by Dr. S. Sawada from the Tokyo Institute of Technology, Japan, was cleaved parallel to the (101), (10$\bar{1}$) and (010) faces. The height of the crystal is 1.15 cm in the $\underset{\sim}{b}$ direction. The (010) faces are in the shape of a rhombus 0.83 cm long in the $\underset{\sim}{a}$ direction and 1.3 cm long in the $\underset{\sim}{c}$ direction.

4.3 Installation of the $NaNO_2$ crystals in the sample holder

Crystal A is not perfectly cylindrical in shape and so it was necessary to orient it in its collar by trial and error. The desired orientation is with the symmetry (2-fold) axis parallel to Axis 2. This is so that rotation about Axis 1 changes θ but not ϕ, whereas rotation about Axis 2 changes ϕ but not θ. This greatly facilitates interpretation of the experimental data.

The method of aligning the crystal can be explained in the following way. Fig. 4.5(a) shows a horizontal section through Axis 2. For clarity, the crystal is shown as lying behind angular scale 2 whereas, in fact, it lies partly in front of it. Fig. 4.5(b) shows a front view of Angular Scale 2. The point O lies at the centre of the angular scale. An imaginary line is now drawn through any point C within the crystal parallel to the symmetry axis of the crystal. That line intercepts the front of the scale at the point P say (see Fig. 4.5(b)). The projection of the line CP on the horizontal plane shown in Fig. 4.5(a), intercepts the front of the scale at the point P' shown in Figs. 4.5(a) and 4.5(b). If the angle $O\hat{C}P$ between the symmetry axis and the rotation axis, which we call γ, is small, then it follows that $\beta=\gamma\cos\alpha$ where α is $P\hat{O}P'$ (see Fig. 4.5(b)). It can be seen from Eq. (3.1) that when θ is small, less than say 5°, the frequency of the high frequency satellite, ν_{hfs}, is nearly independent of ϕ and has a

Fig. 4.5

Schematic diagram of sample holder showing

(a) a horizontal section through Axis 2.

(b) a front view of Angular Scale 2.

(a) Horizontal Section Through Axis 2

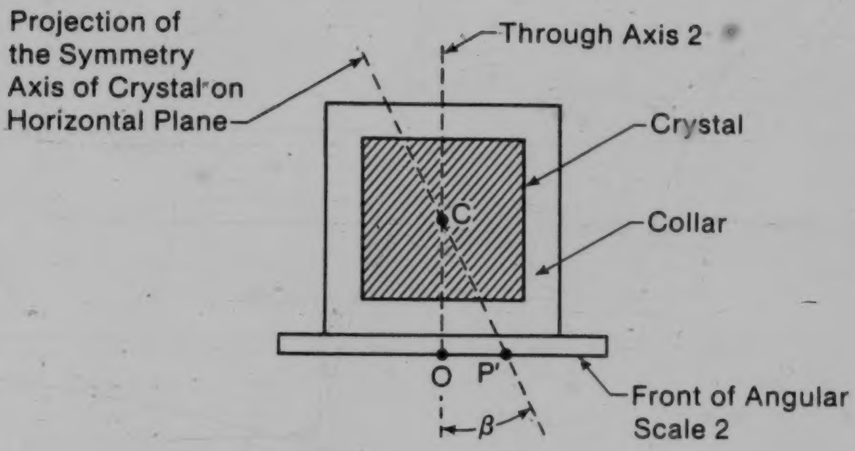
Projection of the Symmetry Axis of Crystal on Horizontal Plane
Through Axis 2
Crystal
C
Collar
O
P'
β
Front of Angular Scale 2

(b) Front View

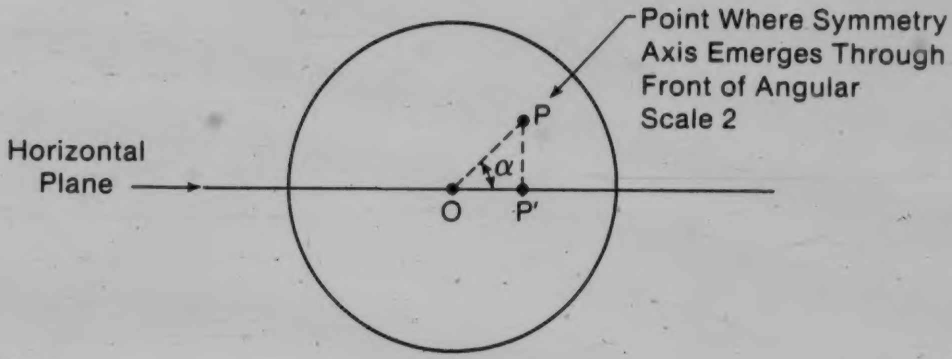
Point Where Symmetry Axis Emerges Through Front of Angular Scale 2
P
α
Horizontal Plane
O
P'

maximum value when θ (the angle between the crystal symmetry axis and the external magnetic field $\vec{H}_o$) is a minimum. If follows that when $\vec{H}_o$ is rotated relative to the crystal (in the horizontal plane), ν_{hfs} will be a maximum when $\vec{H}_o$ is along CP', i.e. when the angle θ between the magnetic field and the symmetry axis CP is a minimum. When this is achieved, the angle β (see Fig. 4.5(a)) has a value β_1 say. Even though β_1 cannot be read directly, the reading θ_1', say, on Angular Scale 1 is equal to β_1 plus a constant δ, say, so that we can write

$$\theta_1' = \beta_1 + \delta = \gamma\cos\alpha + \delta \ . \qquad (4.1)$$

The crystal is now rotated through 120° about Axis 2 so that α in Eq. (4.1) now becomes $\alpha+2\pi/3$. The above procedure is repeated, and the reading θ_2' on Angular Scale 1 is read when $\vec{H}_o$ is at an orientation relative to the crystal such that ν_{hfs} is a maximum. The equation corresponding to Eq. (4.1) now reads

$$\theta_2' = \gamma\cos(\alpha+2\pi/3) + \delta \ . \qquad (4.2)$$

Finally, the crystal is rotated about Axis 2 through a further 120° and the angle θ_3' at which ν_{hfs} is a maximum is again read and

$$\theta_3' = \gamma\cos(\alpha+4\pi/3) + \delta \ . \qquad (4.3)$$

By solving Eqs. (4.1), (4.2) and (4.3), one determines γ and α so that the orientation in space of the symmetry axis relative to rotation Axis 2 is known. A trial adjustment of the crystal in its collar is now made and the above procedure is repeated until the angle γ between the symmetry axis and rotation Axis 2 is sufficiently small. After some practice, we were able to orient the crystal in its collar so that γ was less than 1.5°. We note that Nyquist's sampling theorem (Carlson, 1968) implies that it is necessary to measure θ' at a minimum of three different orientations of the crystal.

Crystal B was cleaved when received, and so the sides of the crystal were parallel to the symmetry axis. It was therefore easy to mount the crystal in the collar so that the symmetry axis was parallel to Axis 2.

4.4 Experimental procedure

4.4.1 Measurement of FID amplitudes

In order to accurately measure relative FID amplitudes, it is essential that the detection system is highly linear. Any receiver operated as an amplitude or diode detector becomes nonlinear when the signals are small. We therefore used phase-sensitive detection to record our FID's. Also, we adjusted the receiver gain so as to operate well below the upper limit of linearity quoted by the manufacturer. The bandwidth of the receiver was kept at 500 kHz for most of our measurements to ensure that there was no distortion of our FID's. To obtain improved accuracy, considerable signal averaging was employed. For studying the orientation dependence of the relaxation rate, the number of sweeps ranged from 32 at low temperature to 256 at high temperature. A data acquisition rate of 1 μs per point was used and the FID was recorded using the full 4096 channels of the Signal Averager.

During our preliminary work, we discovered that the digitizer of the Signal Averager became quite nonlinear when a substantial DC offset was introduced by means of the DC offset control on the front panel of the instrument. When we brought this to the attention of the manufacturer, Nicolet, they agreed that there was a design fault and they said they would inform other owners of their instrument of the problem. For all the work reported in this thesis, we set the instrument DC offset control to zero to avoid the above problem, even though it meant not using one of the twelve bits in the digitizer.

Instead of reading the amplitude of the FID from only one channel, we integrated the FID from t_1 to t_2 to obtain the area under the curve as illustrated in Fig. 4.6. This was done using the instrument's digital integration capability. This procedure makes much better use of the data collected and gives a considerably better signal-to-noise ratio. However, when using phase-sensitive detection and integration, it is important for the field/frequency ratio to be maintained on resonance, since the FID is multiplied by $\cos(\delta\omega t)$ where $\delta\omega$ is the resonance offset and t is the elapsed time after the pulse. The effect of a

Fig. 4.6

Schematic diagram of the FID. The signal is observed after a dead time t_1. The shaded area shows the signal integrated between t_1 and t_2. The dashed curve shows the effect of a small drift of the magnetic field or frequency.

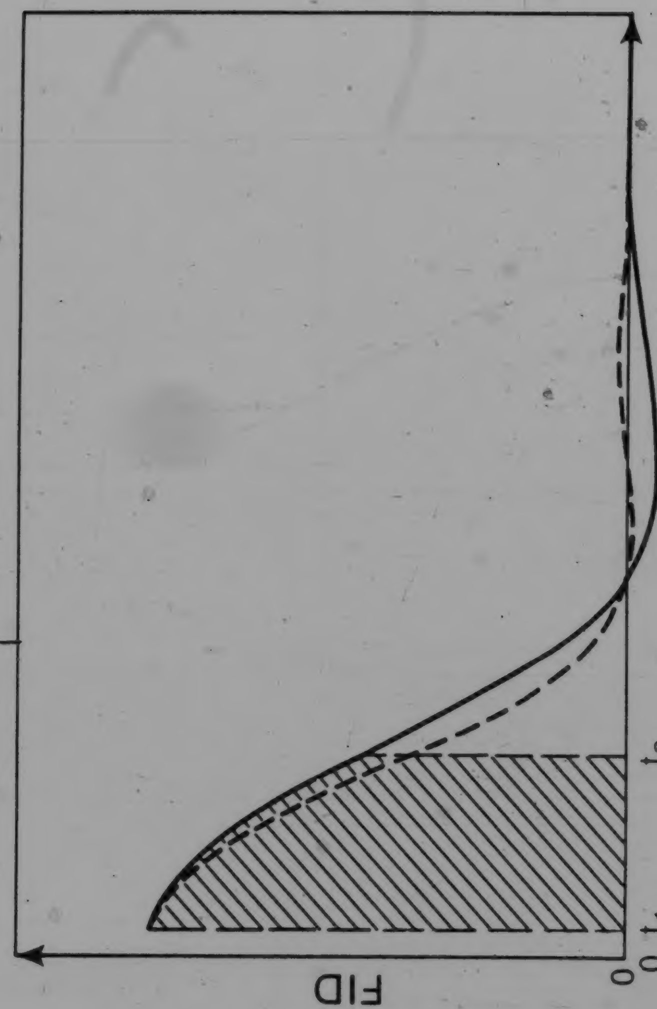
FID
0
0
t_1
t_2
t

resonance offset is illustrated by the dashed curve in Fig. 4.6. For small t, the error introduced by a resonance offset increases as t^2 and, for our field stability ~ 5 parts in 10^6, it meant that we could only integrate over a range t_2-t_1 of about 100 μs. However, since our FID's decay in a time of that order, not much signal amplitude is lost by limiting the integration to such a value. To ensure that only the FID was integrated, the beginning of the signal averager sweep was delayed by typically 20 to 30 μs until the receiver had recovered completely from the pulse. Another advantage of integrating the FID's is that it allowed us to remove the small variable DC offset that is always present. This was done by digitally adding or subtracting a constant from the final signal until the baseline of the integrated signal (after the FID has decayed away) had zero slope.

4.4.2 Choice of experimental method to study the orientation dependence of the quadrupole relaxation

As can be seen from section 2.3.1, several different DNMR experiments can be performed to study quadrupole relaxation in spin systems with I=3/2. These are:

(i) Perturb the centre line and observe the recovery of the centre line which should be of the form $A(e^{-2W_1t}+e^{-2W_2t})+B$ where A is a constant which depends on the perturbation and B is a constant which does not (cf. Eq. (2.65)).

(ii) Perturb the centre line and observe the recovery of either satellite which should be of the form $Ae^{-2W_1t}+B$ (cf. Eq. (2.66)).

(iii) Perturb one of the satellites and observe the recovery of the centre line which should be of the form $Ae^{-2W_1t}+B$ (cf. Eq. (2.67)).

(iv) Perturb one of the satellites and observe its recovery which should be of the form $A(e^{-2W_1t}+e^{2(W_1+W_2)t})+B$ (cf. Eq. (2.68)).

(v) Perturb one of the satellites and observe the recovery of the other satellite which should be of the form $A(e^{-2W_1t}-e^{2(W_1+W_2)t})+B$ (cf. Eq. (2.69)).

Experiments (i), (iv) and (v) have the advantage that they would allow the simultaneous determination of W_1 and W_2. However, it is difficult to obtain accurate values of the two relaxation rates when the recovery is the sum of two exponentials, especially when they are of the same order of magnitude. Moreover, as discussed in section 2.2.3, the same M-tensor governs both W_1 and W_2 in the short correlation time limit. Previous work by BBR (1970) has indicated that the correlation time does seem to be short for the spin-lattice relaxation of ^{23}Na in NaNO$_2$ so that there is no need to determine both W_1 and W_2, at least over a wide temperature range.

Experiments (ii) and (iii) are therefore to be preferred, since it should be easy to accurately determine W_1

from the exponential recovery. Experiment (iii) has the advantage that the centre line has a larger amplitude than the satellite by the ratio $2:\sqrt{3}$ (Schmidt, 1972; Fukushima and Roeder, 1981). Also, the FID's of the ^{23}Na satellites in $NaNO_2$ decay much faster than the FID of the centre line at certain crystal orientations, because of inhomogeneous first-order quadrupole broadening (Betsuyaku, 1969; Bonera et al., 1970). (The centre line is not affected by first-order quadrupole interactions, as can be seen from Eq. (2.34).) We therefore performed experiments (ii) and (iii) in a preliminary study, in order to compare their feasibility and to check that they gave the same values of W_1.

There are two obvious ways in which these experiments can be done. They are the double resonance equivalents of the saturation-recovery method and the inversion-recovery method. These methods differ in that the first resonance is completely saturated in the saturation-recovery method and is inverted by a 180° pulse in the inversion-recovery method. The inversion-recovery method has the advantage that the change in the FID amplitude is twice as large as in the saturation-recovery method (see section 2.3.1). However, it is not possible to fully "invert" a broad resonance with a 180° pulse, because the pulse length τ_p must satisfy the condition $\delta\omega\tau_p << 1$ where $\delta\omega$ is the resonance linewidth. It is particularly difficult to satisfy that condition in our double resonance experiments because our pulses must also be selective, i.e. they must satisfy the condition $\omega_Q \tau_p >> 1$ where ω_Q is the frequency separation between adjacent resonances. Saturation can be achieved in the saturation-recovery method either by applying a single 90° pulse, or, for broad resonances, by applying a comb of 90° pulses separated by an interval $\gtrsim T_2$ (Avogadro et al., 1971; Fukushima and Roeder, 1981), or by the use of more complicated sequences of phase-shifted pulses (Levitt and Freeman, 1979; Freeman et al., 1980).

Since the satellites of ^{23}Na in $NaNO_2$ are quite broad at some crystal orientations, we decided to use a comb of 90° pulses (without phase shifts) to achieve saturation. Experiment (ii) was therefore performed by applying a comb of 90° pulses to the centre line and monitoring the recovery of one of the satellites by measuring the amplitude of its FID at various values of the waiting period between the end of the saturating sequence of pulses and the beginning of the subsequent 90° pulse. We call this FID amplitude $M_z(\tau)$ because it is a measure of the z component of the magnetization immediately before the pulse. We also accurately measured $M_z(\infty)$, the amplitude of the FID of the satellite in thermal equilibrium, i.e. when τ is very long. The quantity $M_z(\tau)-M_z(\infty)$ was plotted semilogarithmically against τ, and the relaxation rate $2W_1$ found from the slope of a straight line fitted to the data by means of a weighted least squares fit. The weighting factors were taken to be proportional to the individual values of $M_z(\tau)-M_z(\infty)$. Experiment (iii) was performed in the same way as experiment (ii), except that the comb of 90° pulses was applied to the satellites and the single 90° pulse was applied to the centre line.

Both these experiments were repeated at four different crystal orientations and the values of W_1 obtained are listed in Table 1. The errors are 68% confidence standard errors obtained from the scatter of the data in the least squares fit. It can be seen from Table 1 that the two values of W_1 agree within the combined experimental errors only at one crystal orientation. The ratio of W_2/W_1 at the various orientations were calculated using the ratio of the M-tensor components found by Hughes and Spencer (1982), and they are listed in Table 1. It can be seen that the sign of the discrepancy is different for the cases where $W_2/W_1 > 1$ and where $W_2/W_1 < 1$. We believe that the discrepancy was caused by the fact that our saturating pulses were not completely selective. The saturating comb consisted of twenty-two rectangular 90° pulses each 80 μs long. The interval between them was 240 μs. Rectangular pulses of frequency ν_o and duration τ_p have a frequency spectrum of the form $\sin\pi(\nu-\nu_o)\tau/\pi(\nu-\nu_o)\tau$ (e.g. Carlson, 1968). Most of the power is confined to the frequency range ν_o-1/τ to ν_o+1/τ, which for our 80 μs pulses is 12.5 kHz on either

Table 1

W_1 of ^{23}Na in $NaNO_2$ at various crystal orientations, obtained from experiments (ii) and (iii)

Orientation	Experiment performed	W_1 ($\overline{s}^{-1}$)	$(W_2/W_1)_{calc}$
$\theta=0°$	(ii)	0.596±0.009	1.93
$\phi=90°$	(iii)	0.561±0.005	
$\theta=29°$	(ii)	1.374±0.017	0.76
$\phi=90°$	(iii)	1.422±0.020	
$\theta=39°$	(ii)	1.609±0.026	0.71
$\phi=90°$	(iii)	1.635±0.014	
$\theta=69°$	(ii)	1.035±0.009	1.96
$\phi=90°$	(iii)	1.016±0.009	

side of the carrier frequency. The separation between resonances is much larger than this, ranging from 195 kHz at $\theta = 69°$ and $\phi = 90°$ to 550 kHz at $\theta = 0°$. The excitation of adjacent resonance by our saturating comb of pulses will therefore be very small but will undoubtedly occur to some extent.

Suppose that the comb of saturating pulses in experiment (ii) excited the satellites in addition to the centre line. The excitation of the satellites will be weak if the separation of the centre line and satellites is relatively large and the effect will be to weakly saturate each resonance. Since the centre line and hence the rf frequency of the pulse is, in first order, midway between the two satellites, both satellites should be saturated equally. Thus, the population differences N'_{+1} and N'_{-1}, defined in section 2.3.1, should be equal. It then follows that C in Eqs. (2.63) and (2.64) should be zero, so that the recovery of the satellites is still exponential with a relaxation rate $2W_1$. In other words, slight excitation of the satellites in experiment (ii) should have no effect, in first order, on the measured value of W_1.

Consider now the situation in experiment (iii) where the saturating comb is applied to one of the satellites. If the saturating comb partially saturates the centre line so that n spins are raised from the state $m = 1/2$ to the state $m = -1/2$, but does not excite the other satellite (because it is twice as far away in the frequency domain), it can be shown from Eqs. (2.62), (2.63) and (2.64) that the recovery of the population difference associated with the centre line should be given by

$$N_o' = \{(n_o-n)/2\}(e^{-2W_1t} - ne^{-2W_2t}) . \qquad (4.5)$$

In this case, the centre line recovery is no longer exponential. There is a small contribution from the transition probability W_2. If W_2 is greater than W_1, the relaxation rate deduced by fitting the data to an exponential will be smaller than $2W_1$. On the other hand, if W_2 is smaller than W_1, the relaxation rate deduced by fitting the data to an exponential will be larger than $2W_1$. These predictions are in qualitative agreement with the results shown in Table 1. From our preliminary investigation, we therefore conclude that W_1 is best measured by experiment (ii).

Experiment (ii) can be carried out by measuring the recovery of either satellite. When studying the orientation dependence of the spin-lattice relaxation at room temperature, we monitored the recovery of each satellite in turn. As expected, there was no significant difference in the W_1 values obtained, and, in later measurements made at other temperatures, we measured the recovery of only the high frequency satellite (i.e. the satellite whose frequency is higher than that of the centre line). In our room temperature work, we used the saturation-recovery method, the same one as we used in our preliminary investigation. However, for the later work at other temperatures, we decided to try the inversion-recovery method. We found that the centre line was sufficiently narrow that we could achieve a large measure of resonance inversion with a nominal 180°pulse, while at the same time keeping the pulse selective. (It is clear from Eqs. (2.63) and (2.64) that it is not necessary to achieve complete inversion of the resonance. Even if inversion is not complete, the recovery of the satellites is still exponential with a rate $2W_1$.)

The determination of relaxation rates from the slopes of semilog plots can be criticized on two counts. Firstly, it assumes an exact knowledge of $M_z(\infty)$ which is, of course, not available. Secondly, if the signal-to-noise ratio is poor, there is a systematic tendency for the $\ln(M_z(\tau)-M_z(\infty))$ values to be too low when τ is large, because of the fact that $\ln(M_z(\tau)-M_z(\infty))$ is not a linear function of $\{M_z(\tau)-M_z(\infty)\}$. That would cause values of relaxation rate deduced from the slope of the graph to be slightly too large. In order to avoid these problems in our studies of the orientation dependence of quadrupole relaxation, we fitted our $M_z(\tau)$ values directly to an expression of the form

$$M_z(\tau) = Ae^{-2W_1\tau} + B \qquad (4.6)$$

by means of a nonlinear least squares fit. When using that method, there is no need to obtain an accurate value of

$M_z(\infty)$, though measurements should of course be made with large τ so that the baseline B is well determined.

4.4.3 Choice of experimental parameters to study the orientation dependence of the quadrupole relaxation

(a) Crystal orientation

As can be seen from Eq. (3.4), the orientation dependence of W_1 is governed by six independent M-tensor components. To determine them all, it is necessary to measure W_1 at at least six suitably chosen orientations of the crystal relative to $\vec{H}_0$. In order to confirm the validity of Eq. (3.4), measurements at many more orientations should be made. We therefore measured the relaxation rate of the high frequency satellite by means of experiment (ii) at between thirteen and sixteen different orientations at the various temperatures selected. It can be seen from from Eq. (3.4) that measurements at three different values of ϕ are needed in order to determine all the M-tensor components. We therefore measured the relaxation rate for various values of θ, (including the symmetrical orientations $\theta=0°$ and $90°$) for $\phi=0°$, $45°$ and $90°$. To ensure that our pulses were sufficiently selective, we avoided crystal orientations, typically those where θ lay between 45° and 70°, where the separation of adjacent resonances was less than about 200 kHz.

(b) Time interval between pulse sequences

In signal averaging, it is necessary to select a value for τ_{seq}, the time interval between pulse sequences. In each case, we chose τ_{seq} so that $e^{-2W_1\tau_{seq}}$ and $e^{-2W_2\tau_{seq}}$ were $\lesssim 10^{-4}$. The spin system was therefore essentially in thermal equilibrium at the beginning of each pulse sequence.

(c) Choice of time interval between pulses

Measurements must be made at at least three different values of τ in order to determine the relaxation rate (see Eq. (4.6)). However, in order to see how well the data fitted an exponential, we used several τ values usually between eight and twelve, roughly equally spaced over a range so that $M_z(\tau)-M_z(\infty)$ varied by about two orders of magnitude. Such a range is comparable to the optimum range of τ values of 5.2 T_1 found theoretically by McLachlan (1977).

(d) Choice of the amplitudes of the rf pulses

The amplitudes of the rf pulses should satisfy certain criteria. In particular, the amplitude of the second rf pulse should satisfy the conditions $\gamma H_1\tau_p = \pi/2$ (cf. Eq. (2.11)), $\omega_Q\tau_p >> 1$ and, ideally, $\delta\omega\tau_p << 1$, where ω_Q is the frequency separation between the centre line and satellites and $\delta\omega$ is the linewidth of the satellites. Since $(\delta\omega/2\pi) \lesssim 3\times10^3$ Hz and $(\omega_Q/2\pi) > 2\times10^5$ Hz, we chose the amplitude of the linearly polarized magnetic field $2H_1$ to be 14 G so as to give a τ_p of about 30 μs. This satisfies the more important condition $\omega_Q\tau_p >> 1$ quite well, but hardly satisfies the condition $\delta\omega\tau_p << 1$. The loss of amplitude of the FID caused by the failure to satisfy the condition $\delta\omega\tau_p << 1$ was not large, however. An rf magnetic field amplitude of 14 G was obtained when the output from the rf gated amplifier was approximately 130 V peak-to-peak, corresponding to a power output of 42 W.

The amplitude of the first pulse was adjusted by setting the output of the RF Generator 1. It was set to the minimum level that would allow a large measure of resonance inversion by the "180° pulse". An estimate of the inversion achieved was obtained from the observed enhancement of the satellite when τ was small. Perfect inversion of the centre line would give an enhancement of 2 as can be seen from Eq. (2.66). In practice, we usually obtained an enhancement in the range 1.5 to 1.9, depending upon the width of the centre line, which, of course, varies with the orientation of the external magnetic field relative to the crystal (Betsuyaku, 1969).

4.4.4 Setting-up procedure

Several experimental parameters had to be optimized to obtain the best accuracy in the determination of the relaxation rates. For example, though it is not essential for the tip angle of the second pulse to be exactly 90°, it should be adjusted to give a maximum FID amplitude for two reasons. Firstly, the bigger the signal, the better the signal-to-noise ratio. Secondly, if the signal is a maximum, then there will be, in first order, no change in signal amplitude due to small changes in the pulse amplitude or in the pulse duration due to jitter. Since many of the experimental parameters depend upon the temperature of the probe etc., they were optimized prior to each relaxation rate measurement. The method of optimizing each experimental parameter is described briefly in the order in which they were carried out in our setting-up procedure.

(a) The probe was tuned so that its impedance was 50 Ω resistive at 14.5 MHz by means of a Hewlett-Packard 4815A Vector Impedance Meter.

(b) The magnetic field was adjusted to give a resonance frequency close to 14.5 MHz for the satellite being observed. Fine adjustment of the resonance condition was made by varying the frequency of the RF Generator 2 until a null output was obtained on the orthogonal mode phase-sensitive detector 2.

(c) The variable-phase unit was adjusted to give a maximum FID amplitude for the satellite.

(d) The length of the second rf pulse was adjusted to give a maximum FID amplitude for the satellite.

(e) A rough estimate of the resonance frequency of the centre line was obtained from the orientation of the crystal and published values of the quadrupole coupling constant and asymmetry parameter (Weiss and Biedenkapp, 1962). The precise frequency was found by monitoring the amplitude of the FID of the satellite while varying the frequency of RF Generator 1. The frequency was set at the value that gave the largest FID amplitude, i.e. the largest enhancement of the satellite. With practice, it was possible to make that adjustment to within ±50 Hz. This adjustment was important, since small fluctuations in the magnetic field would then have least effect on the measured FID amplitude.

(f) The length of the first rf pulse was set at such a value (≈ 100 μs) so as to satisfy the conditions $\omega_Q \tau_p \gg 1$ and, as far as possible, $\delta\omega\tau_p \ll 1$. The amplitude of the rf pulse was then adjusted by varying the output of RF Generator 1 until the amplitude of the FID was a maximum.

CHAPTER 5

RESULTS AND ANALYSIS

5.1 Temperature dependence of the spin-lattice relaxation of ^{23}Na in $NaNO_2$

The relaxation rate $2W_{hfs}$ of the high frequency satellite after excitation of the centre line, was measured as a function of temperature over the range 130 K to 462 K. The low temperature data are listed in Table 2 and plotted in Fig. 5.1. Data taken above room temperature are shown in Table 3 and Fig. 5.2. The crystal orientation corresponded to $\theta = 0°$ for the measurements above room temperature. The measurements below room temperature were initially believed to be at $\theta = 0°$. However, it was later found that they were taken at $\theta = 4°$, $\phi = 0°$, because the crystal was accidentally tilted slightly in its collar. The difference in the relaxation rate caused by the misorientation is not large because the relaxation rate does not vary rapidly with θ near $\theta = 0°$, on account of crystal symmetry.

The error limits in Tables 2 and 3, and in all further tables and figures, are 68% confidence standard errors obtained from the scatter of the data about the fitted exponential form. As can be seen from Tables 2 and 3, the error limits are generally between 1 and 2%. Since

Table 2

Half of the relaxation rate of the high frequency satellite, W_{hfs}, measured at different temperatures at $\theta=4°$, $\phi=0°$.

T(K) ± 1 K	$W_{hfs}(s^{-1})$
130.0	0.061±0.001
140.1	0.047±0.001
150.0	0.038±0.001
160.0	0.036±0.001
170.2	0.045±0.001
180.0	0.080±0.002
190.0	0.151±0.002
200.2	0.255±0.004
210.3	0.331±0.006
220.3	0.369±0.006
224.9	0.375±0.003
229.8	0.383±0.003
239.8	0.425±0.004
250.1	0.461±0.006
260.0	0.487±0.006
270.0	0.508±0.006
280.8	0.538±0.011
290.0	0.571±0.005
300.0	0.601±0.006

Figure 5.1

Half the relaxation rate of the high frequency satellite, W_{hfs}, of ^{23}Na in a single crystal of $NaNO_2$ at $\theta=4°$. $\phi=0°$ plotted as a function of temperature.

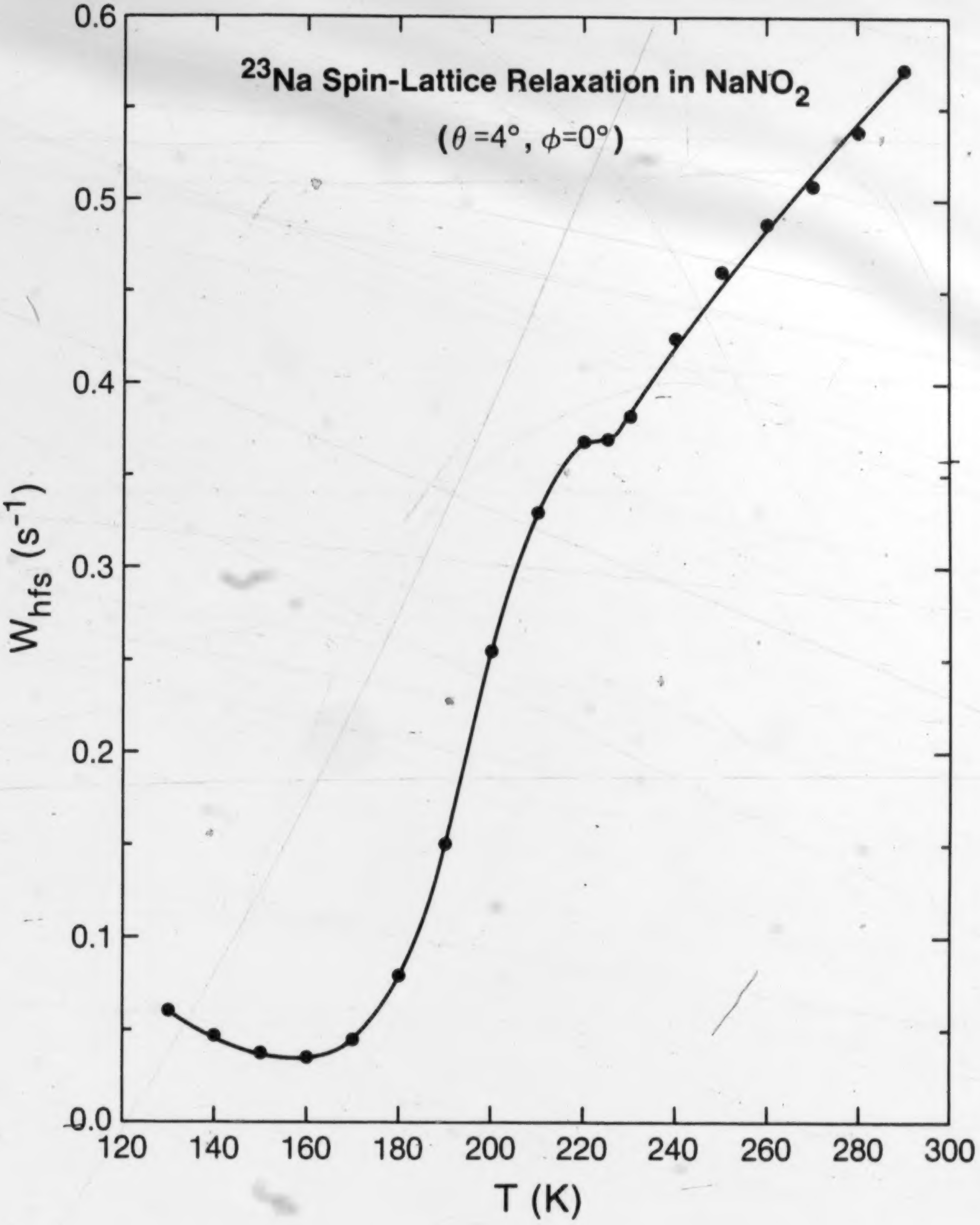
23Na Spin-Lattice Relaxation in NaNO2
(θ =4°, φ=0°)
W_hfs (s^-1)
0.0
0.1
0.2
0.3
0.4
0.5
0.6
T (K)
120
140
160
180
200
220
240
260
280
300

Table 3

Half of the relaxation rate of the high frequency satellite, W_{hfs}, ($\approx W_1$) measured at different temperatures at $\theta=0°$.

T(K) ± 1 K	$W_{hfs}(\approx W_1)(s^{-1})$
299.0	0.617±0.005
306.4	0.627±0.010
313.8	0.666±0.008
321.2	0.682±0.004
328.6	0.731±0.009
336.0	0.751±0.012
343.4	0.788±0.011
350.8	0.850±0.007
358.2	0.916±0.015
365.6	0.968±0.006
373.0	1.093±0.013
380.4	1.170±0.025
387.8	1.280±0.015
395.2	1.329±0.009
402.6	1.516±0.014
410.0	1.706±0.026
417.4	1.924±0.017
424.8	2.265±0.029
432.2	3.185±0.052
435.9	3.759±0.137
439.6	6.302±0.094
443.3	5.201±0.089
447.0	4.537±0.026
454.4	3.722±0.039
461.8	3.252±0.053

Figure 5.2

Half the relaxation rate of the high frequency satellite, W_{hfs} ($\approx W_1$), of ^{23}Na in a single crystal of $NaNO_2$ at $\theta=0°$ plotted as a function of temperature.

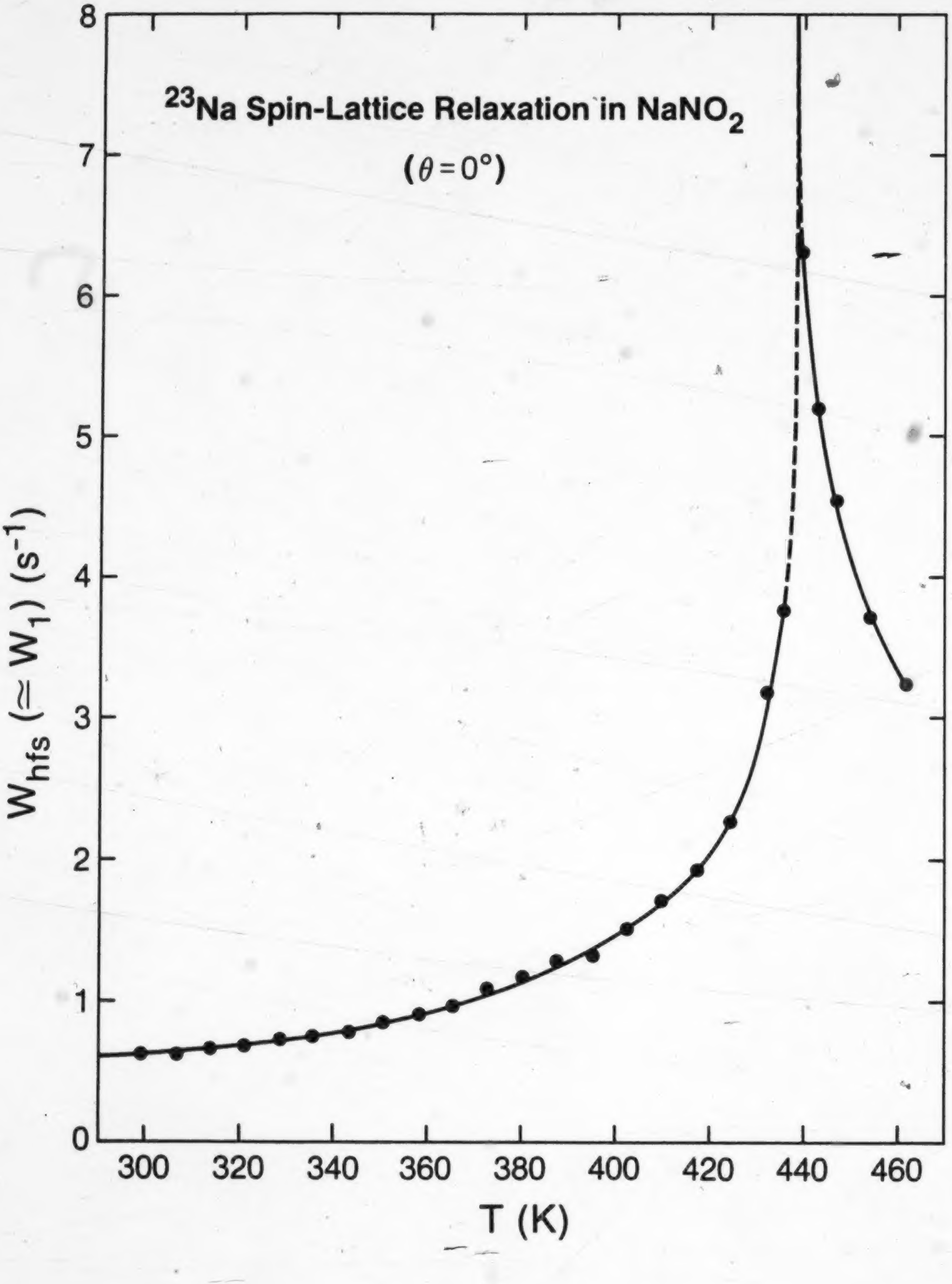
^{23}Na Spin-Lattice Relaxation in $NaNO_2$
($\theta = 0°$)
W_{hfs} ($\simeq W_1$) (s^{-1})
0
1
2
3
4
5
6
7
8
300
320
340
360
380
400
420
440
460
T (K)

random errors associated with noise are responsible for much of the scatter, it is clear that the relaxation behaviour is well fitted by a single exponential over the entire temperature range.

The temperature stability, as indicated by the platinum resistance thermometers and by the thermocouple, was about ±0.1 K at the highest temperature and about ±0.2 K at the lowest temperature. The temperatures shown in Fig. 5.1 are the means of the two temperatures indicated by the platinum resistance thermometer. Guided by the work of BBR (1970), and the behaviour of the specific heat (Sakiyama et al, 1965; Hatta and Ikushima, 1973) and the thermal expansion (Ema et al, 1973; Gesi, 1969), the high temperature data were extrapolated to the critical point. It was found to occur at a temperature of 447 K as measured by our copper-constantan thermocouple. It is believed that the critical point occurs at the Neel temperature T_N near 438 K (Avogadro et al, 1975; Ema et al, 1973). We think that the discrepancy is caused by a combination of two factors, the conduction of heat along the thermocouple wires and an inhomogeneous temperature near the crystal. We used the thinnest thermocouple wires readily available. However, since these wires pass close to the lower heater, a significant amount of heat may have been conducted to the junction, especially along the 0.003 inch diameter copper wire. The actual temperature of the crystal may also have been somewhat lower than the temperature near the thermocouple junction because the junction is closer than the crystal to the lower heater. The existence of a substantial temperature inhomogeneity is confirmed by the fact that the platinum resistance sensors situated roughly midway between the crystal and the heaters, indicated a temperature of 488 K near the critical point. We have therefore corrected the temperature as measured by the thermocouple by taking the temperature at the critical point to be 438 K and assuming that the discrepancy between the temperature of the crystal and the thermocouple junction is proportional to the difference between the indicated thermocouple temperature and room temperature. The validity of the second assumption is supported by the fact that the difference between the platinum resistance thermometer readings and the thermocouple readings was found to be proportional to the difference between the indicated platinum resistance thermometer temperature and room temperature.

Two unexpected features can be seen in Fig. 5.1. One is an abrupt change of slope near 220 K. We believe that this is real and should be investigated further. The second unexpected feature is the increase in W_{hfs} below 160 K. As will be seen later, this is caused by magnetic relaxation and W_{hfs} in Fig. 5.1 depends upon W_1, W_2 and W_3. When the magnetic relaxation is small compared to the quadrupole relaxation, W_{hfs} is approximately equal to W_1+2W_3, the sum of the quadrupole transition probability W_1 and half the magnetic transition probability $4W_3$ (see section 2.3.2). Since the magnetic contribution is negligible above room temperature, the relaxation rate shown in Fig. 5.2 is essentially W_1. The overall form of the temperature dependence shown in Figs. 5.1 and 5.2 is qualitatively similar to that observed by BBR (1970). However, there are significant quantitative differences, as expected since BBR measured $(2/5)(W_1+4W_2)$ at some unspecified orientation.

5.2 Orientation dependence of the spin-lattice relaxation of ^{23}Na in $NaNO_2$

It is convenient to discuss separately the data obtained at room temperature, low temperatures (135 K, 145 K and 170 K), 235 K and 432 K.

5.2.1 Orientation dependence at room temperature

The dependence of W_1 on the orientation of the magnetic field $\vec{H}_o$ relative to the crystal, measured at room temperature (298 K), is shown in Table 4 and Fig. 5.3. As mentioned previously, the magnetic contribution to the relaxation is negligible at room temperature so that the measured relaxation rate is W_1. Approximate values of θ and ϕ were obtained from the readings of angular scales 1 and 2. More accurate values were obtained by fitting the measured frequencies of the satellites and the centre line to Eqs. (3.2) and (3.3).

The rate of recovery of both the high frequency satellite and the low frequency satellite was measured in turn. As can be seen from Table 4, they were in good agreement with one another, and only the mean values are shown in Fig. 5.3. Errors in W_1 shown in Fig. 5.3 are primarily those obtained from the scatter of the data about the best fit to an exponential recovery. However, they also include a contribution from the errors in θ and ϕ, which are believed to be about ±0.2° and ±1° respectively. These contributions were estimated using calculated values of $\partial W_1/\partial\theta$ and $\partial W_1/\partial\phi$ obtained from a preliminary fit of the data. Since these errors were independent of the intrinsic error in W_1, they were all combined in the usual way by taking the square root of the sum of the squares. This method of error analysis was used for studies of the orientation dependence at other temperatures.

The curves shown in Fig. 5.3 are the best fit of the data to Eq. (3.4), and the M-tensor components found from the fit are shown in the third column of Table 5. The errors in the M-tensor components were obtained from the scatter of the data about the best fit. They do not directly include any contribution from systematic errors such as equipment nonlinearity etc. As can be seen from Fig. 5.3, the data are in very good agreement with Eq. (3.4). A quantitative assessment of the goodness of fit is given by the χ^2 per degree of freedom (Bevington, 1969) which was found to be 1.05. (A value near unity for χ^2 per degree of freedom indicates an excellent fit.) The excellent fit to Eq. (3.4) confirms that the symmetry of the sodium site is orthorhombic, though it does not distinguish between the three possible point group symmetries 222, mm2 and mmm. The excellent fit also indicates that the spin-lattice relaxation of ^{23}Na in $NaNO_2$ at room temperature is homogeneous. In other words, it is not, for example, caused by spin diffusion to more rapidly relaxing nuclei situated near domain wall boundaries (Suzuki and Takagi, 1971; Kinase et al, ~~1985)~~.

To confirm the validity of the theory presented in section 2.3.1 and to show that the same M-tensor components determine both W_1 and W_2 (see section 2.2.3), we monitored the recovery of the centre line after it was "inverted" by a single 180° pulse. This was done at two orientations, $\theta=0°$ and $\theta=90°$, $\phi=90°$. The data were in good agreement with an equation of the form

$$M_z(\tau) = A(e^{-2W_1\tau} + e^{-2W_2\tau}) + B , \qquad (5.1)$$

(cf. Eq. (2.65)) and, from a nonlinear least squares analysis, we obtained the values shown in the first two rows of Table 6. As we can see, the values of W_1 are in quite good agreement with those obtained by monitoring the recovery of the satellite (see Table 4). The theoretical values of W_2 at $\theta=0°$ and $\theta=90°$, $\phi=90°$, obtained by substituting the M-tensor components listed in Table 5 in Eq. (3.5), are

Table 4

Orientation dependence of W_1 at 298 K obtained from the relaxation of (a) the high frequency satellite (b) the low frequency satellite.

θ(deg) ±0.2°	ϕ(deg) ±1°	W_1 (s^{-1}) (a)	(b)
15.7	0	1.011±0.027	1.033±0.027
30.7	0	1.817±0.038	1.880±0.039
40.7	0	2.169±0.036	2.230±0.041
45.7	0	2.315±0.024	2.324±0.045
75.7	0	1.120±0.027	1.134±0.026
90.7	0	0.753±0.005	0.777±0.009
40.0	45	1.994±0.027	1.917±0.035
90.0	45	1.096±0.017	1.085±0.007
1.0	90	0.582±0.010	0.583±0.004
89.0	90	0.492±0.005	0.492±0.004
79.0	90	0.659±0.013	0.659±0.013
69.0	90	1.035±0.021	1.038±0.022
39.0	90	1.622±0.034	1.592±0.041
29.0	90	1.368±0.029	1.381±0.030
14.0	90	0.840±0.018	0.835±0.020
9.0	90	0.689±0.015	0.690±0.014

Figure 5.3

Variation of W_1 with θ for ^{23}Na in $NaNO_2$ at 298 K. The solid, open and crossed data points refer to the ϕ and 0°, 45° and 90° respectively. The solid, broken and dotted curves show a least squares fit of the data to Eq. (3.4).

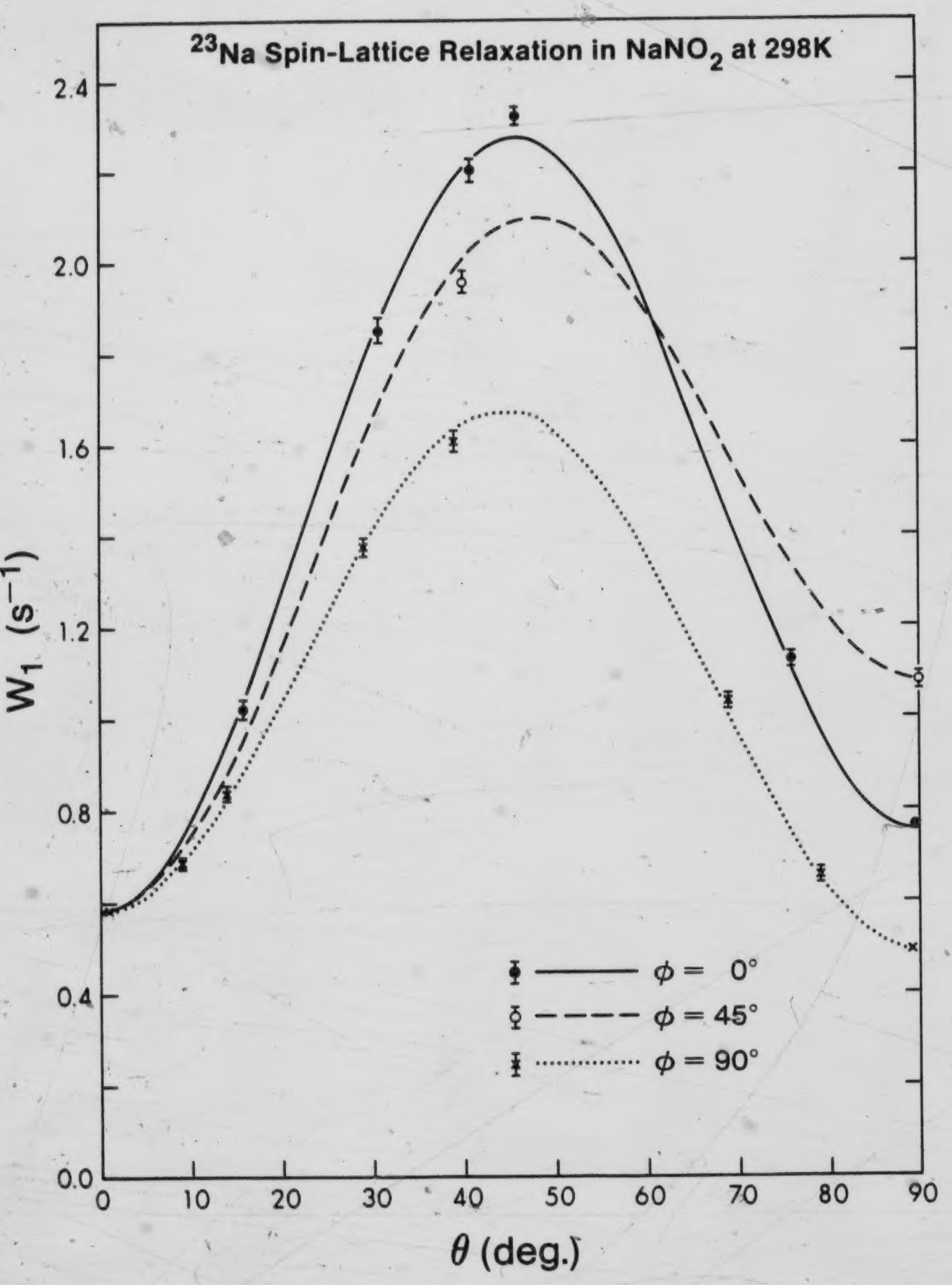
^{23}Na Spin-Lattice Relaxation in NaNO$_2$ at 298K
W_1 (s^{-1})
0.0
0.4
0.8
1.2
1.6
2.0
2.4
θ (deg.)
0
10
20
30
40
50
60
70
80
90
ϕ = 0°
ϕ = 45°
ϕ = 90°

Table 5

M-tensor components multiplied by $e^2Q^2/96$, obtained by fitting the orientation dependence of W_1 at various temperatures to Eq. (3.4).

M-tensor component	170 K ±1 K	235 K ±1 K	298 K ±1 K	432 K ±1 K
	(s^{-1})	(s^{-1})	(s^{-1})	(s^{-1})
$\frac{e^2Q^2}{96} M_{1111}$	0.0044 ±0.0003	0.1686 ±0.0016	0.2418 ±0.0022	0.361 ±0.012
$\frac{e^2Q^2}{96} M_{1133}$	-0.0037 ±0.0002	-0.1740 ±0.0020	-0.2236 ±0.0026	-0.386 ±0.012
$\frac{e^2Q^2}{96} M_{3333}$	0.0063 ±0.0002	0.2391 ±0.0020	0.3244 ±0.0026	0.831 ±0.013
$\frac{e^2Q^2}{96} M_{2323}$	0.0004 ±0.0001	0.0133 ±0.0005	0.0196 ±0.0004	0.089 ±0.007
$\frac{e^2Q^2}{96} M_{3131}$	0.0012 ±0.0001	0.0365 ±0.0005	0.0531 ±0.0004	0.303 ±0.008
$\frac{e^2Q^2}{96} M_{1212}$	0.0024 ±0.0001	0.0264 ±0.0005	0.0419 ±0.0042	0.249 ±0.007

Table 6

Values of W_1 and W_2 at various temperatures and orientations, found by fitting the recovery of the centre line to Eq. (5.1). At 145 K and 135K, the data fitted a single exponential and so W_1 and W_2 are apparently equal.

T(K) ±1 K	θ(deg) ±0.2°	φ(deg) ±1°	W_1 (s^{-1})	W_2 (s^{-1})
298	0.0	90	0.608±0.006	1.096±0.010
298	90.0	90	0.503±0.002	2.447±0.014
235	0.0	90	0.390±0.006	0.776±0.009
235	90.0	90	0.328±0.013	1.786±0.024
170	0.0	90	0.041±0.001	0.052±0.002
170	90.0	90	0.053±0.003	0.061±0.003
145	0.0	90	0.045±0.001	
145	90.0	90	0.053±0.001	
135	4.0	0	0.117±0.001	
135	43.0	0	0.184±0.001	
135	90.0	0	0.126±0.001	

1.13±0.02 and 2.45±0.02 respectively. They are in very good agreement with the measured values, confirming the validity of the theory and showing that the same M-tensor components determine W_1 and W_2 at room temperature.

5.2.2 Orientation dependence at low temperatures (135 K, 145 K and 170 K)

The orientation dependence of W_{hfs} at 170 K is shown in Table 7 and Fig. 5.4. A preliminary analysis of these data, along with the room temperature data, has been published (Towta and Hughes, 198~~5~~6). The curves show a least squares fit of the data to Eq. (3.4). The agreement is poor (χ^2 per degree of freedom is 17) showing that W_{hfs} is not well described by Eq. (3.4).

To obtain further information about the discrepancy, we determined W_1 and W_2 together by monitoring the recovery of the centre line as was done at room temperature and fitting it to Eq. (5.1). The values of W_1 and W_2 (there was no way of knowing a priori which was which) are shown in Table 6. As can be seen, the value, which we believe to be W_1, is in good agreement with the value obtained from the recovery of the satellite at $\theta=0°$. However, the agreement is poor at $\theta=90°$, $\phi=90°$.

Because of the unexpected rise in W_{hfs} observed below 160 K (see Fig. 5.1), we measured the orientation dependence at a lower temperature, 145 K. The data are

Table 7

Orientation dependence of W_{hfs} at 170 K.

θ(deg) ±0.2°	φ(deg) ±1°	W_{hfs} (s^{-1})
19.9	0	0.069±0.001
42.4	0	0.098±0.002
75.4	0	0.075±0.001
90.0	0	0.060±0.001
1.8	45	0.041±0.001
19.7	45	0.061±0.001
40.3	45	0.086±0.001
76.3	45	0.080±0.001
90.0	45	0.064±0.002
0.0	90	0.040±0.001
19.9	90	0.054±0.001
39.9	90	0.077±0.001
86.7	90	0.059±0.001

Fig. 5.4

Variation of W_{hfs} with θ for ^{23}Na in $NaNO_2$ at 170 K. The solid, open and crossed data points refer to the ϕ values 0°, 45° and 90° respectively. The solid, broken and dotted curves show a least squares fit of the data to Eq. (3.4).

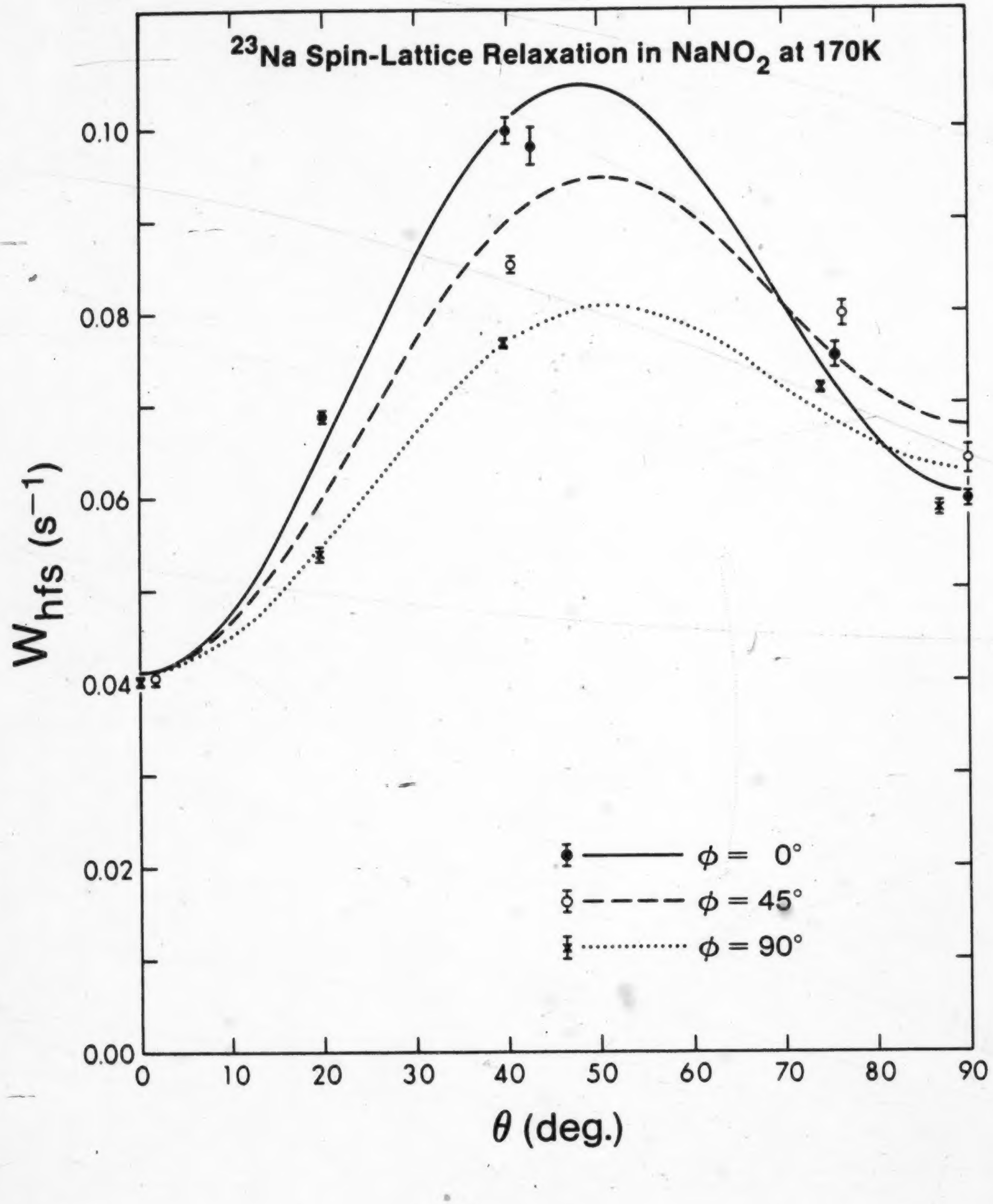

^{23}Na Spin-Lattice Relaxation in $NaNO_2$ at 170K
W_{hfs} (s^{-1})
0.00
0.02
0.04
0.06
0.08
0.10
0
10
20
30
40
50
60
70
80
90
θ (deg.)
$\phi = 0°$
$\phi = 45°$
$\phi = 90°$

listed in Table 8 and are plotted in Fig. 5.5. They are in extremely poor agreement with Eq. (3.4) (χ^2 per degree of freedom is 1371). The theoretical fit is therefore not shown. Instead, the curves in Fig. 5.5 are smooth curves drawn through the data points because we later need interpolated values.

We tried to measure W_1 and W_2 separately by monitoring the recovery of the centre line at $\theta=0°$ and $\theta=90°$, $\phi=90°$. However, it was not possible to fit the data to the sum of two exponentials (Eq. (5.1)). Instead, the data was found to fit a single exponential and the corresponding values of the transition probabilities are shown in Table 6. If the relaxation is quadrupolar at 145 K, the fact that the data fitted a single exponential can only mean that W_1 is equal to W_2. This could happen at one orientation, but is unlikely to happen at two very different orientations.

To investigate this further, we monitored the recovery of the centre line at 135 K. To be sure that we were not at orientations where W_1 and W_2 were accidentally equal, we performed the experiment at three very different orientations. Again, the recovery of the centre line was strictly exponential and the values of the relaxation rates are given in Table 6.

We showed in section 2.3.2 that, if the relaxation is entirely magnetic, the recovery of the centre line

Table 8

Orientation dependence of W_{hfs} at 145 K.

θ(deg) ±0.2°	ϕ(deg) ±1°	W_{hfs} ($\approx 4W_3$) (s^{-1})
20.4	0	0.067±0.001
40.5	0	0.083±0.001
75.3	0	0.069±0.001
89.3	0	0.048±0.001
1.9	45	0.042±0.001
39.8	45	0.066±0.001
75.2	45	0.078±0.001
90.0	45	0.067±0.001
0.0	90	0.040±0.001
19.5	90	0.051±0.001
40.0	90	0.055±0.001
74.2	90	0.077±0.001
86.8	90	0.053±0.001
89.2	90	0.051±0.001

Figure 5.5

Orientation dependence of W_{hfs} ($\approx 4W$) for ^{23}Na in $NaNO_2$ at 145 K. The smooth curves are drawn to pass through all the data points at a fixed ϕ value.

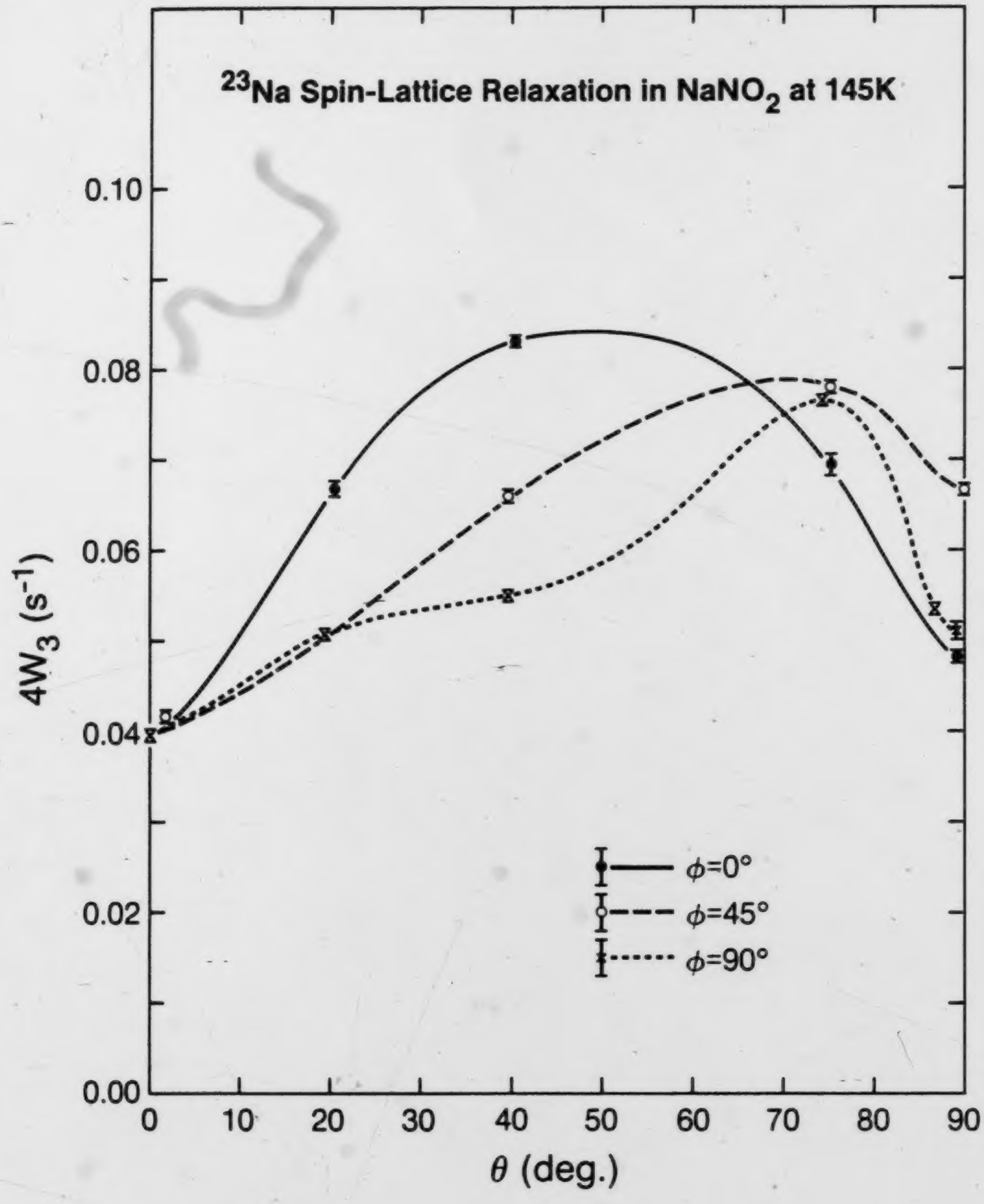
^{23}Na Spin-Lattice Relaxation in NaNO$_2$ at 145K
4W$_3$ (s^{-1})
0.00
0.02
0.04
0.06
0.08
0.10
0
10
20
30
40
50
60
70
80
90
θ (deg.)
ϕ=0°
ϕ=45°
ϕ=90°

following excitation of centre line should be of the form

$$M_z(\tau) = A\left(e^{-12W_3\tau} + (1/9)e^{-2W_3\tau}\right) + B \qquad (5.2)$$

Similarly, the recovery of the satellite following excitation of the centre line should be of the form

$$M_z(\tau) = C\left(e^{-12W_3\tau} - (1/6)e^{-2W_3\tau}\right) + B\ . \qquad (5.3)$$

Even though the $e^{-12W_3\tau}$ term is the dominant one, it should be possible to detect experimentally a nonexponential recovery of the form given by Eqs. (5.2) and (5.3). We therefore fitted the recovery of the centre line at 145 K to an equation of the form

$$M_z(\tau) = A\left(e^{-6\alpha\tau} + \lambda e^{-\alpha\tau}\right) + B \qquad (5.4)$$

where λ is included as a fitted parameter. We found λ to be -0.045 ± 0.026 at the orientation $\theta=0°$ and -0.142 ± 0.098 at $\theta=90°$, $\phi=90°$. These values are not in agreement with the theoretical value of 0.111 (see Eq. (5.2)). To check this further, we fitted the recovery of the high frequency satellite at 145 K to Eq. (5.4) at the fourteen different orientations listed in Table 7. We found the mean of the fourteen values of λ to be -0.003 ± 0.026, as compared with the expected value of -0.167 (see Eq. (5.3)). There is therefore no evidence of the nonexponentiality predicted theoretically for magnetic relaxation. We believe that this is due to the magnetic transitions between the states $m = \pm3/2$ and $m = \pm1/2$ being ineffective because of the suppression of the flip-flop transitions which contribute to spin diffusion. As was shown in section 2.3.2, the recovery of the centre line should, in that case, be exponential as observed experimentally.

It was shown in section 2.3.2 (see Eqs. (2.90) and (2.91)) that the relaxation rate of the centre line $2W_{cl}$ should be identical to the relaxation rate of the high frequency satellite $2W_{hfs}$. (Both should equal $8W_3$.) This was checked by monitoring the recovery of the high frequency satellite at 135 K. We also measured W_{cl} and W_{hfs} at 135 K and 145 K with Crystal B, our cleaved crystal. The measured values of W_{cl} and W_{hfs} are listed in Table 9. (For comparison purposes, some of the data presented in Tables 6 and 8 are presented again in Table 9.) It can be seen that, with the exception of one orientation, W_{cl} is consistently somewhat larger than W_{hfs} for both crystals at the same temperature and orientation. We attribute the small discrepancy to the fact that the satellite resonance will not be observed from ^{23}Na nuclei close to the paramagnetic centres. That is because of the large first-order quadrupole interactions expected near such centres. The centre line, on the other hand, will be observed from almost all ^{23}Na nuclei including those close to the paramagnetic centres. Since the effective magnetic relaxation rate will decrease with increasing distance from the paramagnetic centre, one would expect that the centre line would recover somewhat faster than the observed part of the high frequency satellite.

Table 9

Half the relaxation rate of the centre line, W_{cl}, and half the relaxation rate of the high frequency satellite, W_{hfs}, measured at different orientations and temperatures.

Temp.(K) ±1 K	θ(deg) ±0.2°	φ(deg) ±1°	W_{cl} (s^{-1})	W_{hfs} (s^{-1})
135	4.0	0	0.0586±0.0003	0.0557±0.0008
135	42.9	0	0.0921±0.0006	0.1002±0.0004
135	90.0	0	0.0629±0.0004	0.0596±0.0004
135	0.0	0	0.0505±0.0007*	0.0471±0.0006*
145	0.0	0	0.0420±0.0003*	0.0392±0.0007*
145	0.0	90	0.0453±0.0002	0.0396±0.0003

*Obtained with Crystal B.

In order to determine the quadrupolar contribution to the relaxation we observed at 170 K (see Fig. 5.4), we need to determine the magnitude of the magnetic relaxation at that temperature. We believe that the increase in W_{hfs} below 160 K shown in Fig. 5.1 is the high temperature side of what is called a "T_1 minimum". A T_1 minimum, or a maximum in the relaxation rate, occurs when the local magnetic field (or electric field gradient for quadrupolar nuclei) fluctuates at a frequency close to the Larmor frequency (Bloembergen, Purcell and Pound, 1948; Abragam, 1961). If the cause of the fluctuating magnetic field involves a thermally activated process, then a plot of the logarithm of T_1 (or its reciprocal the relaxation rate) against 1/T will be linear on either side of the "T_1 minimum", and the activation energy can be determined from the slopes. Guided by that, we plotted the logarithm of all the W_{hfs} values obtained with both crystals against 1/T as shown in Fig. 5.6. The solid circles are measurements made with our cylindrical crystal at $\theta=4°$, $\phi=0°$; except for the point at 145 K which was taken earlier at $\theta=0°$. The value of W_{hfs} for this data point has been increased slightly to correspond to $\theta=4°$, $\phi=0°$ using the graph shown in Fig. 5.5. The open circles in Fig. 5.6 refer to the cleaved crystal and were taken at $\theta=0°$. To correspond to $\theta=4°$, $\phi=0°$, they were also increased slightly using the graph in Fig. 5.5. We see that the data for both crystals are in good agreement. Also, the data appear to

Figure 5.6

Logarithm of W_{hfs}' plotted versus 1/T at low temperatures. The solid (open) data points refer to Crystal A (Crystal B). The broken line is a linear extrapolation of the low temperature behaviour.

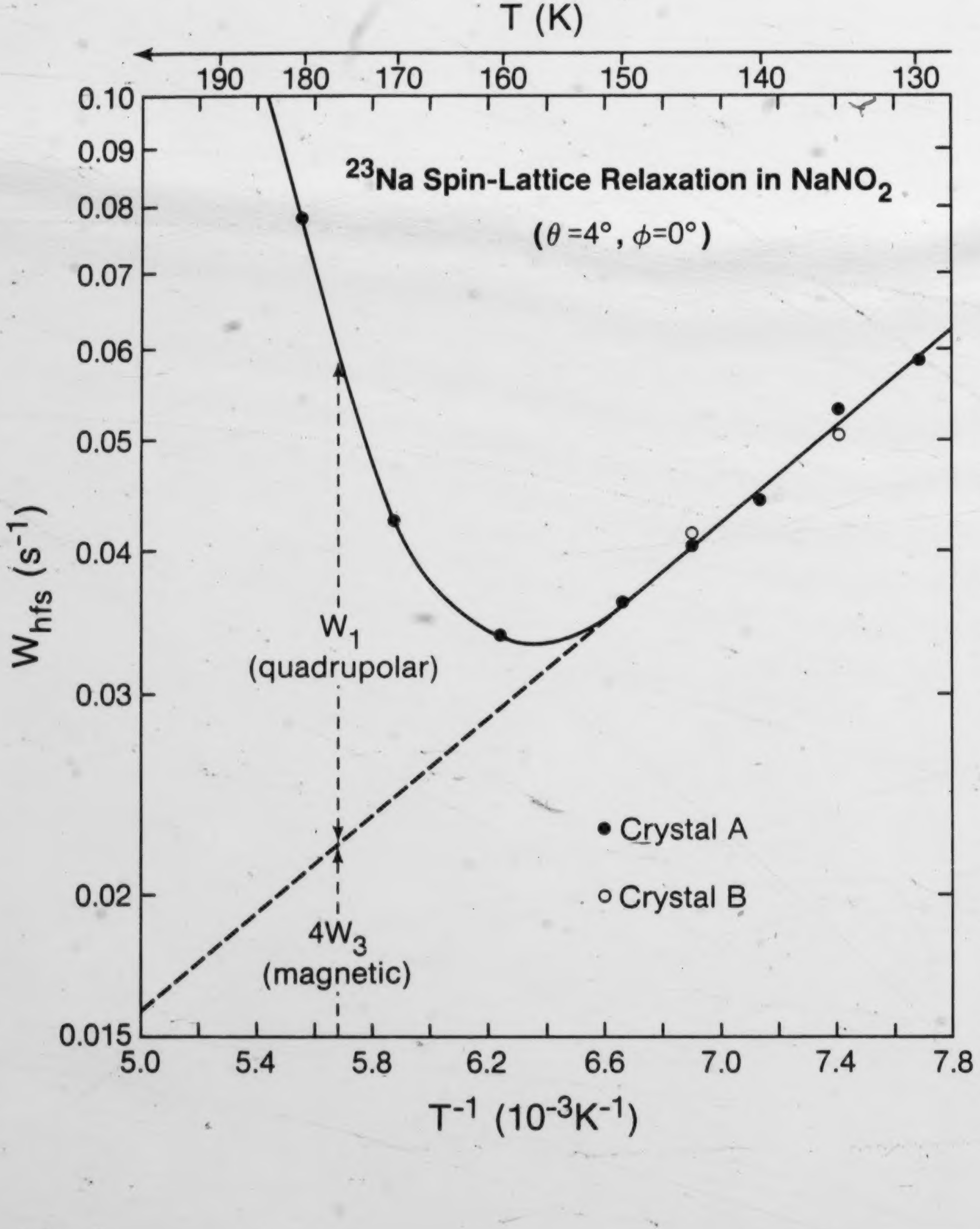
T (K)
190
180
170
160
150
140
130
0.10
0.09
0.08
0.07
0.06
0.05
0.04
0.03
0.02
0.015
^{23}Na Spin-Lattice Relaxation in NaNO$_2$
(θ =4°, ϕ=0°)
W_{hfs} (s^{-1})
W_1
(quadrupolar)
$4W_3$
(magnetic)
● Crystal A
○ Crystal B
5.0
5.4
5.8
6.2
6.6
7.0
7.4
7.8
T^{-1} ($10^{-3}K^{-1}$)

Also, the data appear to fall on a straight line, as expected if we are seeing the "tail" of a T_1 minimum caused by a thermally activated process. It would have been desirable to have extended our measurements to lower temperatures. However, it would have meant completely redesigning our probe. We believe that the magnetic relaxation we have observed is related to the T_1 minimum observed at lower temperatures by Abe et al. (1972) in a NQR study of ^{14}N in $NaNO_2$. This is discussed in section 6.

In order to remove the magnetic contribution from the observed relaxation rates at 170 K and higher temperatures, it seems reasonable to extrapolate the magnetic relaxation to higher temperatures as shown by the dashed line. Moreover, according to our earlier interpretation of the exponential nature of the relaxation, W_{hfs} must equal $4W_3$. The extrapolation shown in Fig. 5.6 refers to the orientation $\theta=4°$, $\phi=0°$. We assumed that the temperature dependence was the same at all orientations, so that by combining the orientation dependence shown in Fig. 5.5, and the temperature dependence shown in Fig. 5.6, the value of $4W_3$ can be determined at any required orientation and temperature.

As we showed in section 2.3.3, the recovery of the satellite should be nonexponential if the magnetic and quadrupole relaxations are of comparable strength as they seem to be at 170 K. Using the values of $4W_3$ obtained from

Figs. 5.5 and 5.6, a least squares fit of the 170 K data (earlier fitted to a single exponential) was made to Eq. (2.103) with W_1, W_2, E and the amplitude of the FID in thermal equilibrium as fitted parameters. The values of W_1 from from the fit are listed in Table 10. The data point at $\theta=39.7°$. $\phi=0°$ is not plotted in Fig. 5.7 and was not included in the fit. That is because W_2 came out to be negative and the value of W_1 was a long way off the fitted curve. Also excluded is the data point at $\theta=73.8°$, $\phi=90°$. That is because it is close to the orientation at which we found inconsistent values of W_{hfs}. In addition to being inconsistent, they also tended to be higher than expected. We attribute this to an additional relaxation mechanism possibly involving cross-relaxation to the ^{14}N, ^{15}N or ^{17}O spin systems in the crystal. In section 2.3.3, we showed that if $W_1-W_2 << 16W_3^2$ and if W_1 and W_2 are not very different from each other, then W_1 can be found by simply subtracting $4W_3$ from W_{hfs}. The results of such a subtraction is shown in the last column of Table 10. They are in surprisingly good agreement with the values obtained by fitting the data to Eq. (2.103) (except for the data point at $\theta=39.7°$, $\phi=0°$ which gave a negative value of W_2). It is therefore a reasonable approximation to consider W_1 to be the difference between the continuous curve drawn through the data points in Fig. 5.6 and the dashed line representing the magnetic relaxation, at least for temperatures

Table 10

Orientation dependence of $4W_3$ and W_1 at 170 K.

θ(deg) ±0.2°	φ(deg) ±1°	$4W_3(s^{-1})$ ±0.002	W_1 (from 4 parameter fit)(s^{-1})	$W_1=W_{hfs}-4W_3$ (s^{-1})
19.9	0	0.0405	0.0285	0.0283±0.0021
39.7	0	0.0508	0.0650	0.0488±0.0025*
42.4	0	0.0513	0.0474	0.0467±0.0024
90.0	0	0.0596	0.0299	0.0299±0.0021
1.8	45	0.0249	0.0164	0.0156±0.0021
19.7	45	0.0317	0.0306	0.0290±0.0022
40.3	45	0.0409	0.0450	0.0452±0.0022
76.3	45	0.0474	0.0325	0.0323±0.0024
90.0	45	0.0411	0.0232	0.0228±0.0026
0.0	90	0.0244	0.0160	0.0159±0.0021
19.9	90	0.0316	0.0223	0.0223±0.0022
39.9	90	0.0340	0.0422	0.0426±0.0021
86.7	90	0.0333	0.0254	0.0254±0.0021

*This point is not included in the fit.

below about 170 K. The orientation dependence of W_1 at 170 K, obtained by fitting to the sum of two exponentials, are shown in Fig. 5.7. The curves show a least fit of the data to Eq. (3.4). Taking into account the uncertainty of about ±0.002 in the value of $4W_3$, the values of W_1 are in quite good agreement with Eq. (3.4) and give a χ^2 per degree of freedom of about unity. The corresponding values of the M-tensor components are listed in the first column of Table 5.

The values of W_2 at the various crystal orientations, determined from the fit to Eq. (2.103), have large errors associated with them. They are in fair agreement with values calculated using Eq. (3.5) and the M-tensor components listed in Table 5 (except for the data point at $\theta=39.7°$, $\phi=0°$ which gave a negative value of W_2).

5.2.3 Orientation dependence at 235 K

The orientation dependence of W_{hfs} was measured at 235 K, a temperature approximately midway between 170 K temperature and room temperature at which the other measurements of W_1 were made. The data are shown in Table 11. In section 2.3.3, we showed theoretically that, if $16W_3^2 << (W_1-W_2)^2$, then the relaxation of the satellite is approximately exponential and the corresponding relaxation rate is $2(W_1+2W_3)$. At 235 K, the extrapolated magnetic relaxation is small whereas the quadrupole relaxation is

Figure 5.7

Variation of W_1 with θ for ^{23}Na in $NaNO_2$ at 170 K. The solid, open and crossed data points refer to the ϕ values 0°, 45° and 90° respectively. The solid, broken and dotted curves show a least squares fit of the data to Eq.(2.4).

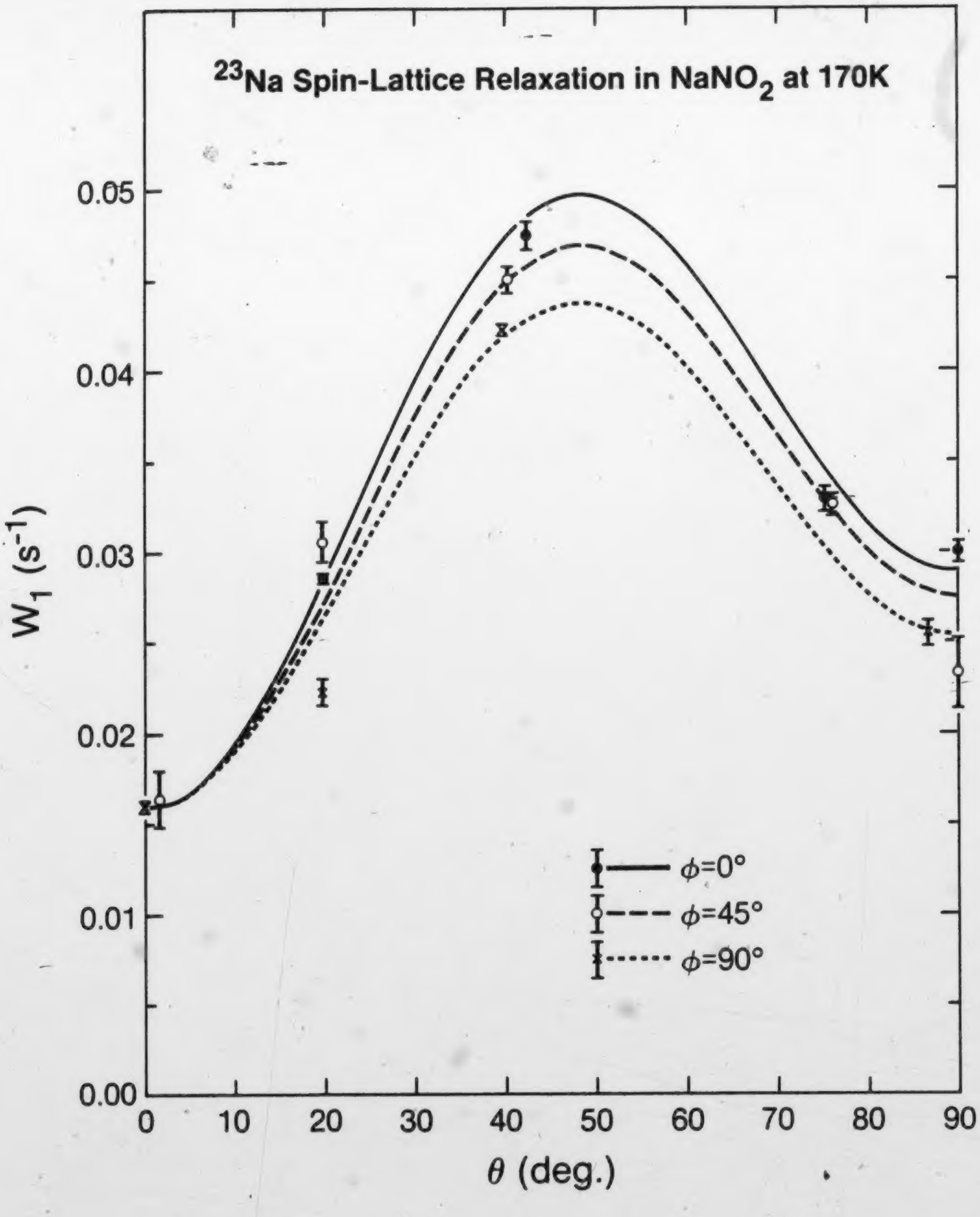
^{23}Na Spin-Lattice Relaxation in NaNO$_2$ at 170K
W_1 (s^{-1})
0.00
0.01
0.02
0.03
0.04
0.05
0
10
20
30
40
50
60
70
80
90
θ (deg.)
ϕ=0°
ϕ=45°
ϕ=90°

Table 11

Orientation dependence of W_{hfs} and W_1 at 235 K.

θ(deg) ±0.2°	φ(deg) ±1°	W_{hfs} (s^{-1})	$4W_3(s^{-1})$ ±0.002 s^{-1}	$W_1=W_{hfs}-2W_3$ (s^{-1})
1.3	0	0.407±0.005	0.012	0.401±0.006
21.4	0	0.972±0.012	0.020	0.962±0.012
41.2	0	1.681±0.014	0.024	1.657±0.014
76.2	0	0.793±0.010	0.020	0.773±0.010
81.3	0	0.642±0.010	0.017	0.625±0.011
91.3	0	0.504±0.005	0.015	0.489±0.006
0.5	45	0.410±0.004	0.012	0.398±0.005
39.1	45	1.476±0.017	0.019	1.457±0.017
74.5	45	1.048±0.012	0.023	1.025±0.012
89.5	45	0.789±0.001	0.020	0.769±0.002
18.4	90	0.660±0.010	0.015	0.645±0.010
38.4	90	1.121±0.011	0.016	1.105±0.011
88.5	90	0.328±0.003	0.015	0.313±0.004

relatively large, and so the condition $16W_3^2 << (W_1-W_2)^2$ is well satisfied. We therefore subtracted $2W_3$ from the measured value of W_{hfs} to remove the magnetic contribution. The values are listed in the last column of Table 11 and are shown in Fig. 5.8. The curves show a least squares fit of the data to Eq. (3.4) and the χ^2 per degree of freedom is 4.6. The values of the M-tensor components are listed in the second column of Table 5.

5.2.4 Orientation dependence at 432 K

The orientation dependence of W_1 was measured at 432 K, near the critical point at 438 K. (The magnetic relaxation is, of course, negligible at this temperature.) As can be seen in Fig. 5.2, W_1 varies very rapidly with temperature near the critical point. Since we could not rely on the temperature being stable to better than about ±0.2°C over the period necessary to complete all the measurements, we felt we could not make measurements closer to the critical point than 432 K. The data are presented in Table 12 and are plotted in Fig. 5.9. The curves show a least squares fit of the data to Eq. (3.4) and the χ^2 per degree of freedom is 1.8. The values of the M-tensor components are listed in the fourth column of Table 5.

5.3 Temperature dependence of the quadrupole coupling constant and asymmetry parameter of ^{23}Na in $NaNO_2$

While measuring the temperature dependence of W_{hfs}, we noted the frequencies of the high frequency satellite

Figure 5.8

Variation of W_1 with θ for ^{23}Na in $NaNO_2$ at 235 K. The solid, open and crossed data points refer to the ϕ values 0°, 45° and 90° respectively. The solid, broken and dotted curves show a least squares fit of the data to Eq.(3.4).

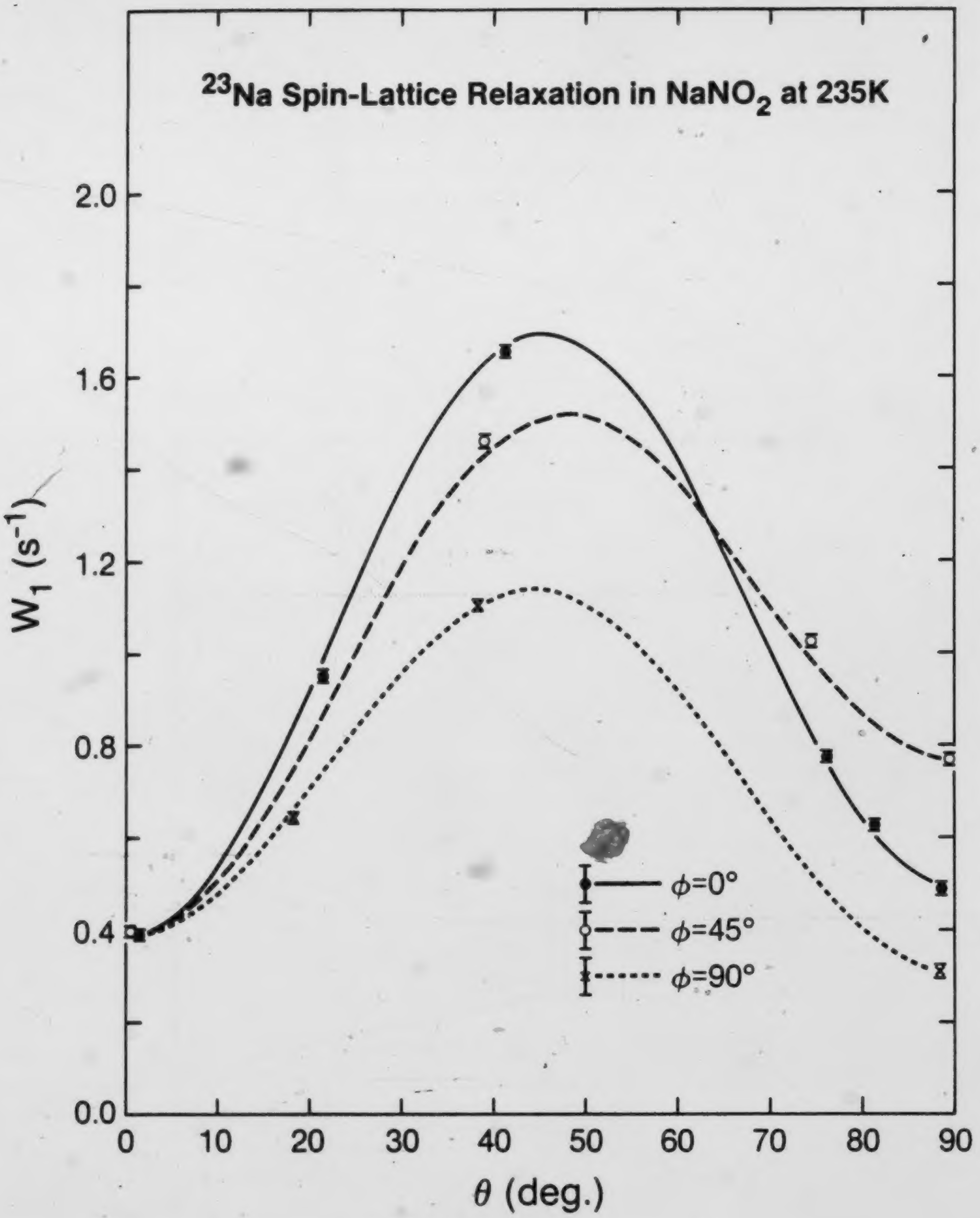
^{23}Na Spin-Lattice Relaxation in NaNO$_2$ at 235K
W_1 (s^{-1})
θ (deg.)
0.0
0.4
0.8
1.2
1.6
2.0
0
10
20
30
40
50
60
70
80
90
ϕ=0°
ϕ=45°
ϕ=90°

Table 12

Orientation dependence of W_1 at 432 K.

θ(deg) ±0.2°	ϕ(deg) ±1°	W_1 (s^{-1})
0	0	3.065±0.055
20	0	2.901±0.042
35	0	4.736±0.119
77	0	4.761±0.072
90	0	4.239±0.097
20	45	4.279±0.041
35	45	5.420±0.117
77	45	3.551±0.055
90	45	3.028±0.046
20	90	4.626±0.079
35	90	6.091±0.079
77	90	3.395±0.037
90	90	2.726±0.046

Figure 5.9

Variation of W_1 with θ for ^{23}Na in $NaNO_2$ at 432 K. The solid, open and crossed data points refer to the ϕ values 0°, 45° and 90° respectively. The solid, broken and dotted curves show a least squares fit of the data to Eq.(3.4).

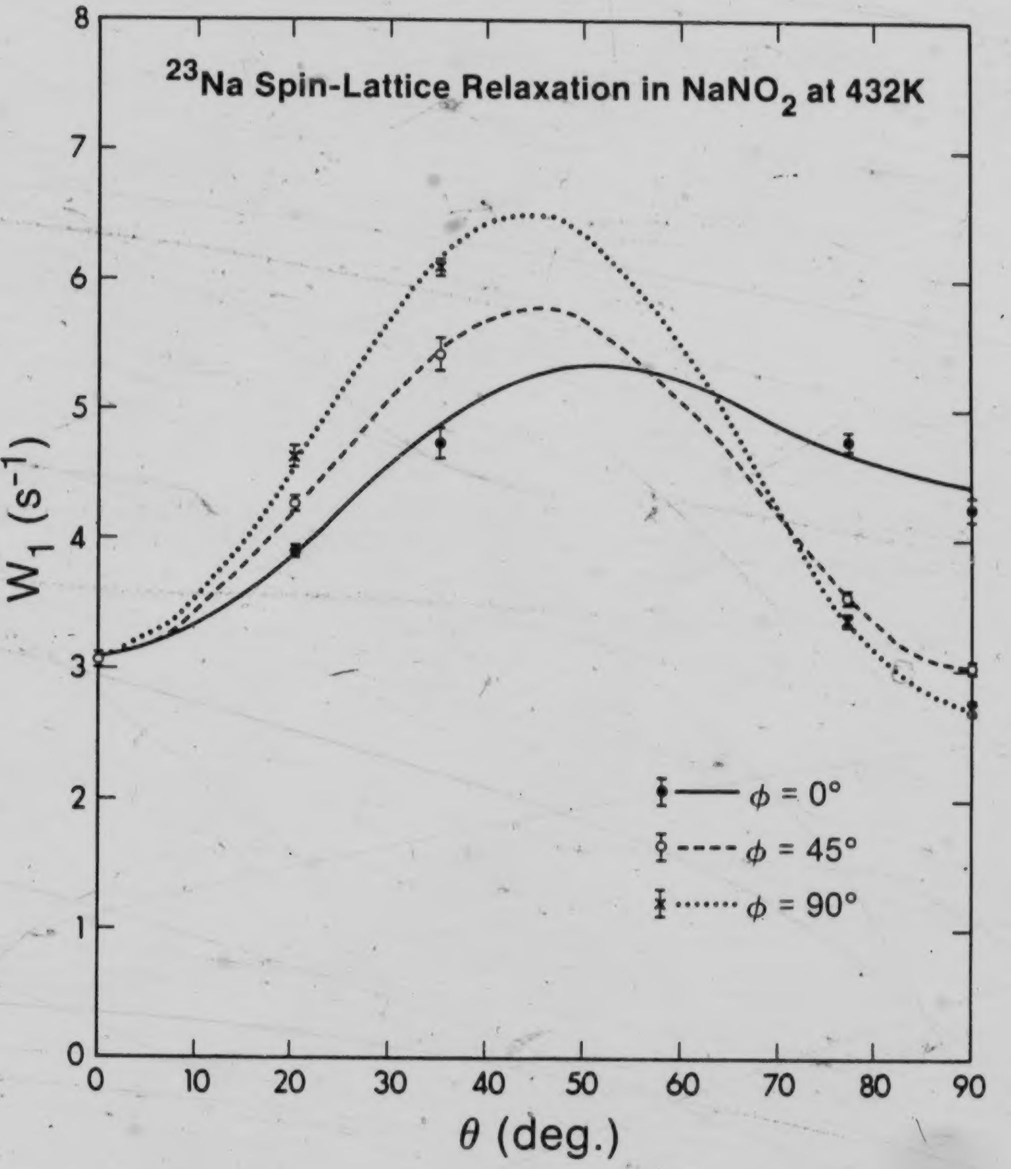
^{23}Na Spin-Lattice Relaxation in NaNO$_2$ at 432K
W_1 (s^{-1})
θ (deg.)
0
1
2
3
4
5
6
7
8
0
10
20
30
40
50
60
70
80
90
ϕ = 0°
ϕ = 45°
ϕ = 90°

and the centre line. By substituting these values and the known values of θ and ϕ in Eqs. (3.2) and (3.3), we were able to determine the quadrupole coupling constant, e^2qQ/h, of ^{23}Na in $NaNO_2$. Our values are shown as a function of temperature in Table 13 and Fig. 5.10, and are believed to be accurate to within ±0.2 kHz. They are in good agreement with values found by Weiss and Biedenkapp (1962) above room temperature. There are no previously reported values of the quadrupole coupling constant below room temperature. However, as can be seen from Fig. 5.3, the variation of the quadrupole coupling constant is smooth in that range. We see no evidence of a discontinuity in the slope of the graph near 170 K where other workers (Gesi, 1965; Ema et al, 1975) have observed anomalies which they attributed to a phase transition.

By fitting the frequencies of the high frequency satellite and centre line, measured during our studies of the orientation dependence of W_{hfs}, to Eqs. (3.2) and (3.3), we were also able to determine a few values of the asymmetry parameter η. These are given in Table 14 and plotted in Fig. 5.10. We see that η decreases below room temperature. Since it also decreases above room temperature (Weiss and Biedenkapp, 1962) as discussed in section 3.2, it evidently has a maximum value 0.109 near room temperature.

Table 13

Quadrupole coupling constant e^2qQ/h at various temperatures

T(K) ±1 K	(e^2qQ/h ±0.2) kHz	T(K) ±1 K	(e^2qQ/h ±0.2) kHz
130.0	1143.2	328.6	1081.5
140.1	1142.3	336.0	1076.2
150.0	1141.1	343.4	1071.2
107.0	1139.5	350.8	1065.2
170.2	1138.2	358.2	1059.6
180.0	1135.4	365.6	1052.4
189.9	1133.3	373.0	1044.9
200.2	1130.6	380.4	1036.1
210.3	1128.2	387.8	1028.0
220.3	1125.5	395.2	1017.3
224.9	1124.5	402.6	1005.1
229.8	1122.7	410.0	990.7
239.8	1119.7	417.4	974.0
250.1	1116.4	424.8	951.8
280.8	1104.9	432.2	921.0
290.0	1100.9	435.4	897.0
299.0	1098.8	396.6	848.2
300.0	1097.2	443.3	837.4
306.4	1093.6	447.0	830.5
313.8	1089.5	454.4	815.3
321.8	1086.0	461.8	801.2

Table 14

Asymmetry parameter η at various temperatures

T(K) ±1 K	η±0.005
145	0.1023
170	0.1030
235	0.1076
298	0.1091

Figure 5.10

The solid circles show the quadrupole coupling constant e^2qQ/h plotted as a function of temperature. The open circles show the asymmetry parameter η plotted as a function of temperature. The solid and broken curves are smooth curves drawn through the data points.

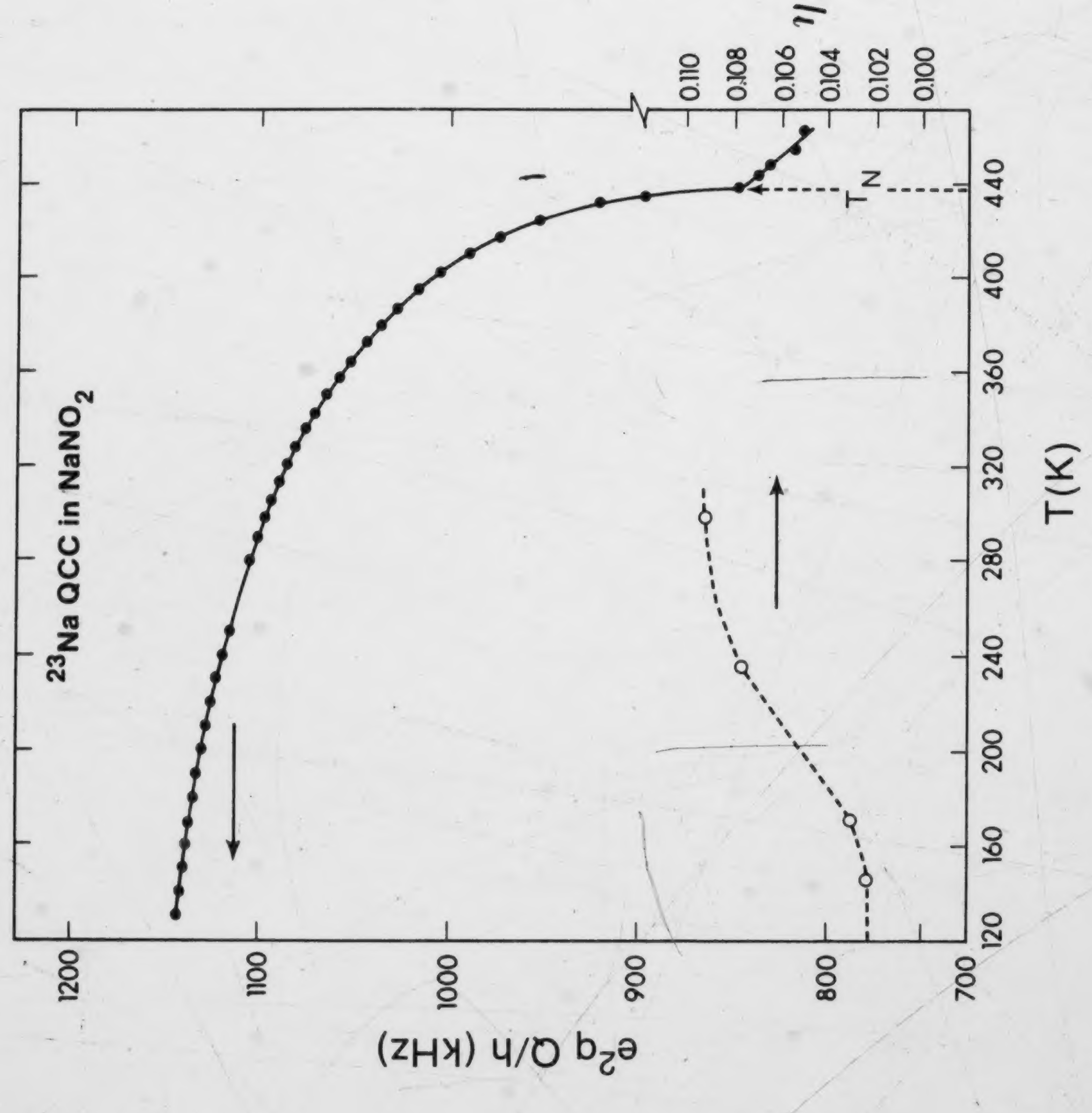
^{23}Na QCC in NaNO$_2$
$e^2q\,Q/h$ (kHz)
1200
1100
1000
900
800
700
120
160
200
240
280
320
360
400
440
T(K)
T_N
η
0.110
0.108
0.106
0.104
0.102
0.100

5.4 Electron spin resonance spectrum of a single crystal of $NaNO_2$

The low temperature ^{23}Na spin-lattice relaxation data seemed to indicate the presence of paramagnetic centres in our crystals. We therefore ran a few exploratory electron spin resonance (ESR) spectra on Crystal B. Crystal A was too large to fit into the microwave cavity. Crystal B was rather large but could be fitted in at some orientations of the crystal relative to the external magnetic field. The spectra were run by Mr. G. Bigam in our Department of Chemistry on a Bruker ER-100 spectrometer.

Fig. 5.11 shows the ESR spectrum obtained when the magnetic field was perpendicular to the $\underset{\sim}{b}$ axis and made an angle of about 25° with the $\underset{\sim}{c}$ axis. (Because of its size, it was impossible to orient the crystal so that the magnetic field was exactly parallel to $\underset{\sim}{c}$ axis.) Fig. 5.12 shows the ESR spectrum run under similar conditions but with the magnetic field parallel to the a axis. In Fig. 5.11, a prominent ESR signal, approximately Lorentzian in shape, is observed at a magnetic field strength of 2239 G. Substituting this value and the frequency $\nu = 9.392$ GHz into the equation (Poole, 1967(a))

$$\nu = 1.4\times10^{6} gH_{o} \qquad (5.5)$$

where H_o is in Gauss, we find that the g factor is 3.00. The peak-to-peak derivative linewidth is approximately 175 G. The spectrum shown in Fig. 5.12 is very different from

Figure 5.11

ESR spectrum of Crystal B with the magnetic field perpendicular to the $\underset{\sim}{b}$ axis and making an angle of about 25° with the $\underset{\sim}{c}$ axis. The field markers are in gauss.

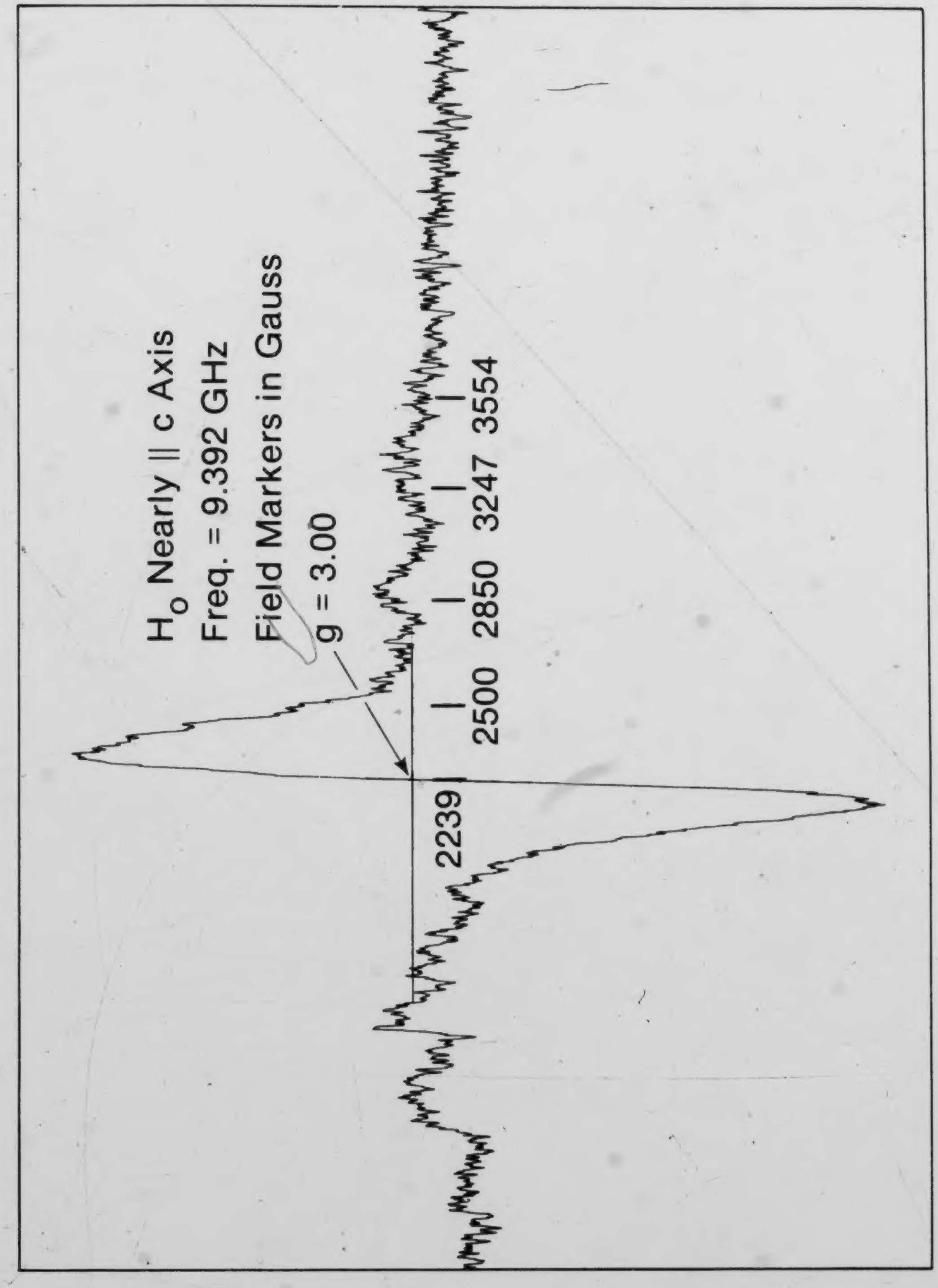
H_o Nearly ∥ c Axis
Freq. = 9.392 GHz
Field Markers in Gauss
g = 3.00
2239
2500
2850
3247
3554

Figure 5.12

ESR spectrum of Crystal B with the magnetic field parallel to the $\underset{\sim}{a}$ axis. The field markers are in gauss.

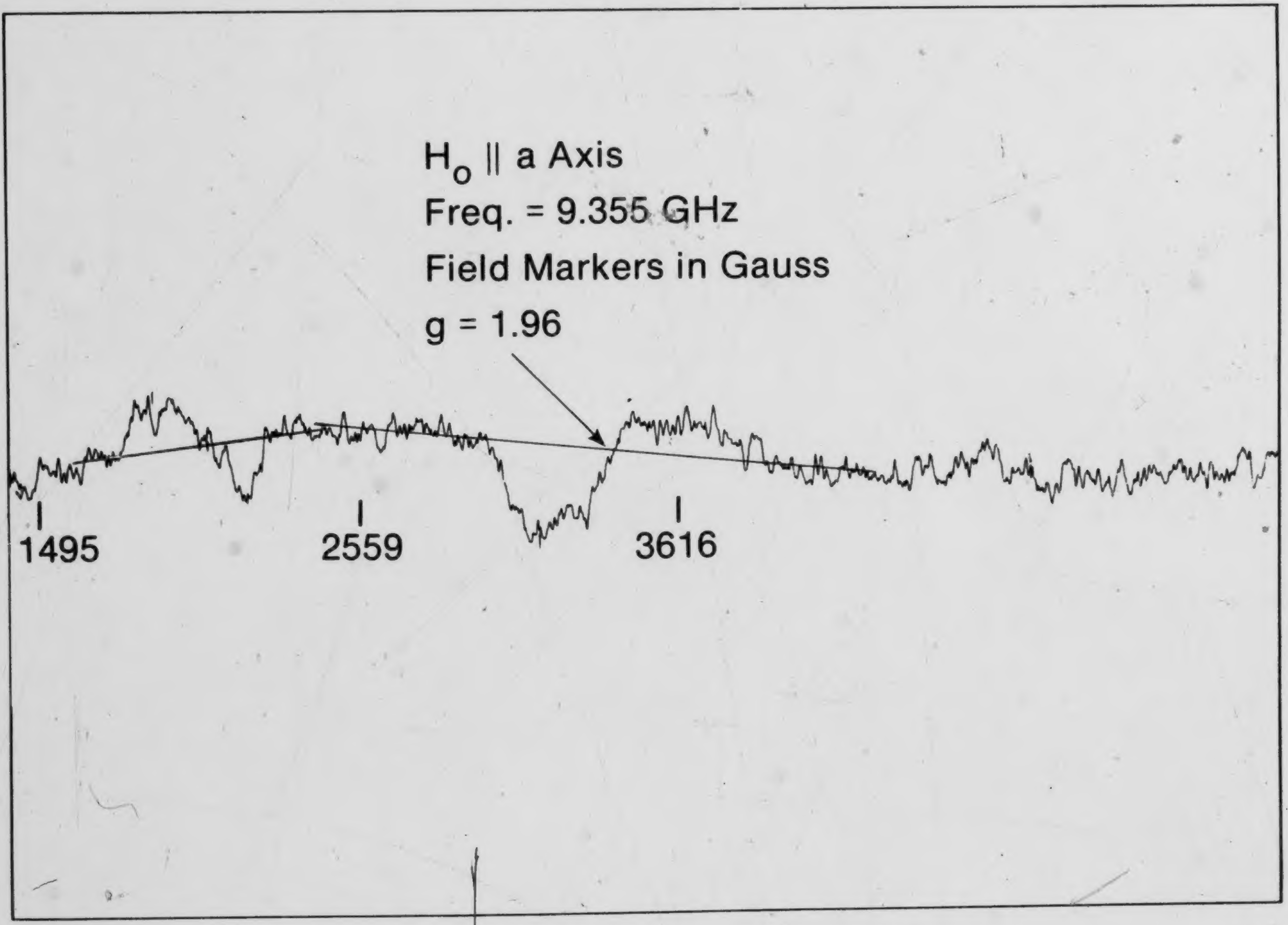
H_o || a Axis
Freq. = 9.355 GHz
Field Markers in Gauss
g = 1.96
1495
2559
3616

that in Fig. 5.11. A weak asymmetric broad resonance is seen at a field of 3400 G corresponding to a g factor of about 1.96. There is apparently another weak signal at about 2050 G corresponding to a g factor of 3.26. However, it is of opposite phase to that expected.

According to the manual of the ESR spectrometer, a signal-to-noise ratio of approximately 120 would be obtained from $2.5\times10^{10}\Delta H$ spins, where ΔH is the linewidth, using a 0.3 ml sample, a one second time constant and the optimum modulation amplitude. The spectra in Figs. 5.11 and 5.12 were obtained from a smple of volume 0.6 ml, using a time constant of 0.1 second and a peak-to-peak modulation amplitude of 10 G, well below the optimum value. The RMS noise amplitude is proportional to the square root of the bandwidth or inversely proportional to the square root of the time constant. By using a peak-to-peak modulation amplitude of 10 G instead of the optimum value of roughly 700 G, the amplitude of the signal in Fig. 5.11 is reduced by a factor of about 17.5 (Poole, 1967(b)). Thus, under our conditions, we would expect a signal-to-noise ratio of roughly $120\times0.6/0.3\times17.5\times\sqrt{10} = 4.4$ from $2.5\times10^{10}\times175 = 4.38\times10^{12}$ spins. The signal-to-noise ratio of the signal in Fig. 5.11 is about 20, corresponding to $4.38\times10^{12}\times20/4.4 = 2\times10^{13}$ spins. Since the density of $NaNO_2$ is 2.17 g/cm^3, the mass of our crystal is 1.3 grams and the number of molecules of $NaNO_2$ is 1.1×10^{22}. The molar concentration of paramagnetic spins is therefore $2\times10^{13}/1.1\times10^{22}$ or about 2×10^{-9}. This value should be regarded as a lower limit since the ESR spectrometer may not have been operating under the optimum conditions. But it would seem that the concentration of paramagnetic centres is probably of the order of 1 part in 10^8 and almost certainly less than 1 ppm.

CHAPTER 6

DISCUSSION

6.1 Temperature dependence of the spin lattice relaxation

The temperature dependence of $(2/5)(W_1+4W_2)$, measured by BBR (1970) at an orientation where the satellites overlap the centre line, is shown in Fig. 6.1. It is qualitatively similar to our data shown in Figs. 5.1 and 5.2. At 160 K, and $\theta=0°$ we measured a magnetic relaxation rate $2W_{hfs} = 0.06\ s^{-1}$. Assuming that the orientation dependence is similar to that found at 145 K (see Fig. 5.5), this implies a magnetic relaxation rate of about 0.1 s^{-1} in the vicinity of the overlap orientation used by BBR. It is not possible to tell from BBR's graph whether T_1 at 160 K is indeed 0.1 s^{-1} or close to zero. So BBR's data do not help to answer the question whether the magnetic relaxation we observed at low temperatures is present in all $NaNO_2$ crystals.

We note that the temperature dependence of the quadrupole relaxation rate observed by us and by BBR (1970) is very different from the T^2 dependence expected if the relaxation is predominantly caused by phonons (Van Kranendonk, 1954; Van Kranendonk and Walker, 1967; Van Kanendonk and Walker, 1968). Also, the relaxation rates of ^{23}Na observed in $NaNO_2$ are about an order of magnitude

Figure 6.1

The spin-lattice relaxation rate $T^{-1} = (2/5)(W_1+4W_2)$ of ^{23}Na in a single crystal of $NaNO_2$ measured as a function of temperature by Bonera et al. (1970). The solid (open) circles refer to measurements made at a frequency of 24 MHz (8 MHz).

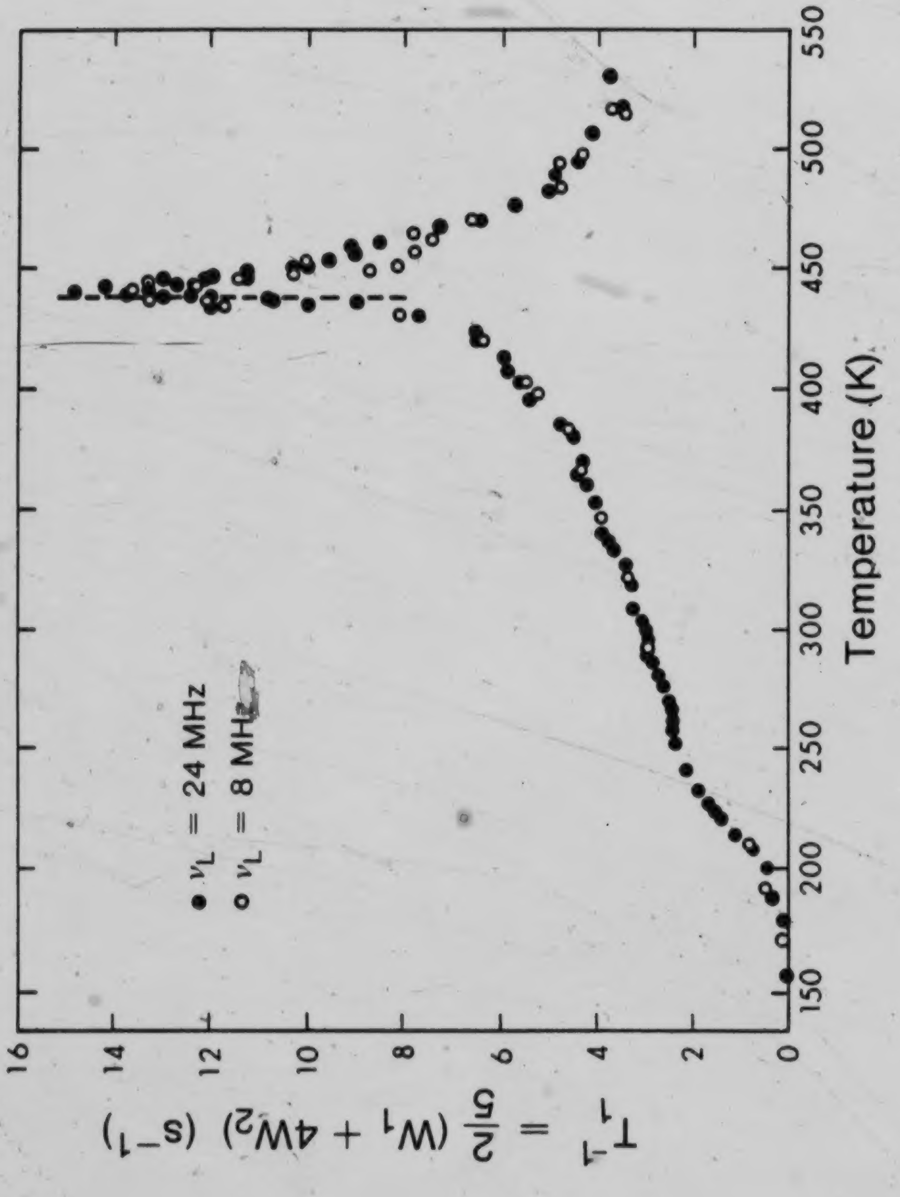
● ν_L = 24 MHz
○ ν_L = 8 MHz
$T_1^{-1} = \frac{5}{2}(W_1 + 4W_2)$ (s^{-1})
0
2
4
6
8
10
12
14
16
Temperature (K)
150
200
250
300
350
400
450
500
550

larger than those observed at the same temperature in other ionic crystals of sodium, such as $NaNO_3$ (Kasahara et al., 1977), NaCl (Wikner et al., 1960), and NaF and NaI (Weber, 1963). The observed quadrupole relaxation is therefore not likely to be caused by phonons

Between room temperature and the critical point, we observed (see Fig. 5.2) an increase in W_1 of a factor of ten. The data of BBR (1970) show an increase of only a factor of five. That could be because of a larger temperature gradient across the crystal in BBR's work than ours. However, the values of $(2/5)(W_1+4W_2)$ obtained by Avogadro et al. (1975) (though not necessarily measured at exactly the same angles θ and ϕ) are in approximate agreement with BBR's data. Avagagro et al. presumably had quite a uniform temperature across the sample since they were particularly interested in the relaxation rate very near the critical point. That indicates that the difference between our data and BBR's is real, and it shows that the M-tensor components do not all scale in the same way with temperature.

6.2 Cause of the observed magnetic relaxation

Magnetic relaxation is caused by fluctuating magnetic fields caused by nuclear magnetic dipoles or electronic magnetic dipoles. As indicated in section 5.2.2, the exponential approach to equilibrium of the centre line and satellites indicates that spin diffusion, associated with flip-flop transitions $m = \pm 3/2 \leftrightarrow \pm 1/2$ and $m = \pm 1/2 \leftrightarrow \pm 3/2$

between neighbouring nuclei, is inhibited. That implies that there must be substantial inhomogeneous quadrupole broadening of ^{23}Na near the source of the magnetic relaxation. That, in turn, points to paramagnetic centres as being the case of the magnetic relaxation we observe. A rough estimate of N, number of electronic spins per unit volume that would account for the observed relaxation rate, can be obtained by substituting in the formula

$$\frac{1}{T_1} = 4\pi bND \tag{6.1}$$

(de Gennes, 1958; Abragam, 1961). Here, b is a length of the order of the internuclear distance which we take to be equal to $\underset{\sim}{a}$ or 3.56×10^{-8}cm, and D is the spin diffusion coefficient which is $\sim Wa^2$ where W is the rate of flip flops between nearest neighbours. Taking W to be $10^3\ s^{-1}$, we find D to be approximately $10^{-12}cm^2/s$. Taking T_1 to be 10 s, corresponding to W_{hfs} in the magnetic region of 0.05 s^{-1}, and substituting in Eq. (6.1), we find that N is $2.2\times10^{17}cm^{-3}$. That corresponds to a molar concentration of 1.2×10^{-5} (or an atomic concentration of 3×10^{-6}). Such a concentration is much higher than that indicated by the ESR study. That would point to nuclear magnetic dipoles as being the cause of the magnetic relaxation. However, to confirm this, ESR measurements should be made on small portions of our crystals and compared with ESR spectra obtained under the same conditions from reference samples containing a known number of spins. If the concentration of paramagnetic centres is found to be high, we suggest that a chemical analysis should be carried out to see whether the paramagnetic centres are impurities. However, we doubt that the magnetic relaxation is caused by impurities, since the relaxation rates we found with Crystals A and B, which were obtained from different sources, are so similar. Also, the relaxation rate should not vary strongly with temperature because it involves spin diffusion which is temperature independent. If the relaxation is not caused by paramagnetic impurities, we suggest they may be associated with electrons trapped in anion vacancies in the lattice. These would be similar to F centres (Markham, 1966) but would be intrinsic defects, in other words characteristic of the pure crystal in thermal equilibrium. F centres are known to cause coloration of alkali halides (Markham, 1966). They would presumably do the same for $NaNO_2$ and could account for the yellowish colour of that material.

The other possibility is that the magnetic relaxation is caused by the motion of magnetic nuclei through the lattice. However, the motion must be of such a kind as to leave the lattice electrically unchanged, otherwise the relaxation would be predominantly quadrupolar. One possible motion is a reorientation of the NO_2 group through 180° about the $\underset{\sim}{b}$ axis. Calculation of the energetics of the reorientation of NO_2 groups in $NaNO_2$ (Ehrhardt and Michel,

1981) shows that reorientation about the $\underset{\sim}{b}$ axis is very improbable. However, Hughes (1986) calculated the relaxation rate of the ^{23}Na nuclei caused by the magnetic field fluctuation due to the longitudinal component of the magnetic moment of ^{17}O nuclei in NO_2 groups reorienting about the $\underset{\sim}{b}$ axis. The isotopic abundance of ^{17}O is so low (0.037%) that the calculated relaxation rate is more than two orders of magnitude smaller than that observed. Motion of the ^{14}N nuclei (isotopic abundance 99.6%) could, however, account for the order of magnitude of the observed relaxation. Self diffusion of the NO_2 groups could account for the observations, though it seems unlikely to occur sufficiently rapidly at low temperatures. Another possibility is that the NO_2 groups are undergoing frequent inversion as a result of the rapid passage of 180° domain walls. (Provided all the NO_2 groups were inverted simultaneously, the quadrupole interaction would remain the same and so there would be no strong quadrupole relaxation.)

The temperature dependence of the spin-lattice relaxation time of ^{14}N, measured down to 4.2 K by Abe et al. (1972) in a nuclear quadrupole resonance (NQR) study, is shown in Fig. 6.2. The ν_- and ν_+ refer to the two resonances observed because η is non-zero (Das and Hahn, 1958). Measurements were later made by Petersen and Bray (1976) on the same spin system. However, their work was done above 77 K and so they did not observe the T_1 minima.

Figure 6.2

The spin-lattice relaxation time T_1 of ^{14}N in $NaNO_2$ powder measured as a function of temperature in an NQR study by Abe et al. (1972). The solid (open) circles refer to the ν_+ (ν_-) resonance.

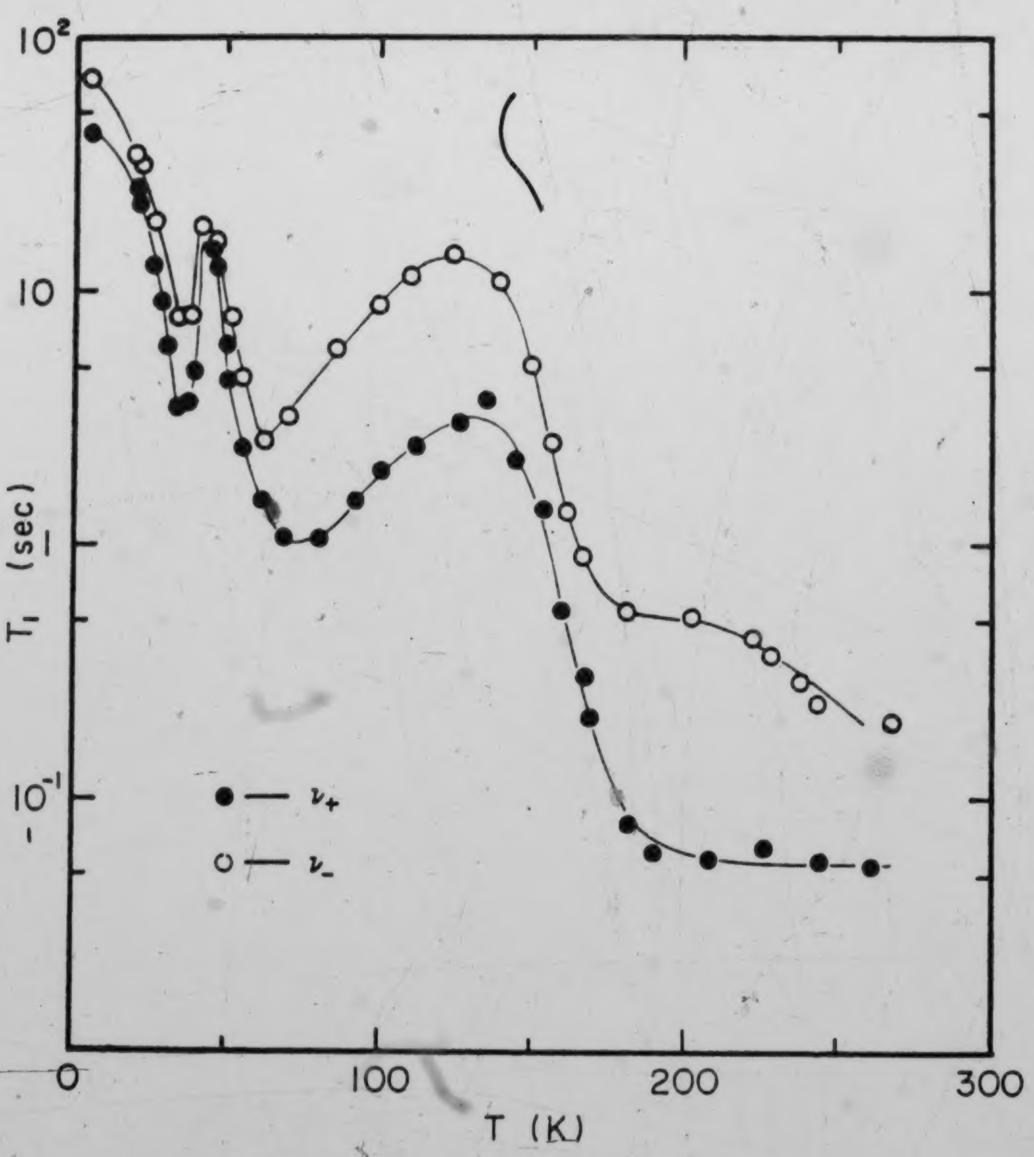
10^2
10
1
10^{-1}
T_1 (sec)
0
100
200
300
T (K)
● — ν_+
○ — ν_-

We believe that the T_1 minima, observed by Abe et al. at 36 K for both the ν_+ and ν_- resonances, at 64 K for the ν_- resonance and at 80 K for the ν_+ resonance, are related to the increase in magnetic relaxation we observed at low temperatures. We therefore believe that the relaxation they observed at temperatures below 150 K is magnetic and not quadrupolar as they stated. In particular, we propose that the minima observed for both resonances at 36 K occur when the frequency of the fluctuating magnetic field is ~1.74 MHz, the difference in frequency between the + and - levels or, in other words, the frequency of the difference line (Marino and Bray, 1968). The minimum at 64 K occurs when the frequency of the fluctuating magnetic field is ~3.759 MHz, the frequency of the ν_- resonance, and the minimum at 80 K occurs when the frequency of the fluctuating magnetic field is ~4.933 MHz, the frequency of the ν_+ resonance. If the motion is thermally activated, then the logarithm of the frequency should vary linearly with 1/T. As is shown in Fig. 6.3, the three points do lie on the same straight line. However, our data indicate that the T_1 minimum occurs below 130 K for ^{23}Na (resonance frequency ≈ 14.5 MHz). As can be seen in Fig. 6.3, our data point does not lie on the same straight line as the points of Abe et al. (1972), though that is possibly because of large errors in reading the temperatures at which the minima occur in Fig. 6.2.

Figure 6.3

Logarithm of f_{min}, the frequency difference between pairs of energy levels, plotted against the reciprocal of the temperature at which the relaxation time, associated with transitions between the levels, is a minimum. The closed circles refer to the minima observed by Abe et al. (1972) (see Fig. 6.2). The open circle refers to the minimum which we believe occurs for ^{23}Na in $NaNO_2$ below 130 K. The temperatures at which the minima occur are shown in brackets.

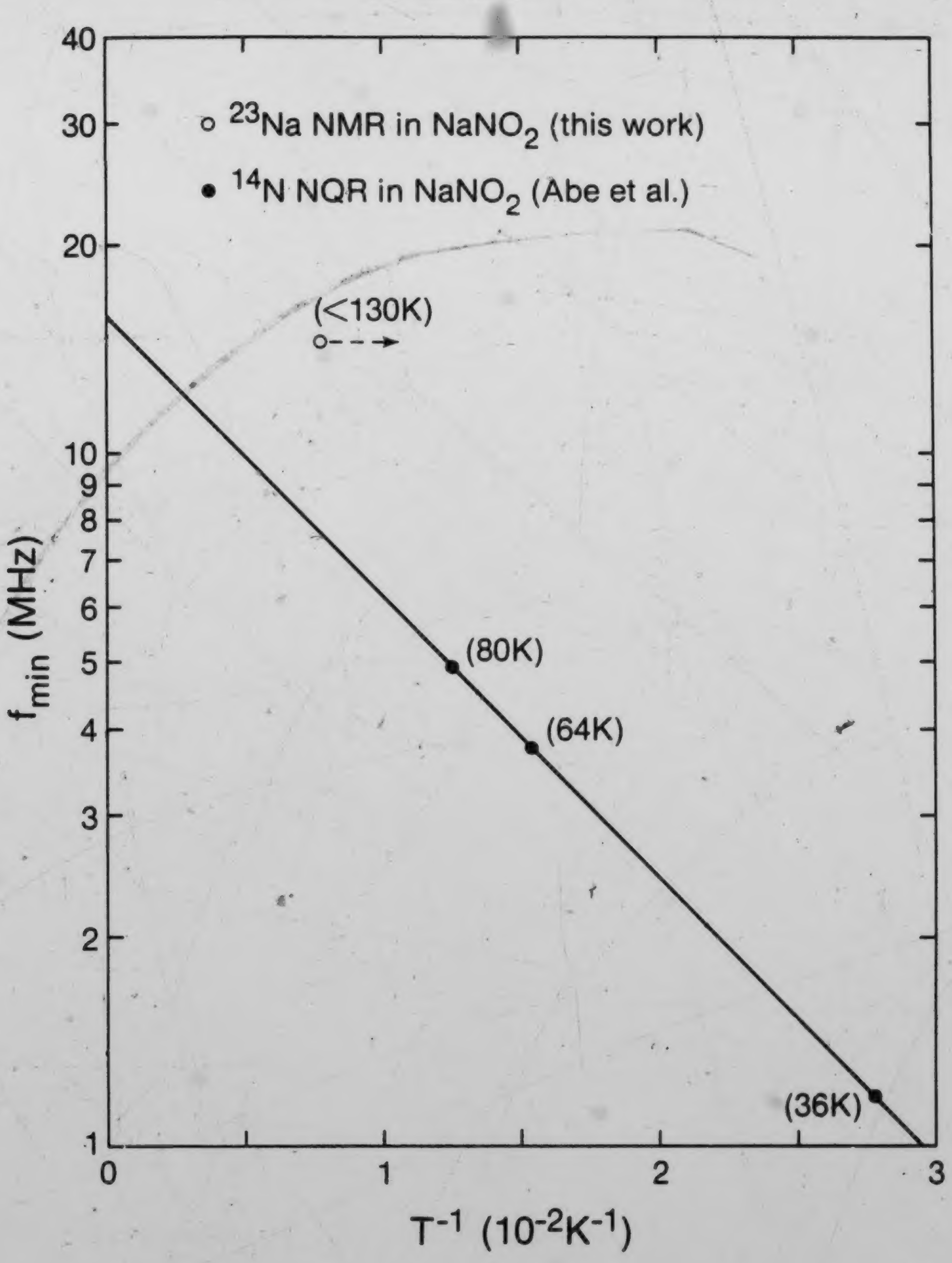
○ ^{23}Na NMR in NaNO$_2$ (this work)
● ^{14}N NQR in NaNO$_2$ (Abe et al.)
(<130K)
(80K)
(64K)
(36K)
f_{min} (MHz)
T^{-1} ($10^{-2}K^{-1}$)
40
30
20
10
9
8
7
6
5
4
3
2
1
0
1
2
3

The slope of the straight line in Fig. 6.3 is ΔE/k, so that ΔE, the activation energy of the thermally activated process causing the T_1 minima, is 791 J/mole (or 0.189 kcal/mole). If our "data point" in Fig. 6.3 is taken into account, an activation energy $\gtrsim$ 1000 J/mole (0.24 kcal/mole) is indicated. It is also possible to estimate the activation energy from the asymptotic values of the slope of the graph of the relaxation rate (or relaxation time) versus 1/T on either side of the T_1 minimum. The slope of the graph of the logarithm of W_{hfs} versus 1/T below 150 K, shown in Fig. 5.6, points to an activation energy of approximately 4.1×10^3 J/mole (0.98 kcal/mole). Estimates of the activation energy can also be obtained from the asymptotic slopes on either side of the T_1 minima shown in Fig. 6.2. These are listed in Table 15. As can be seen, there is a very large scatter in the values of the activation energy. The reason for this is not known. The average of all the values is about 2×10^3 J/mole (or 0.5 kcal/mole).

6.3 Orientation dependence of the quadrupole relaxation at and below room temperature

It can be seen from Eqs. (2.43) and (2.48) that all M-tensor components of the form $M_{\alpha\beta\alpha\beta}$ should be positive. As can be seen from Table 5, that is the case for M_{1111}, M_{3333}, M_{2323}, M_{3131} and M_{1212} at all the temperatures studied. The component M_{1133} can be positive or negative,

Table 15

Values of the activation energy derived from the asymptotic values of the slopes of the graph of T_1 versus T on either side of the T_1 minima in Fig. 6.2.

Asymptotic region	T_1 minimum	Activation Energy	
		J/mole	kcal/mole
Low temperature	ν_- at 36 K	830	0.198
High temperature	ν_- at 36 K	4.4×10^3	1.05
Low temperature	ν_- at 64 K	3.4×10	0.806
High temperature	ν_- at 64 K	1.7×10^3	0.412
Low temperature	ν_+ at 36 K	1.3×10^3	0.303
High temperature	ν_+ at 36 K	3.3×10^3	0.787
Low temperature	ν_+ at 80 K	3.7×10^3	0.874
High temperature	ν_+ at 80 K	2.2×10^3	0.529

but is found to be negative at all temperatures. Also, M_{1133} satisfies the relation $M_{1133}^2 < M_{1111}M_{3333}$ (Snyder and Hughes, 1971).

The ratios of the M-tensor components at the various temperatures are shown in Table 16. They are normalized with respect to M_{3333}, instead of M_{1111} as in our earlier publication (Towta and Hughes, 1986), because the 3 axis (z axis) is the symmetry axis of the crystal. Also shown in Table 16 are the ratios obtained at room temperature by Hughes and Spencer (1982). There are small discrepancies between our room temperature ratios and Hughes and Spencer's, showing that there are significant but not serious systematic errors in their data or ours.

We see that the ratios of the M-tensor components are quite similar at 235 K and 298 K, indicating that the quadrupole relaxation mechanism is essentially the same at both temperatures. However, it is not obvious what the mechanism is. As mentioned in section 6.1, the relaxation is unlikely to be caused by phonons because its magnitude is large and is far from being proportional to T^2.

The ratios of the M-tensor components at 170 K are significantly different from those at room temperature and 235 K. More obvious than the difference in the ratios of the M-tensor components is the fact that W_1 at 170 K is almost completely independent of ϕ (see Fig. 5.7). If the dependence on 2ϕ vanishes, it implies that $M_{2323} = M_{3131}$ and

Table 16

Values of the ratios of the M-tensor components at different temperatures derived from our data. Experimental values obtained by Hughes and Spencer (1982) are also shown for comparison.

Ratio	170 K	235 K	298 K	432 K	296 K*
$\frac{M_{1111}}{M_{3333}}$	0.690 ±0.045	0.781 ±0.009	0.745 ±0.009	0.435 ±0.016	0.668 ±0.014
$\frac{M_{1133}}{M_{3333}}$	-0.593 ±0.033	-0.728 ±0.010	-0.689 ±0.010	-0.465 ±0.016	-0.594 ±0.013
$\frac{M_{2323}}{M_{3333}}$	0.117 ±0.028	0.056 ±0.002	0.060 ±0.001	0.107 ±0.009	0.051 ±0.003
$\frac{M_{3131}}{M_{3333}}$	0.187 ±0.015	0.153 ±0.003	0.164 ±0.002	0.365 ±0.011	0.186 ±0.008
$\frac{M_{1212}}{M_{3333}}$	0.380 ±0.017	0.111 ±0.002	0.129 ±0.002	0.300 ±0.010	0.134 ±0.005

*Values obtained by Hughes and Spencer (1982).

$M_{1133} = -M_{3333}/2$ (see Eq. 3.4), and the crystal is behaving as though the symmetry is tetragonal (Snyder and Hughes, 1971). Since the contribution of the cos 4ϕ term in Eq. (3.4) is also very small at 170 K, it suggests that the motion giving rise to the quadrupole relaxation at that temperature has azimuthal symmetry about $\underset{\sim}{b}$ axis i.e. is totally independent of ϕ. This could be explained by supposing that the relaxation was caused by the motion of distant charged defects along the $\underset{\sim}{b}$ axis. However, it is not possible for NO_2 vacancies, for example, to move along the $\underset{\sim}{b}$ axis. Also, it is not obvious in that case why the θ dependence in Fig. 5.7 is so strong. Model calculations are needed to study this further.

Theoretical estimates of the ratios of the M-tensor components were obtained for simple lattice motions using the point charge model as outlined in section 2.2.4. The results of these are presented in Table 17, along with the room temperature data for comparison purposes. All the theoretical values were obtained using a model in which each sodium nucleus is assumed to be surrounded by seven point charges representing the seven nearest neighbour atoms. (More distant neighbours need not be considered in an approximate calculation since the fluctuations in field gradient due to a point charge at a distance r fall off as r^{-4}, and so the contribution of a point charge to the M-tensor component falls off as r^{-8}.) The effective charges

Table 17

Theoretical values of the ratios of the M-tensor components calculated for simple point charge models. For comparison, the experimental ratios at 298 K are also shown.

Ratio	a	b	c	d	Experimental at 298 K
$\frac{M_{1111}}{M_{3333}}$	0.272	0.092	0.188	0.240	0.745 ±0.009
$\frac{M_{1133}}{M_{3333}}$	-0.346	-0.302	-0.434	-1.497	-0,689 ±0.010
$\frac{M_{2323}}{M_{3333}}$	0.477	0.428	1.184	0.271	0.060 ±0.001
$\frac{M_{3131}}{M_{3333}}$	0.248	0.366	5.766	0.614	0.164 ±0.002
$\frac{M_{1212}}{M_{3333}}$	0.312	0.016	0.727	0.817	0.129 ±0.002

a) Isotropic, uncorrelated vibration of equal amplitude of the Na nucleus and the seven nearest neighbours.

b) Reversal of NO_2 groups only.

c) Small angular oscillation of NO_2 groups about the $\underset{\sim}{a}$ axis only.

d) Small angular oscillation of NO_2 groups about the $\underset{\sim}{c}$ axis only.

on the oxygen and nitrogen atoms were taken to be -0.562 e and +0.124 e respectively.

The values in the first column were obtained by assuming that the sodium ion (nucleus) and the seven nearest neighbours vibrate isotropically, with equal amplitude and in an uncorrelated manner. The values shown in the second column were obtained by assuming that the Na nucleus ~~is~~ stationary and the surrounding NO_2 ions reverse their orientation, as they are believed to do near the critical point. It was assumed that the coordinates of the nitrogen and oxygen atoms along the $\underset{\sim}{b}$ axis are exchanged as a result of the reversal. The values in the third and fourth columns of Table 17 were obtained by assuming that the nucleus is stationary and that the NO_2 groups undergo uncorrelated small angle oscillations about the $\underset{\sim}{a}$ and $\underset{\sim}{c}$ axes respectively. For all the calculations except the reversal of NO_2 groups, fluctuations in the electric field gradient were assumed to be linear in the the atomic displacements. In the fourth column, only the four nearest neighbour oxygen atoms were taken into consideration. If the three more distant neighbours are also taken into account, the ratios remain the same except for M_{2323}/M_{3333} which increases from 0.271 to 2.82. The theoretical ratios shown in the first three columns of Table 17 bear little relationship to the experimental values. The values in the fourth column show the same trend as the experimental ones but are a factor of roughly 3 to 5 too large. It may be that approximations made in the model cause M_{3333} to be seriously underestimated. If so, this may indicate that the "quadrupole" relaxation at and below room temperature may be due mainly to an oscillation of the NO_2 groups about the $\underset{\sim}{c}$ axis. If this is so, then the small experimental value of M_{2323}/M_{3333} presumably indicates that the fluctuations in the electric field gradient are primarily due to the four nearest oxygen atoms which are in four NO_2 groups which lie on adjacent axes to the ^{23}Na nucleus. That would indicate a degree of covalency in the bonding to these four nearest oxygen atoms. This interpretation was put forward in our recent paper (Towta and Hughes, 1986). We now wish to propose an alternative explanation hinted at in section 6.2, namely that $NaNO_2$ contains a significant concentration, $\sim 10^{-4}$ perhaps, of NO_2 vacancies in thermal equilibrium. A concentration $\sim 10^{-4}$ would account for the substantial inhomogeneous quadrupole broadening of ^{23}Na satellites, which always seems to be observed in $NaNO_2$ crystals. We propose that these vacancies diffuse at a sufficient rate to give rise to the quadrupole relaxation observed above 150 K. Moreover, the relaxation rate might be expected to increase exponentially, as initially observed (see Figs. 5.1 and 5.6), because the process is thermally activated. Such vacancies would be expected to jump parallel to the $\underset{\sim}{a}$ axis. We have not calculated the ratios of the M-tensor components resulting from such a motion. However, since the best agreement between experiment and theory in Table 17 was obtained by postulating small oscillations of NO_2 groups about the $\underset{\sim}{c}$ axis in which charges move essentially parallel to the $\underset{\sim}{a}$ axis, we suspect that motion of vacancies parallel to the $\underset{\sim}{a}$ axis would also give rise to ratios of the M-tensor components in rough agreement with the experimental values. Much more work is obviously needed in this area.

6.4 Orientation dependence of the quadrupole relaxation at 432 K

It can be seen from BBR's data (Fig. 6.1) and from our data (Figs. 5.1 and 5.2) that the ^{23}Na relaxation rate varies almost linearly with temperature from about 240 K to 350 K, at which point it increases more rapidly toward the critical point. A similar anomalous behaviour above about 350 K is observed in the specific heat (Hatta and Ikushima, 1973) and thermal expansion coefficients (Ema et al., 1975). Guided by this, we subtracted off the "background" (noncritical) contribution to W_1 in order to study the relaxation associated with the critical phenomenon. (Provided the two relaxation contributions are independent, the measured transition probability should be the sum of the two individual contributions.) Our W_1 data in the range 200 K to 410 K is shown in Fig. 6.4 and the solid line is a

Fig. 6.4

Values of W_{hfs} ($\equiv W_1$) plotted against temperature between 200 K and 410 K. The solid circles were measured at $\theta=0°$ and are taken from Fig. 5.2. The open circles were measured at $\theta=4°$. $\phi=0°$ and are taken from Fig. 5.1. The solid line passing through P (corresponding to a temperature of 432 K) is an extrapolation of the linear behaviour below about 340 K. The point Q shows the value of the "background" contribution to W_1 at 432 K used in the text to determine the critical contribution. The broken line parallel to the ordinate axis indicates the temperature (432 K) at which the high temperature data were taken.

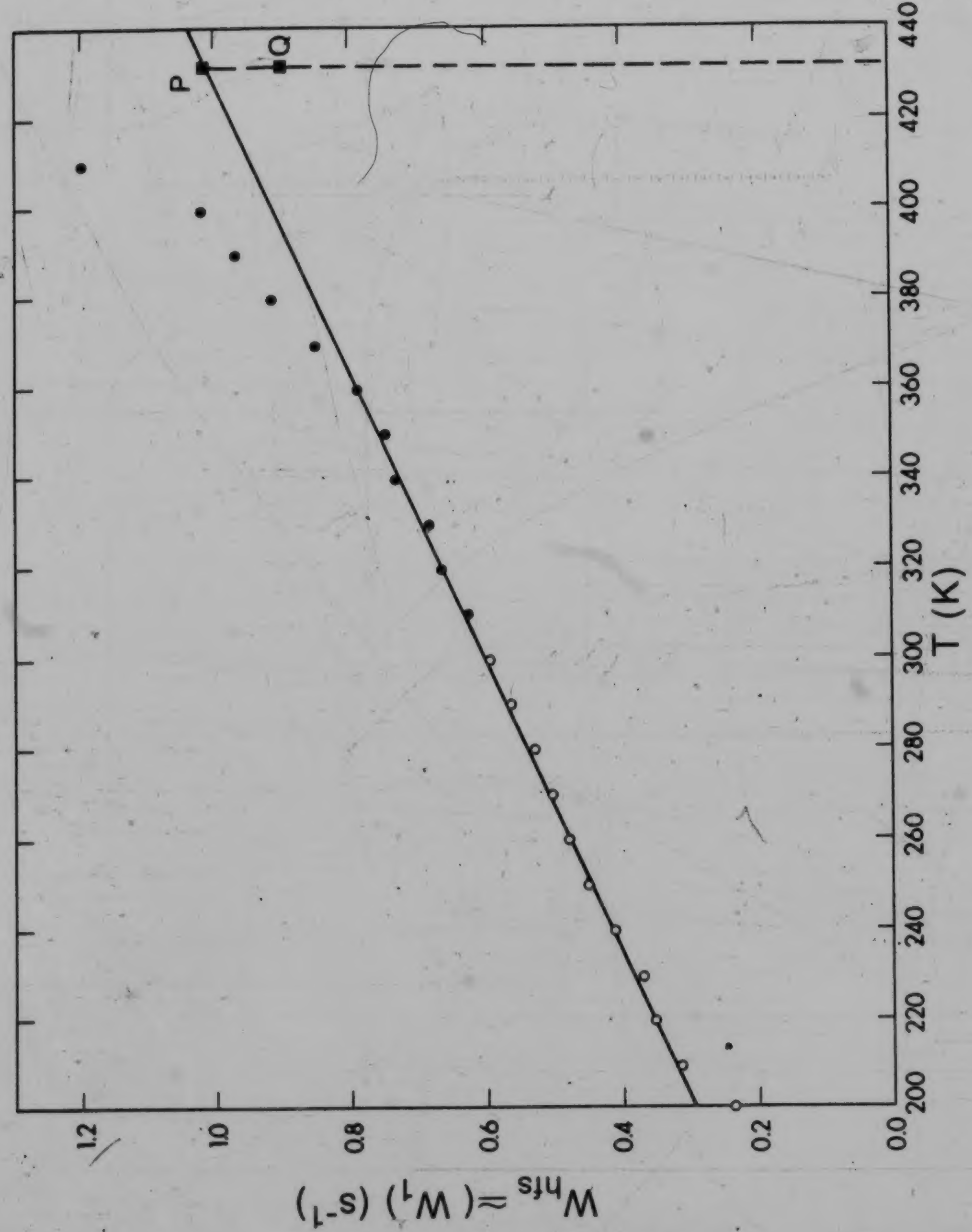
$W_{hfs} \approx \langle W_1 \rangle$ (s^{-1})
1.2
1.0
0.8
0.6
0.4
0.2
0.0
200
220
240
260
280
300
320
340
360
380
400
420
440
T (K)
P
Q

best fit to the data in the linear region. We initially took the "background" value of W_1 at 432 K to be 1.013 s^{-1}, the value at P given by the linear extrapolation to the data. It was then assumed that the orientation dependence of the "background" contribution at 432 K was identical to that observed at 298 K (see Fig. 5.3), except that it was scaled by a factor 1.013/0.595, the ratio of the extrapolated value of W_1 at $\theta=0°$ and 432 K, to the value at $\theta=0°$ obtained by fitting the orientation dependence of W_1 at 298 K. By fitting the "critical" contrtibution to W_1 to Eq. (3.4), it was found that $(e^2Q^2/96)(M_{1111})_{crit}$ was -0.051 s^{-1}. That is of course unphysical since $(M_{1111})_{crit}$ must be positive. We therefore rejected the extrapolated value represented by P in Fig. 6.4. Instead, we assumed that $M_{1111})_{crit}$ was zero at 432 K. This implies that the "background" contribution to W_1 at 432 K is 0.899 s^{-1} corresponding to the point Q in Fig. 6.4. This value was then used in conjunction with the orientation dependence of W_1 at 298 K to remove the "background" contribution. The values of the M-tensor components associated with the critical contribution to the relaxation are listed in Table 18. The ratios of these M-tensor components are listed in Table 19, along with the theoretical values obtained by assuming reversal of the NO_2 groups (see second column of Table 17). The agreement between experiment and theory is only fair. Even though the theoretical model is very crude and the

Table 18

M-tensor components associated with the critical contribution to the relaxation at 432 K.

M-tensor component	Value at 432 K (s^{-1})
$\frac{e^2Q^2}{96}(M_{1111})_{crit}$	0.0
$\frac{e^2Q^2}{96}(M_{1133})_{crit}$	-0.052
$\frac{e^2Q^2}{96}(M_{3333})_{crit}$	0.346
$\frac{e^2Q^2}{96}(M_{2323})_{crit}$	0.059
$\frac{e^2Q^2}{96}(M_{3131})_{crit}$	0.224
$\frac{e^2Q^2}{96}(M_{1212})_{crit}$	0.187

Table 19

The ratios of the M-tensor components associated with the critical contribution to the relaxation at 432 K.

Ratio	Experimental value at 432 K	Theoretical value (reversal of NO_2 groups)
$\frac{(M_{1111})_{crit}}{(M_{3333})_{crit}}$	0.0	0.092
$\frac{(M_{1133})_{crit}}{(M_{3333})_{crit}}$	-0.150	-0.302
$\frac{(M_{2323})_{crit}}{(M_{3333})_{crit}}$	0.171	0.428
$\frac{(M_{3131})_{crit}}{(M_{3333})_{crit}}$	0.647	0.366
$\frac{(M_{1212})_{crit}}{(M_{3333})_{crit}}$	0.540	0.016

extrapolation of the experimental data from 298 K to 432 K is somewhat uncertain, the large discrepancy between the experimental and theoretical values of $(M_{1212})_{crit}/(M_{3333})_{crit}$ in Table 19 is somewhat surprising. It may mean that the NO_2 groups do not all lie on the $\underset{\sim\sim}{bc}$ plane when they reverse their orientation near the critical point.

6.5 Temperature dependence of the M-tensor components

We wish to show more clearly how the various M-tensor components vary with temperature. Even though we only determined the M-tensor components at four temperatures, we show them graphically as a function of temperature in Fig. 6.5. The data shown in Figs. 5.1, 5.2 and 5.6 have been used as a guide in interpolating between the four temperatures and in drawing smooth curves through the points in Fig. 6.5. The variation of M_{2323} and M_{3131} with temperature is more accurately known than that of the other components, since the ratio M_{3131}/M_{2323} is approximately the same (≈3) at all four temperatures, and since W_1 at $\theta=0°$ is equal to $(e^2Q^2/96)(8M_{2323}+ 8M_{3131})$ (see Eq.(3.4)). The dependence of M_{2323} and M_{3131} should therefore be very similar to the temperature dependence of W_1 shown in Figs. 5.1, 5.2 and 5.6. Fig. 6.5 indicates that all six M-tensor components have roughly the same anomalous temperature dependence below about 340 K. Above that temperature, five of the six components show critical behaviour whereas the sixth, M_{1111}, does not.

Figure 6.5

Values of the M-tensor components plotted as a function of temperature. The error bars are too small to be shown at 298 K and below. Figs. 5.1, 5.2 and 5.6 have been used as a guide in drawing smooth curves through the points. The data points and curves corresponding to the various M-tensor components can be identified from the key at the top of the graph. For convenience, M_{1133} is shown as being positive instead of negative. The values of M-tensor components at 170 K, shown in the box at the bottom left corner, have been multiplied by 10 in order to distinguish between them. The broken line parallel to the ordinate axis indicates the critical temperature (438 K).

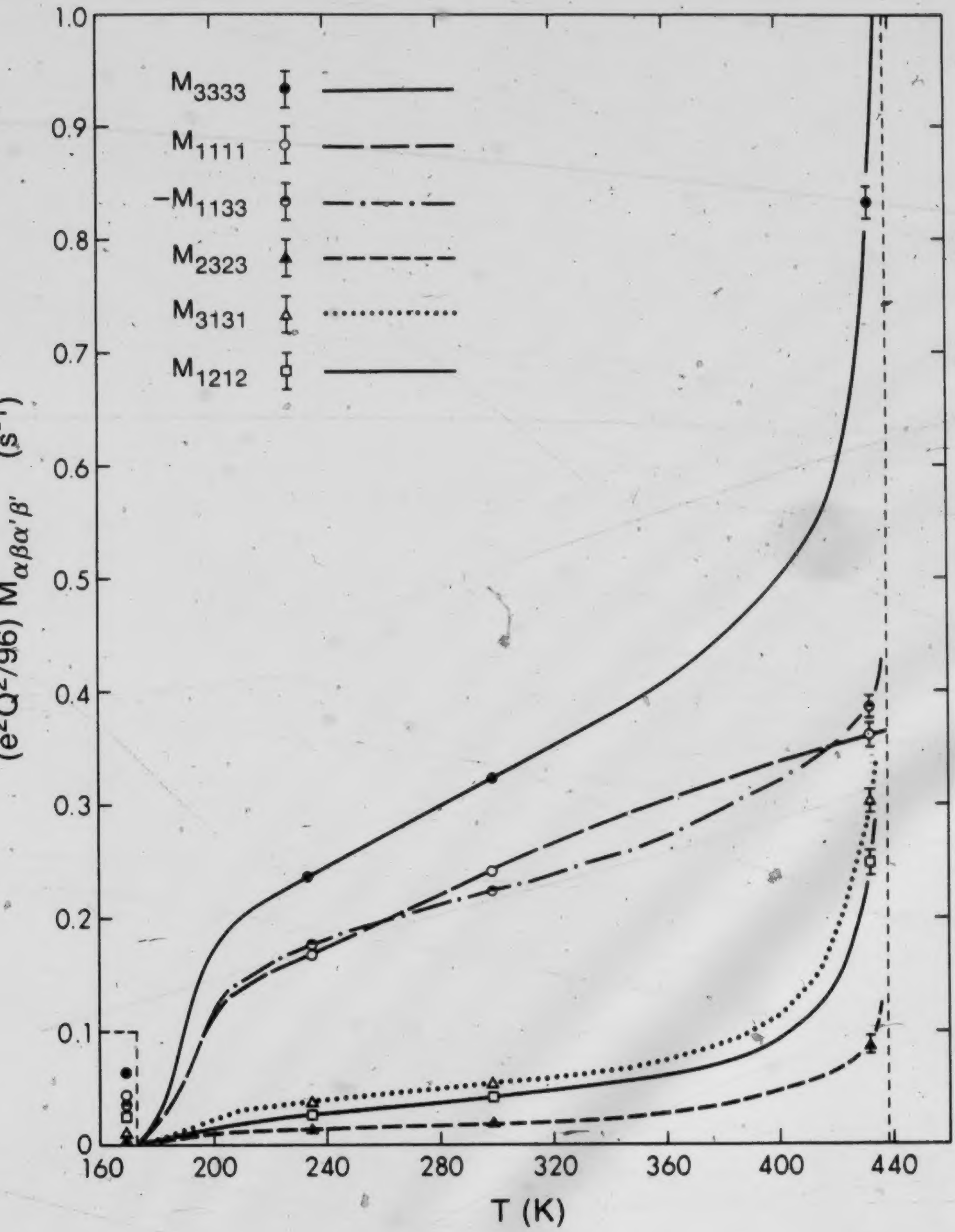
M_{3333}
M_{1111}
$-M_{1133}$
M_{2323}
M_{3131}
M_{1212}
$(e^2Q^2/96)\ M_{\alpha\beta\alpha'\beta'}$ (s^{-1})
0
0.1
0.2
0.3
0.4
0.5
0.6
0.7
0.8
0.9
1.0
160
200
240
280
320
360
400
440
T (K)

BIBLIOGRAPHY

Abe, Y., Ohneda, Y., Abe, S. and Kojima, S., 1972, J. Phys. Soc. Japan, 33, 864.

Abragam, A., 1961, The Principles of Nuclear Magnetism (Oxford: Clarendon Press).

Allen, J.E. and Segre, S.E., 1961, Nuovo Cimento, 21, 980.

Andrew, E.R. and Tunstall, D.P., 1961, Proc. Phys. Soc., 78, 1.

Avogadro, A., Cavelius, E., Muller, D. and Petersson, J., 1971, Phys. Status Solidi B, 44, 639.

Avogadro, A., Bonera, G. and Rigamonti, A., 1975, J. Magn. Reson., 20, 399.

Bayer, H., 1951, Z. Phys., 130, 227.

Becker, K.D., 1978, Phys. Stat. Sol. (b). 87, 589.

Bersohn, R., 1952, J. Chem. Phys., 20, 1505.

Bevington, P.R., 1969, Data Reduction and Error Analysis for the Physical Sciences (New York: McGraw-Hill) p. 313.

Betsuyaku, H., 1969, J. Phys. Soc. Japan, 27, 1485.

Bloembergen, N., 1949, Physica, 15, 386.

Bloembergen, N., Purcell, E.M. and Pound, R.V., 1948, Phys. Rev., 73, 679.

Bonera, G., Borsa, F. and Rigamonti, A., 1970, Phys. Rev. B, 2, 2784.

Buess, M.L. and Petersen, G.L., 1978, Rev. Sci. Instrum., 49, 1151.

Carlson, A.B., 1968, Communication Systems: An Introduction to Signals and Noise in Electrical Communication (New York: McGraw-Hill).

Cohen, M.H. and Reif, F., 1957, Solid State Physics, vol. 5, Eds. F. Seitz and D. Turnbull (New York: Academic Press) p. 321.

Contaxes, N. and Hatch, A.J., 1969, J. Appl. Phys., 40, 3548.

Das, T.P. and Hahn, E.L., 1958, Solid State Physics, Suppl.1, Eds. F. Seitz and D. Turnbull (New York: Academic Press) p. 40.

Ema, K., Hamano, K. and Hatta, I., 1975, J. Phys. Soc. Japan, 39, 726.

Ehrhardt, K.D. and Michel, K.H., 1981, Phys. Rev. Lett., 46, 291.

Freeman, R., Kempsell, S.P. and Levitt, M.H., 1980, J. Magn. Reson., 38, 453.

Fukushima, E. and Roeder, S.B.W., 1981, Experimental Pulse NMR (London: Addison-Wesley).

Gesi, K., 1969, J. Phys. Soc. Japan, 26, 953.

Hatta, I. and Ikushima, A., 1973, J. Phys. Chem. Solids, 43, 57.

Hoult, D.I., 1978, Prog. in NMR Spectroscopy, 12, 41.

Hughes, D.G., 1973, J. Phys. C, 6, 3797.

Hughes, D.G., 1986, Private communication.

Hughes, D.G., Reed, K. and Snyder, R.E., 1970, Can. J. Phys., 48, 2212.

Hughes, D.G. and Reed, K., 1971, J. Phys. C, 4, 2945.

Hughes, D.G. and Spencer, P.A., 1982, J. Phys.C, 15, 7417.

Hughes, D.G. and Pandey, L., 1984, J. Magn. Reson., 56, 428.

International Telephone and Telegraph Corporation, 1977, Reference Data for Radio Engineers (New York: Howard W. Sams & Co., Inc.).

Kasahara, M., Hikita, T., Tatsuzaki, I. and Sasakawa, K., 1977, J. Phys. Soc. Japan, 42, 1239.

Kay, M.I. and Frazer, B.C., 1961, Acta Crystallogr., 14, 56.

Kinase, W. Makino, W. and Takahashi, K., 1985, Ferroelectrics, 64, 173.

Landau, L.D. and Lifshitz, E.M., 1958, Statistical Physics (London: Pergamon Press) p. 337.

Levitt, M.H. and Freeman, R., 1979, J. Magn. Reson., 33, 473.

Magid, L.M., 1972, Electromagnetic Fields, Energy and Waves (New York: Wiley) p. 519.

Marino, R.A. and Bray, R., 1968, J. Magn. Reson.,48, 4833.

Markham, J.J., 1966, Solid State Physics, Suppl. 8, Eds. F. Seitz and D. Turnbull (New York: Academic Press).

McLachlan, L.A., 1977, J. Magn. Reson., 26, 223.

McLachlan, L.A., 1980, J. Magn. Reson., 39, 11.

Niemelä, L., 1967, Ann. Acad. Sci. Fenn. (Finland), A 6, No. 236.

Nye, J., 1957, Physical Properties of Crystals (Oxford: University Press).

Pandey, L. and Hughes, D.G., 1984, J. Magn. Reson., 56, 443.

Petersen, G. and Bray, P.J., 1976, J. Chem. Phys., 64, 522.

Pietilä, A., 1968, Ann. Acad. Sci. Fenn. (Finland), A 6, No. 271.

Poole, C.P., 1967(a), Electron Spin Resonance (New York: Wiley) p. 341.

Poole, C.P., 1970(b), ibid. p. 403.

Pound, R.V., 1950, Phys. Rev., 79, 685.

Powell, R.L., Hall, W.J., Hyink, C.H., Sparks, L.L., Burns, G.W., Scroger, M.G. and Plumb, H.H., 1974, Thermocouple Reference Tables Based on the IPTS-68 (Washington: National Bureau of Standards).

Ramsey, N.F., 1953, Nuclear Moments (New York: Wiley).

Redfield, A.G., 1956, Phys. Rev., 67, 10.

Sakiyama, M., Kimoto, A. and Seki, S., 1965, J. Phys. Soc. Japan, 20, 2180.

Sawada, S., Nomura, S., Fujit, S. and Yosida, I., 1958, Phys. Rev. Lett., 1, 320.

Schmidt, V.H., 1972, Pulsed Magnetic and Optical Resonance, Proceedings of the Ampere International Summer School II, Basko polje, 1971, Ed. R. Blinc (University of Ljubljana, Ljubljana, Yugoslavia) p. 75.

Slichter, C.P., 1980, Principles of Magnetic Resonance (New York: Springer).

Snyder, R.E. and Hughes, D.G., 1971, J. Phys. C, 4, 227.

Spencer, P.A. and Hughes, D.G., 1978, J. Phys. C, 11, 183.

Suzuki, S. and Takagi, M., 1971, J. Phys. Soc. Japan, 30, 188.

Townsend, J.S. and Donaldson, R.H., 1928, Philos. Mag. J. Sci., 5, 178.

Towta, S. and Hughes, D.G., 1986, Z. Naturf., 41a, 370.

Van Kranendonk, J., 1954, Physica, 20, 781.

Van Kranendonk, J. and Walker, M., 1967, Phys. Rev. Lett., 18, 701.

Van Kranendonk, J. and Walker, M., 1968, Can. J. Phys., 46, 2241.

Weber, M.J., 1963, Phys. Rev., 130, 1.

Weiss, A., 1960, Z. Naturf., 15a, 536.

Weiss, A. and Biedenkapp, D., 1962, Z. Naturf., 17b, 794.

Wikner, E.G., Blumberg, W.E. and Hahn, E.L., 1960, Phys. Rev. 118, 631.

Yamada, Y. Shibuya, I. and Hoshino, S., 1963, J. Phys. Soc. Japan, 18, 1594.

Yamada, Y. and Yamada,T., 1966, J. Phys. Soc. Japan, 21, 2167.

Yosida, K. and Moriya, T., 1956, J. Phys. Soc. Japan, 11, 33.

Ziegler, G.E., 1931, Phys. Rev., 38, 1040.